UNIVERSITY OF CALIFORNIA, SAN DIEGO

An Analysis of Astrophysics and Fundamental Physics from the Lyman-alpha Forest

A dissertation submitted in partial satisfaction of the
requirements for the degree
Doctor of Philosophy

in

Physics

by

Aaron Day

Committee in charge:

Professor David Tytler, Chair
Professor George Fuller
Professor Michael Norman
Professor Justin Roberts
Professor George Tynan

2013

The dissertation of Aaron Day is approved, and it is acceptable in quality and form for publication on microfilm and electronically:

_____

_____

_____

_____

_____

Chair

University of California, San Diego

2013

DEDICATION

To my Dad, Steven Raymond Day

Our countless discussions about science, engineering, and life have deeply contributed to the formation of this dissertation.

EPIGRAPH

The whole history of physics
proves that a new discovery is quite likely
lurking at the next decimal place.
—F.K. Richtmeyer

TABLE OF CONTENTS

LIST OF FIGURES

LIST OF TABLES

ACKNOWLEDGEMENTS

Chapter 2, in full, is currently being prepared for submission for publication of the material. Day, Aaron; Tytler, David; Kirkman, David; Norman, Michael. The dissertation author was the primary investigator and author of this material.

Chapter 3, in full, is currently being prepared for submission for publication of the material. Day, Aaron; Tytler, David; Kirkman, David; Lopez, Liliana; Liang, Jia. The dissertation author was the primary investigator and author of this material.

Chapter 4, in full, is currently being prepared for submission for publication of the material. Day, Aaron; Tytler, David; Kirkman, David. The dissertation author was the primary investigator and author of this material.

VITA

2013	Ph. D. in Physics, University of California, San Diego
2009	M.S. in Physics, University of California, San Diego
2003	B. S. in Physics; Computer Science; and Applied Computational and Mathematical Science, University of Washington

ABSTRACT OF THE DISSERTATION

An Analysis of Astrophysics and Fundamental Physics from the Lyman-alpha Forest

by

Aaron Day

Doctor of Philosophy in Physics

University of California, San Diego, 2013

Professor David Tytler, Chair

The Lyα forest, made up of the cosmologically redshifted hydrogen Lyα absorption lines in the spectra of distant quasars, is a sensitive probe of cosmology and astrophysics. The shape and distribution of the Lyα absorption lines is determined by the column densities, peculiar velocities, redshifts, turbulent velocities, temperatures, and the distribution of systems of neutral hydrogen in the space between galaxies known as the intergalactic medium. The Lyα forest is sensitive to the total cosmological matter power spectrum at the smallest available scales. It provides a long lever arm for constraints on the shape of the matter power spec-

trum when used in conjunction with measurements at large scales, such as the cosmic microwave background. It also has the potential to be used to detect the small scale matter power suppression caused by the free streaming of fundamental particles including known active light neutrinos or potential warm dark matter candidates.

Focusing on the line widths, optical depth, and the power spectrum of the flux of the Lyα forest, we find that previously published observations do not match the outputs of fully hydrodynamic cosmological computer simulations. We present a new measurement of the power spectrum of the flux of the Lyα forest, using 91 quasar spectra taken with the Keck HIRES spectrograph. This is the largest high resolution data set to date by a factor of about 3. The high resolution of our data sample gives fully resolved absorption lines. Compared to the low resolution data set from SDSS, the HIRES data allows for more accurate subtraction of metal line contamination, as well as a measurement of the flux power at the smallest scales. Finally, we run a suite of 44 new computer simulations, varying cosmological and astrophysical parameters in an attempt to find a model that matches our observational data. We find that no standard cosmological or astrophysical parameters provide an acceptable match. This calls into question previous constraints on cosmological parameters made from Lyα forest data sets.

Chapter 1

Introduction

1.1 The Lyα forest

At the center of many galaxies lie super-massive black holes, which through their accretion of matter shine as the brightest stable sources of electromagnetic radiation in the universe. These objects are known as quasars. Quasars emit electromagnetic radiation at a nearly uniform intensity over a wide wavelength range. The brightness and uniformity of their spectra makes them useful for the measurement of absorption lines caused by matter along the line of sight. The most abundant element in the universe is hydrogen, and the relatively strong Lyα transition makes Lyα absorption lines ideal for measuring properties of the intergalactic medium (IGM).

While the central wavelength of a Lyα line in the rest frame of the absorbing hydrogen is always 1215.668 Å, the cosmological expansion of space increases the wavelength measured by an observer on Earth. For redshifts greater than about 1.6, the line is shifted into the visible spectrum, and can be observed through Earth's atmosphere. Since the amount of redshifting is a function of the distance

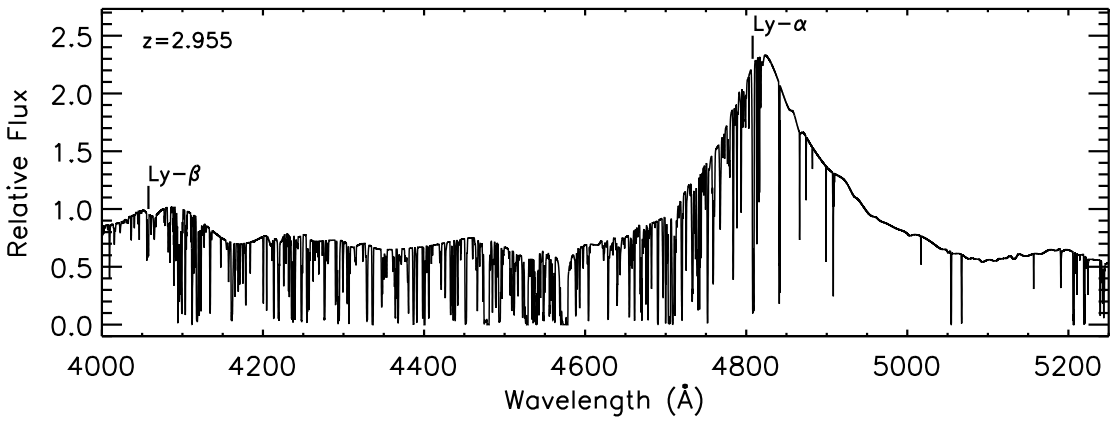

Figure 1.1: Lyα forest spectrum. All absorption lines to the right of the Lyα line are from elements other than hydrogen. All hydrogen absorption lines between the quasar's Lyα emission line and the Lyβ emission line are due to Lyα absorption by intergalactic hydrogen.

to the object being observed, each Lyα absorption line in a quasar spectrum is shifted to a wavelength corresponding to its position in space.

If the initial wavelength of a photon emitted in the rest frame of the quasar is less than the Lyα wavelength, then at some point as the light travels to Earth, its wavelength will increase until it becomes equal to Lyα, and it can be absorbed by neutral hydrogen (HI) at the right position in space. Since the Lyα transition is the shortest wavelength transition for hydrogen and Lyβ is the second shortest, no other hydrogen transitions could lead to an absorption line in the quasar rest wavelength range between Lyα and Lyβ, no matter the redshift. This dissertation is focused on properties of the spectrum between these two lines, known as the Lyα forest. There is a small contribution from absorption lines from elements other than hydrogen which contaminate the Lyα forest spectrum and must be removed.

The Lyα forest probes the distribution and evolution of neutral hydrogen for redshifts between about 1.6 and 4.2, or from about 1.5 billion years after the big bang up until around 4.1 billion years, with the current age of the universe being

around 14 billion years. Each quasar spectrum provides data on scales ranging from 1 to 40 comoving Mpc, where 1 Mpc $= 3.26 \times 10^6$ light years. It contains information about cosmological parameters, including the matter power spectrum, as well as astrophysical parameters, such as the ionization and thermal state of the cosmological hydrogen distribution.

The Lyα forest is a measure of column densities, peculiar velocities, redshifts, turbulent velocities, temperatures, and the distribution of matter in the universe and how these evolve with time. This introduction chapter describes how each of these parameters specifies the Lyα forest. In §1.2, we give a description of how the shape of a single absorption line is determined by the column density, temperature, and turbulent velocities of the HI absorbers. In §1.3, we describe the primordial distribution of matter, along with the physics of the cosmological expansion history that gives rise to the redshifts that shift the wavelengths of the absorption lines by a factor depending on the distance to the HI absorber. In §1.4, we describe a method of determining the mass of light active neutrinos or warm dark matter based on the suppression of gravitational collapse on small distance scales. Then in §1.5, we discuss the thermal and ionization history of the intergalactic medium and how these influence the Lyα forest. Finally, in §1.6 we give a description of the simulations that enable us to extract information about the various parameters that give rise to the Lyα forest.

1.2 Absorption lines

The Lyα forest is made up of the superposition of many HI absorption lines. Each absorption line in the Lyα forest can be represented by a Voigt profile, the convolution of a Lorentz profile for the natural line width with a Maxwellian

velocity distribution. The Lorentz profile is the quantum mechanical description of the probability of a single hydrogen atom absorbing a photon of a given frequency, and moving to a higher energy level. The Lorentz profile is given by:

$$\phi_\nu = \frac{4\gamma_{ul}}{16\pi^2(\nu - \nu_{ul})^2 + \gamma_{ul}^2}, \tag{1.1}$$

where γ_{ul} is the damping width of the upper level, ν is the photon frequency, and ν_{ul} is the resonance line frequency. The Maxwellian velocity distribution is present because the absorption is caused by an ensemble of hydrogen atoms with a velocity distribution set by a combination of the thermal and kinematic velocity of a cloud of hydrogen gas. The Maxwellian velocity profile is given by:

$$p_v = \frac{1}{\sqrt{\pi}b} e^{-(v-v_0)^2/b^2}. \tag{1.2}$$

The velocity of each individual hydrogen atom can be thought of as leading to a doppler shift in the frequency at which the hydrogen atom will absorb. Bulk movement of the gas will shift the entire absorption line frequency through the $(v - v_0)$ term in the exponential. The shape of the Maxwellian distribution is solely determined by the b-value, which consists of both thermal and turbulent kinematic components added in quadrature:

$$b = \sqrt{b_{th}^2 + b_{kin}^2} \tag{1.3}$$

$$b_{kin} = \sqrt{2kT/m_H} \tag{1.4}$$

The total absorption profile is given by the convolution of the two proba-

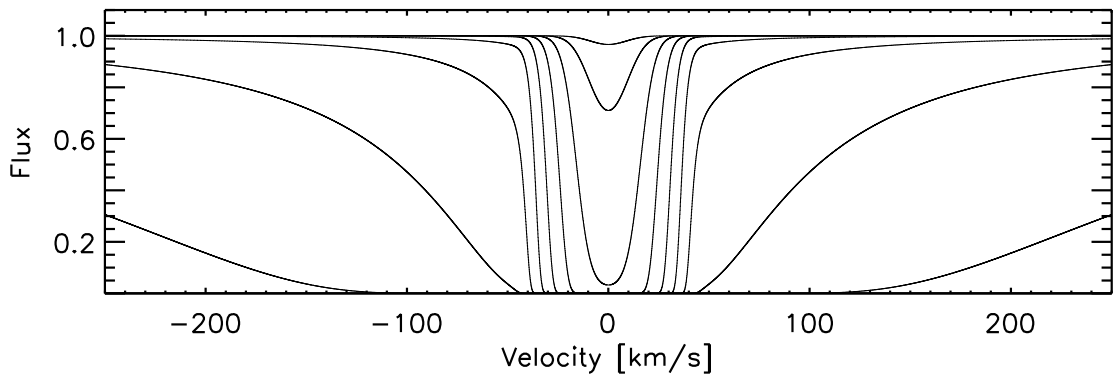

Figure 1.2: Lyα absorption lines. The narrowest absorption line has $N(HI) = 10^{12} cm^{-2}$, and the widest line has $N(HI) = 10^{20} cm^{-2}$, with each subsequent line representing a factor of 10 increase in column density. All absorption lines have $b = 25 km/s$.

bility distributions:

$$\phi_\nu^{Voigt} \equiv \int d\nu' p_v(v - v')\phi_\nu = \frac{1}{\sqrt{\pi}} \int \frac{d\nu}{b} e^{-v^2/b^2} \frac{4\gamma_{ul}}{16\pi^2(\nu - \nu_{ul})^2 + \gamma_{ul}^2}. \tag{1.5}$$

The optical depth at a given frequency ν is then given by:

$$\tau_\nu \propto N_{HI} \phi_\nu^{Voigt}, \tag{1.6}$$

where N_{HI} is density of HI integrated along the line of sight, known as the column density. The observable is the normalized flux level of the quasar spectrum, which is:

$$F = e^{-\tau_\nu}. \tag{1.7}$$

The shape of an absorption line is thus specified by a combination of the b-value and N_{HI}.

Figure 1.2 demonstrates the dependence of absorption line shape on column density. For unsaturated lines, the equivalent width (integral of the absorption line profile) increases linearly with $N(HI)$. For saturated lines, the equivalent

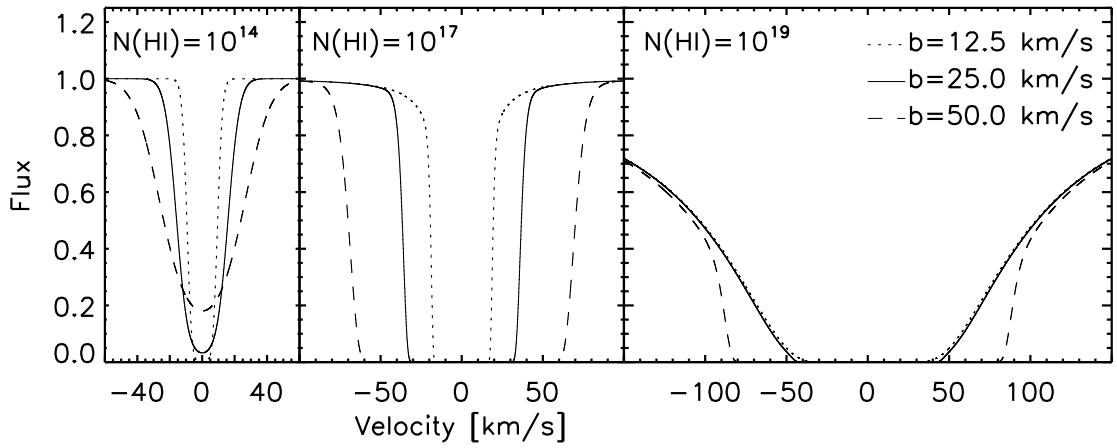

Figure 1.3: Lyα absorption lines. Increasing the b-value widens the absorption line profile. Absorption lines with $N(HI) \gtrsim 10^{20} cm^{-2}$ are completely specified by their column density, and have no measurable dependence on the b-value.

width increases with $log(N(HI))$ until $N(HI) \gtrsim 10^{18} cm^{-2}$, at which point the damping wings from the Lorentz profile become pronounced, and the equivalent width increases with the square root of $N(HI)$.

Figure 1.3 demonstrates the dependence of absorption line shape on b-value. At low column densities, the line width is dominated by the Maxwellian distribution, with larger temperatures leading to wider lines. Since the Lorentz profile drops off slower than the Maxwellian profile, high column density lines with $N(HI) \gtrsim 10^{20} cm^{-2}$ are dominated by the Lorentz profile, with the b-value having little effect on the line shape.

1.3 Cosmology

1.3.1 The primordial power spectrum

The initial conditions for the cosmological distribution of hydrogen are set by the physics of the Big Bang. The standard theory is that sometime around

10^{-36} seconds after the big bang, a brief period of inflation lasting only around 10^{-32} seconds expanded tiny quantum mechanical fluctuations to cosmological distance scales, providing the small density inhomogeneities necessary for structure formation. In inflationary theories, the perturbations are a nearly scale invariant Gaussian random field, which is completely specified by its power spectrum. This primordial power spectrum is given by:

$$P(k) = A_s(\frac{k}{k_0})^{n_s-1+\alpha_s lnk}. \tag{1.8}$$

The running of the spectral index, α_s is predicted to be 0. Thus the initial statistical distribution of matter is fully specified by just two free parameters, the amplitude of the power spectrum A_s, and the spectral index n_s. The spectral index is a measure of the small deviation from scale invariance predicted by inflation, with a value predicted to be close to 1.

The matter power spectrum has been measured using the cosmic microwave background radiation [21], galaxy clustering [30], gravitational lensing [14, 3], and the Lyα forest [27, 12]. The Lyα forest probes the smallest scales, and so offers strong constraints on the shape of the power spectrum when combined with other measurement sources at larger scales.

1.3.2 The expansion of the universe

The expansion of the universe is determined by Einstein's general theory of relativity, the fundamental theory of gravity. At large enough scales, the universe is observed to be homogeneous and isotropic. This fact combined with Einstein's field equations, which comprise Einstein's general theory of relativity, directly lead

to Friedmann's equation:

$$H \equiv \frac{\dot{a}}{a} = \sqrt{\frac{8\pi G}{3}\rho - \frac{kc^2}{a^2}} \tag{1.9}$$

where ρ is the energy density of the universe, a is the scale factor, G is the gravitational constant, c is the speed of light, and k is the spatial curvature, with a value of +1, 0, or -1. The second term is so far immeasurably small (possibly equal to 0), and so the expansion rate is determined by the energy density. The scale factor is the distance scale of the universe. If the scale factor doubles, the distance between particles in space doubles.

To illuminate the various contributions to the energy density, Friedmann's equation can be restated as:

$$H = H_0\sqrt{\Omega_R a^{-4} + \Omega_M a^{-3} + \Omega_k a^{-2} + \Omega_\Lambda}, \tag{1.10}$$

where H_0 is the Hubble constant, Ω_R is the radiation density, Ω_M is the matter density, Ω_k is the spatial curvature density, and Ω_Λ is the cosmological constant, and all these parameters are at their present day values, at $a = 1$. The only variable with time dependence in this equation is a, and so it is straight forward to integrate to obtain the scale factor at any point in time. For a Lyα absorption line, the observed wavelength will be shifted due to this expansion by:

$$\lambda = (1 + z)\lambda_0, \tag{1.11}$$

where $z \equiv \frac{a_0}{a} - 1$ is the redshift, and λ_0 is the rest wavelength.

With time, higher density regions undergo gravitational collapse, while the bulk of the volume of the universe expands. Initially, the growth of structure is

linear, with Fourier modes evolving independently. As time goes on, dense regions gravitationally attract more mass, and become denser, leading to nonlinear growth. In the nonlinear regime, N-body Newtonian gravitational physics must be applied to obtain an accurate description of the matter distribution. The Lyα forest probes distance scales that are only mildly nonlinear at the measured epoch. The positions and clustering of the absorption lines is determined by the expansion of space and the matter power spectrum. The shape of the absorption lines is influenced by the growth of structure through the column density of the absorbers.

1.4 Neutrino and/or warm dark matter mass

One exciting use of the Lyα forest is as a probe of the mass of light fundamental particles, including neutrinos and warm dark matter. Neutrino oscillation experiments have found that the sum of the masses of the 3 light active neutrinos is greater than 0.05 eV. The current upper bound from terrestrial experiments is $\Sigma m_\nu \leq 6.6eV$, from tritium beta decay experiments [6, 25, 31, 22, 32]. The future KATRIN tritium beta decay experiment is expected to have the ability to measure a neutrino mass as low as 0.6eV. This leaves a large range of possible masses that not only has not been tested in terrestrial experiments, but may not be measurable by these experiments for the foreseeable future. Cosmological measurements offer the ability to measure the neutrino masses at whatever value they might have.

Neutrinos or warm dark matter particles both suppress gravitational collapse on small scales due to their free-streaming out of potential wells. These particles essentially only interact gravitationally due to their weak scattering cross sections. Therefore, they keep their initial velocity distribution, which becomes redshifted with the expansion of space. In the case of active neutrinos and in some

warm dark matter particle models, the initial velocity distribution is theorized to be a thermal distribution that was once in equilibrium with baryonic matter shortly after the Big Bang. The velocity dispersion sets the free-streaming scale, below which matter cannot collapse. The free-streaming wavenumber is defined as:

$$k_{FS} \equiv \sqrt{4\pi G\rho}\frac{a}{\langle v\rangle} \tag{1.12}$$

where ρ is the average density of the universe, G is the gravitational constant, a is the scale factor, and $\langle v\rangle$ is the velocity dispersion of the active neutrinos or warm dark matter [7]. This equation is analogous to the Jean's scale, utilized in astrophysical processes to describe the gravitational collapse of a cloud which is supported by a velocity dispersion. At scales below k_{FS}, gravitational collapse is inhibited. The signature of the free streaming scale is a suppression of the matter power spectrum below a specific wave number compared to a fiducial model. Using Eqn. 1.9, Eqn. 1.12 can be written as:

$$k_{FS} = \sqrt{\frac{3}{2}}\frac{aH}{\langle v\rangle} \tag{1.13}$$

with the velocity dispersion given by:

$$\langle v\rangle = \sqrt{\frac{3kT}{m}}. \tag{1.14}$$

A particle with a smaller mass has a larger free streaming scale due to its greater velocity dispersion. Thus if we can measure k_{FS}, we can determine the neutrino mass, given the well established theory of the temperature of cosmic neutrinos.

1.5 Astrophysics

1.5.1 Ionization Fraction of Hydrogen

Given that the Lyα forest is created by neutral hydrogen, in order to obtain any cosmological information, it is critical to obtain an accurate model of the ionization fraction of hydrogen throughout the IGM. The ionization state and temperature also affect structure formation, and so it is important to use a model that follows the evolution with time. Although the universe began in a hot, ionized state, this did not last long, as adiabatic cooling caused by the expansion of space reduced the temperature to the point where protons and electrons could combine into neutral hydrogen. Before recombination, photons were coupled to the plasma through Thompson scattering. After hydrogen became neutral, the photons no longer interacted with it, and traveled freely, redshifting with the expansion of space to become what we detect today as the cosmic microwave background radiation (CMB). Through measurements of the current temperature of the CMB, it has been determined that recombination occurred at a redshift of 1100, when the universe was approximately 380,000 years old.

The Lyα forest cannot be seen until bright sources of light form, against which neutral hydrogen can absorb. Even then, at any point in the expansion history of the universe, there is enough hydrogen to completely absorb all photons at the Lyα wavelength. It is not until enough sources of ionizing radiation form that the hydrogen obtains a high enough ionization fraction that it becomes transparent enough that absorption features can be detected and used as a probe of its distribution in space. The detection of Thompson scattering of CMB photons off of free electrons available due to the presence of ionized hydrogen indicates that the ionization of hydrogen in the IGM began around a redshift of 11 [23]. The presence

of a complete Gunn-Peterson absorption trough in quasars with HI absorption at $z \sim 6$ and the rapid transition to partial transmission of Lyα photons at a slightly lower redshift indicates that ionization of HI was nearly complete by $z \sim 6$ [4]. At the redshifts at which the Lyα forest is commonly studied ($2.0 \leq z \leq 4.0$), the neutral fraction of both hydrogen and helium is less than $\sim 10^{-3}$ in the bulk of the IGM, and the mean free path of ionizing photons is greater than 50 Mpc [18]. Sources of ionizing radiation, including galaxies and quasars, are separated by much smaller distances, and so the ionizing radiation field for HI and HeI is approximately uniform [17, 26]. Over time, photoionization equilibrium is established, in which photoionizations are balanced by recombinations, and photoheating is balanced by adiabatic cooling. This process will erase any initial inhomogeneity of the ionization and thermal state, and the temperature will asymptotically approach a form given by the uniform ultraviolet background (UVB) [19, 20].

1.5.2 Temperature

The temperature of the IGM is important for several reasons: it contributes to the line widths as described in §1.2, it controls the pressure which sets the size and density of absorbing regions, and it sets the recombination rate of hydrogen. In the most widely used models of the IGM, the main heating source is photoionizations. When a photon ionizes an atom, any additional energy above that required for the ionization goes into heating the gas. By the redshifts of the Lyα forest, HI and HeI ionizations are due to a uniform ionizing background, but the higher ionization potential of HeII causes it not to be ionized until $z \sim 3$. The photoionization of HeII during the time that the Lyα forest is absorbed causes significant heating, which may be non-uniform due to radiative transfer physics of the HeII [28, 5, 15, 16].

There is also the potential for other sources of heating, including decaying dark matter, annihilating dark matter, and blazars [9, 10, 8]. Each of these possible sources have a different density dependence, and thus would leave their own characteristic mark on the Lyα forest. Most temperature models of the IGM used to extract cosmological data from the Lyα forest use a uniform ionizing background or an imposed temperature density relationship. A wider range of possible thermal history scenarios should be tested to ensure the correct model is chosen allowing accurate cosmological parameters to be determined.

1.6 Simulations

The standard means of interpreting Lyα forest data sets is through the use of large hydrodynamic computer simulations. In this dissertation, we use the publicly available ENZO code. These simulations follow both cold dark matter and baryonic gas (H, H+, He, He+, He++, and e-).

The dark matter is implemented as a set of particles, each with a position and velocity. The dark matter particle trajectories are calculated by solving Poisson's equation including the gravitational potential of both the dark matter and the baryonic matter.

The baryonic matter is implemented as a fluid on a Cartesian grid with periodic boundary conditions. Each cell includes the velocity, temperature, density of each species, internal gas energy, and total energy. In addition to the gravitational forces, the baryonic matter experiences hydrodynamic forces, which are calculated using the piecewise parabolic method of [11]. Cooling and heating of the baryonic gas includes both collisional and radiative processes for each of the 6 species [29, 1, 2]. Ionization and photo-heating rates are dependent on the ionizing

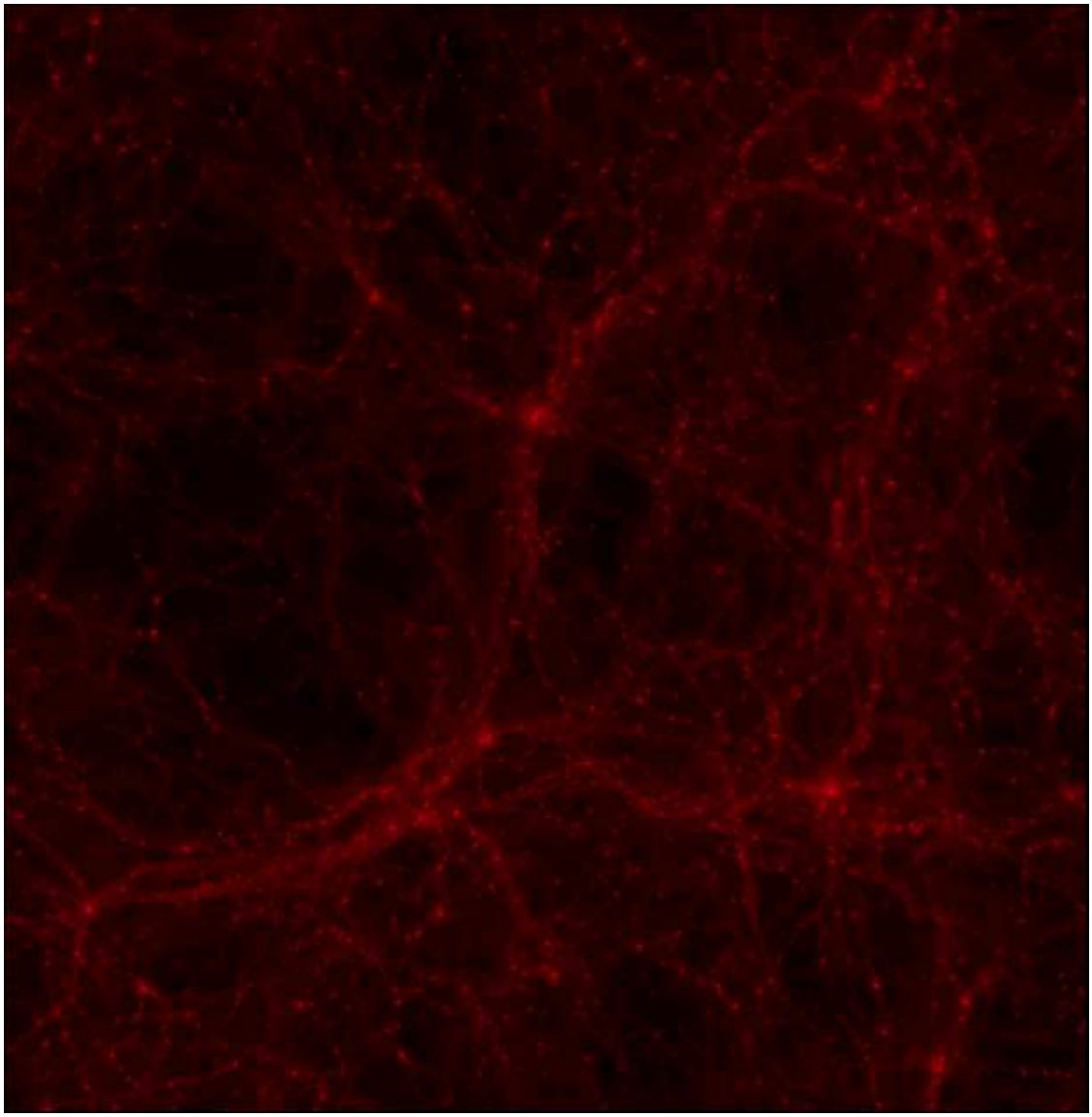

Figure 1.4: A slice of a cosmological simumlation run with ENZO. The brightness of the image scales with the log of the dark matter density. The length of a side is 19.2 Mpc comoving.

background radiation, as described in §1.5.

Initial conditions for the dark matter positions and velocities and the baryonic matter densities and velocities are specified by an initial power spectrum. The density fluctuations in k-space are calculated on a uniform Cartesian grid, and the Fourier Transform is taken to obtain the physical density fluctuations. We ran most of our simulations with initial conditions generated with the algorithm developed by [13]. We also ran a few simulations with massive light neutrinos using initial conditions generated by CAMB [24].

We generate Lyα forest spectra along lines of sight through the simulation cube. For each line of sight, we choose a random starting location and a random direction. We then integrate Eqn. 1.5 and calculate the flux from Eqn. 1.7, using the simulated HI density, temperature, and velocity fields.

1.7 Summary

The Lyα forest contains information about fundamental physics, including the primordial matter power spectrum and the masses of fundamental particles. It also encodes astrophysics, including the temperature and ionization state of hydrogen and helium in the IGM. In the work that this dissertation comprises, we provide the most precise measurements of the small scale flux power spectrum of the Lyα forest to date. We also provide data from computer simulations and compare the results to the observational data set. We show that the current standard model of the IGM is insufficient to explain the measured properties of the Lyα forest. Further research will need to be conducted to find a model that accurately explains the features found in observational data. The precision of the observational data set we provide has the potential to contain information

regarding fundamental physics that is waiting to be exploited by new, more realistic computer simulations.

Bibliography

[1] T. Abel, P. Anninos, Y. Zhang, and M. L. Norman. Modeling primordial gas in numerical cosmology. *New Astronomy*, 2:181, Aug. 1997.

[2] P. Anninos, Y. Zhang, T. Abel, and M. L. Norman. Cosmological hydrodynamics with multi-species chemistry and nonequilibrium ionization and cooling. *New Astronomy*, 2:209–224, 1997.

[3] D. J. Bacon, A. R. Refregier, and R. S. Ellis. Detection of weak gravitational lensing by large-scale structure. *MNRAS*, 318:625–640, Oct. 2000.

[4] R. H. Becker, X. Fan, R. L. White, M. A. Strauss, V. K. Narayanan, R. H. Lupton, J. E. Gunn, J. Annis, N. A. Bahcall, J. Brinkmann, A. J. Connolly, I. Csabai, P. C. Czarapata, M. Doi, T. M. Heckman, G. S. Hennessy, Ž. Ivezić, G. R. Knapp, D. Q. Lamb, T. A. McKay, J. A. Munn, T. Nash, R. Nichol, J. R. Pier, G. T. Richards, D. P. Schneider, C. Stoughton, A. S. Szalay, A. R. Thakar, and D. G. York. Evidence for Reionization at z $\sim$ 6: Detection of a Gunn-Peterson Trough in a z=6.28 Quasar. *AJ*, 122:2850–2857, Dec. 2001.

[5] J. S. Bolton, S. P. Oh, and S. R. Furlanetto. Photoheating and the fate of hard photons during the reionization of HeII by quasars. *MNRAS*, 395:736–752, May 2009.

[6] J. Bonn, B. Bornschein, L. Bornschein, L. Fickinger, B. Flatt, O. Kazachenko, A. Kovalik, C. Kraus, E. Otten, J. Schall, H. Ulrich, and C. Weinheimer. The mainz neutrino mass experiment. *Nuclear Physics B - Proceedings Supplements*, 91(1-3):273 – 279, 2001.

[7] A. Boyarsky, J. Lesgourgues, O. Ruchayskiy, and M. Viel. Lyman-α constraints on warm and on warm-plus-cold dark matter models. *Journal of Cosmology and Astro-Particle Physics*, 5:12–+, May 2009.

[8] P. Chang, A. E. Broderick, and C. Pfrommer. The Cosmological Impact of Luminous TeV Blazars. II. Rewriting the Thermal History of the Intergalactic Medium. *ApJ*, 752:23, June 2012.

[9] X. Chen and M. Kamionkowski. Particle decays during the cosmic dark ages. *Phys. Rev. D*, 70(4):043502, Aug. 2004.

[10] M. Cirelli, F. Iocco, and P. Panci. Constraints on Dark Matter annihilations from reionization and heating of the intergalactic gas. *Journal of Cosmology and Astro-Particle Physics*, 10:9, Oct. 2009.

[11] P. Colella and P. R. Woodward. The Piecewise Parabolic Method (PPM) for Gas-Dynamical Simulations. *Journal of Computational Physics*, 54:174–201, Sept. 1984.

[12] R. A. C. Croft, D. H. Weinberg, M. Bolte, S. Burles, L. Hernquist, N. Katz, D. Kirkman, and D. Tytler. Toward a Precise Measurement of Matter Clustering: Lyα Forest Data at Redshifts 2-4. *ApJ*, 581:20, Dec. 2002.

[13] D. J. Eisenstein and W. Hu. Power Spectra for Cold Dark Matter and Its Variants. *ApJ*, 511:5–15, Jan. 1999.

[14] L. Fu, E. Semboloni, H. Hoekstra, M. Kilbinger, L. van Waerbeke, I. Tereno, Y. Mellier, C. Heymans, J. Coupon, K. Benabed, J. Benjamin, E. Bertin, O. Doré, M. J. Hudson, O. Ilbert, R. Maoli, C. Marmo, H. J. McCracken, and B. Ménard. Very weak lensing in the CFHTLS wide: cosmology from cosmic shear in the linear regime. *A&A*, 479:9–25, Feb. 2008.

[15] S. Furlanetto and S. P. Oh. Inhomogeneous Helium Reionization and the Equation of State of the Intergalactic Medium. *ArXiv e-prints*, 711, Nov. 2007.

[16] S. R. Furlanetto and S. P. Oh. The History and Morphology of Helium Reionization. *ApJ*, 681:1–17, July 2008.

[17] F. Haardt and P. Madau. Radiative Transfer in a Clumpy Universe. II. The Ultraviolet Extragalactic Background. *ApJ*, 461:20, Apr. 1996.

[18] F. Haardt and P. Madau. Radiative Transfer in a Clumpy Universe. IV. New Synthesis Models of the Cosmic UV/X-Ray Background. *ApJ*, 746:125, Feb. 2012.

[19] L. Hui and N. Y. Gnedin. Equation of state of the photoionized intergalactic medium. *MNRAS*, 292:27, Nov. 1997.

[20] L. Hui and Z. Haiman. The Thermal Memory of Reionization History. *ApJ*, 596:9–18, Oct. 2003.

[21] E. Komatsu, K. M. Smith, J. Dunkley, C. L. Bennett, B. Gold, G. Hinshaw, N. Jarosik, D. Larson, M. R. Nolta, L. Page, D. N. Spergel, M. Halpern, R. S. Hill, A. Kogut, M. Limon, S. S. Meyer, N. Odegard, G. S. Tucker, J. L. Weiland, E. Wollack, and E. L. Wright. Seven-year Wilkinson Microwave Anisotropy Probe (WMAP) Observations: Cosmological Interpretation. *ApJS*, 192:18, Feb. 2011.

[22] C. Kraus, B. Bornschein, L. Bornschein, J. Bonn, B. Flatt, A. Kovalik, B. Ostrick, E. W. Otten, J. P. Schall, T. Thummler, and C. Weinheimer. Final results from phase ii of the mainz neutrino mass search in tritium beta decay. *EUR.PHYS.J.C*, 40:447, 2005.

[23] D. Larson, J. Dunkley, G. Hinshaw, E. Komatsu, M. R. Nolta, C. L. Bennett, B. Gold, M. Halpern, R. S. Hill, N. Jarosik, A. Kogut, M. Limon, S. S. Meyer, N. Odegard, L. Page, K. M. Smith, D. N. Spergel, G. S. Tucker, J. L. Weiland, E. Wollack, and E. L. Wright. Seven-year Wilkinson Microwave Anisotropy Probe (WMAP) Observations: Power Spectra and WMAP-derived Parameters. *ApJS*, 192:16–+, Feb. 2011.

[24] A. Lewis and S. Bridle. Cosmological parameters from CMB and other data: A Monte Carlo approach. *Phys. Rev. D*, 66(10):103511, Nov. 2002.

[25] V. Lobashev, V. Aseev, A. Belesev, A. Berlev, E. Geraskin, A. Golubev, O. Kazachenko, Y. Kuznetsov, R. Ostroumov, L. Rivkis, B. Stern, N. Titov, S. Zadorozhny, and Y. Zakharov. Direct search for mass of neutrino and anomaly in the tritium beta-spectrum. *Physics Letters B*, 460(1-2):227 – 235, 1999.

[26] P. Madau, F. Haardt, and M. J. Rees. Radiative transfer in a clumpy universe. III. the nature of cosmological ionizing sources. *ApJ*, 514:648–659, 1999.

[27] P. McDonald, U. Seljak, R. Cen, D. Shih, D. H. Weinberg, S. Burles, D. P. Schneider, D. J. Schlegel, N. A. Bahcall, J. W. Briggs, J. Brinkmann, M. Fukugita, Ž. Ivezić, S. Kent, and D. E. Vanden Berk. The Linear Theory Power Spectrum from the Lyα Forest in the Sloan Digital Sky Survey. *ApJ*, 635:761–783, Dec. 2005.

[28] M. McQuinn, A. Lidz, M. Zaldarriaga, L. Hernquist, P. F. Hopkins, S. Dutta, and C. Faucher-Giguère. He II Reionization and its Effect on the Intergalactic Medium. *ApJ*, 694:842–866, Apr. 2009.

[29] B. W. O'Shea, G. Bryan, J. Bordner, M. L. Norman, T. Abel, R. Harkness, and A. Kritsuk. Intoducing ENZO, an AMR cosmology application. In *Adaptive Mesh Refinement – Theory and Applications. Eds. T. Plewa, T. Linde & V.G. Weirs, Springer Lecture Notes in Computational Science and Engineering.* , 2004.

[30] M. Tegmark, M. R. Blanton, M. A. Strauss, F. Hoyle, D. Schlegel, R. Scoccimarro, M. S. Vogeley, D. H. Weinberg, I. Zehavi, A. Berlind, T. Budavari, A. Connolly, D. J. Eisenstein, D. Finkbeiner, J. A. Frieman, J. E. Gunn, A. J. S. Hamilton, L. Hui, B. Jain, D. Johnston, S. Kent, H. Lin, R. Nakajima, R. C. Nichol, J. P. Ostriker, A. Pope, R. Scranton, U. Seljak, R. K. Sheth, A. Stebbins, A. S. Szalay, I. Szapudi, L. Verde, Y. Xu, J. Annis, N. A.

Bahcall, J. Brinkmann, S. Burles, F. J. Castander, I. Csabai, J. Loveday, M. Doi, M. Fukugita, J. R. Gott, III, G. Hennessy, D. W. Hogg, Ž. Ivezić, G. R. Knapp, D. Q. Lamb, B. C. Lee, R. H. Lupton, T. A. McKay, P. Kunszt, J. A. Munn, L. O'Connell, J. Peoples, J. R. Pier, M. Richmond, C. Rockosi, D. P. Schneider, C. Stoughton, D. L. Tucker, D. E. Vanden Berk, B. Yanny, D. G. York, and SDSS Collaboration. The Three-Dimensional Power Spectrum of Galaxies from the Sloan Digital Sky Survey. *ApJ*, 606:702–740, May 2004.

[31] C. Weinheimer, B. Degenddag, A. Bleile, J. Bonn, L. Bornschein, O. Kazachenko, A. Kovalik, and E. Otten. High precision measurement of the tritium beta spectrum near its endpoint and upper limit on the neutrino mass. *Physics Letters B*, 460(1-2):219 – 226, 1999.

[32] W.-M. Yao, C. Amsler, D. Asner, R. Barnett, J. Beringer, P. Burchat, C. Carone, C. Caso, O. Dahl, G. D'Ambrosio, A. DeGouvea, M. Doser, S. Eidelman, J. Feng, T. Gherghetta, M. Goodman, C. Grab, D. Groom, A. Gurtu, K. Hagiwara, K. Hayes, J. Hernández-Rey, K. Hikasa, H. Jawahery, C. Kolda, K. Y., M. Mangano, A. Manohar, A. Masoni, R. Miquel, K. Mönig, H. Murayama, K. Nakamura, S. Navas, K. Olive, L. Pape, C. Patrignani, A. Piepke, G. Punzi, G. Raffelt, J. Smith, M. Tanabashi, J. Terning, N. Törnqvist, T. Trippe, P. Vogel, T. Watari, C. Wohl, R. Workman, P. Zyla, B. Armstrong, G. Harper, V. Lugovsky, P. Schaffner, M. Artuso, K. Babu, H. Band, E. Barberio, M. Battaglia, H. Bichsel, O. Biebel, P. Bloch, E. Blucher, R. Cahn, D. Casper, A. Cattai, A. Ceccucci, D. Chakraborty, R. Chivukula, G. Cowan, T. Damour, T. DeGrand, K. Desler, M. Dobbs, M. Drees, A. Edwards, D. Edwards, V. Elvira, J. Erler, V. Ezhela, W. Fetscher, B. Fields, B. Foster, D. Froidevaux, T. Gaisser, L. Garren, H.-J. Gerber, G. Gerbier, L. Gibbons, F. Gilman, G. Giudice, A. Gritsan, M. Grünewald, H. Haber, C. Hagmann, I. Hinchliffe, A. Höcker, P. Igo-Kemenes, J. Jackson, K. Johnson, D. Karlen, B. Kayser, D. Kirkby, S. Klein, K. Kleinknecht, I. Knowles, R. Kowalewski, P. Kreitz, B. Krusche, Y. Kuyanov, O. Lahav, P. Langacker, A. Liddle, Z. Ligeti, T. Liss, L. Littenberg, L. Liu, K. Lugovsky, S. Lugovsky, T. Mannel, D. Manley, W. Marciano, A. Martin, D. Milstead, M. Narain, P. Nason, Y. Nir, J. Peacock, S. Prell, A. Quadt, S. Raby, B. Ratcliff, E. Razuvaev, B. Renk, P. Richardson, S. Roesler, G. Rolandi, M. Ronan, L. Rosenberg, C. Sachrajda, S. Sarkar, M. Schmitt, O. Schneider, D. Scott, T. Sjöstrand, G. Smoot, P. Sokolsky, S. Spanier, H. Spieler, A. Stahl, T. Stanev, R. Streitmatter, T. Sumiyoshi, N. Tkachenko, G. Trilling, G. Valencia, K. van Bibber, M. Vincter, D. Ward, B. Webber, J. Wells, M. Whalley, L. Wolfenstein, J. Womersley, C. Woody, A. Yamamoto, O. Zenin, J. Zhang, and R.-Y. Zhu. Review of Particle Physics. *Journal of Physics G*, 33:1+, 2006.

Chapter 2

Questioning Lyman-alpha forest results: the intergalactic medium temperature, the ionizing radiation intensity, the temperature-density relation, the matter power spectrum and neutrino mass limits

2.1 Abstract

Some of the best limits on the masses of the normal active neutrinos, and separately warm dark matter particles such as sterile neutrinos, come from observations of the Lyα absorption in the ultraviolet spectra of quasars. These limits are measured by comparing spectra to supercomputer simulations of an intergalactic

medium that was photoionized and heated by ultraviolet photons from stars and quasars. We show that these simulations do not match data on the Lyα at redshift $z \sim 2$. The simulations give the wrong shape for the power spectrum of the flux, and separately they give too little power on intermediate-scales (0.01 s/km, or 3 Mpc) for the measured amount of Lyα absorption. If the data are reliable, as suggested by independent data sets at higher z, then the simulations do not adequately describe the Lyα absorption. We must then question multiple results that rely on these simulations, including the temperature and ionization of the gas in the intergalactic medium, the correlation between temperature and density, the fraction of the volume containing elements made in stars, the power spectrum of the matter and the limits on the masses of the neutrinos. Simulations would be more like data if a larger proportion of their Lyα absorption came from higher density regions, as might happen if those regions were cooler or of lower ionization than in normal simulations.

2.2 Introduction

The spectra of QSOs show hundreds of Lyα absorption lines from neutral hydrogen in higher density regions of the intergalactic medium (IGM) [74, 58]. These lines are redshifted to observed wavelengths $\lambda_{obs} = (1 + z)1216$ Å, so that neutral hydrogen farther from us will be seen at larger wavelengths. The changing redshift means that the spectrum of each QSO shows a forest of Lyα lines that describe the distribution of the neutral hydrogen all along the path from the QSO to us.

We can use the fluctuations in the amount of Lyα absorption as a function of wavelength (or redshift) to measure astrophysical parameters including the temperature and ionization of the IGM, as well as the amplitude of the power spectrum of the cosmological matter density field (the matter power). The amount of Lyα absorption increases with the gas density, and the gas density is tied to the

total matter density [20, 21, 29, 33, 34, 53, 52, 97, 94, 19]. The Lyα forest gives the matter power on smaller scales than galaxies or the cosmic microwave background (CMB), and the density in the IGM fluctuates by factors of only a few on Mpc scales. These density fluctuations are close enough to linear that large hydrodynamic numerical simulations that track the density, velocity, temperature and ionization of the hydrogen and helium in the IGM should give an accurate representation of the Lyα absorption expected for a given primordial matter power spectrum. We estimate the astrophysical parameters and the primordial matter power spectrum amplitude by finding the simulation that makes Lyα absorption most like that in the observed QSO spectra.

We are interested in Lyα forest data sets as probes of inflation, light neutrino masses, warm dark matter (WDM) and IGM thermal history. We consider these four applications in order. First, inflation. The small-scales provide maximum leverage when compared to the large-scale power from the CMB. This comparison tests whether the overall shape of the power spectrum is consistent with the expectation of a tilted power-law with index $n_s \sim 0.95$. Departure from this power-law, such as a running-spectral index (that changes with wavenumber), would tell us about the potential of the inflaton field.

Second, the best upper-limits on the sum of the masses of the three normal active neutrinos, Σm_ν, may come from comparing the power from the Lyα forest on small-scales to the power on much larger scales. Neutrinos with smaller masses remain relativistic for longer, they travel farther and suppress the gravitational growth of structure on larger scales. The neutrinos suppress power across all scales sampled by the Lyα forest. The suppression increases as the scale decreases below the neutrino free streaming wave number $k_{fs} = 0.002(\Sigma m_\nu/0.05 \text{ eV})^{1/2}$ (1/Mpc) [32, Eqn. 1], or $k_{fs} = 10^{-5}$ (s/km), 1000 times larger than the scales we will discuss. At redshift $z = 3.5$ and for $\Sigma m_\nu = 0.05$ eV, the power is suppressed by 1% at $k = 0.03$ (1/Mpc) (or 8×10^{-5} s/km) and 1.9% for $k > 0.6$ (1/Mpc) (or > 0.0017 s/km)[49]. At a fixed wavenumber, the suppression increases with Σm_ν

and with increasing time (decreasing z). For $k > 0.6$ (1/Mpc) the matter power is suppressed by $2.1(\Sigma m_\nu/0.05\text{ eV})\%$ at $z = 1.5$ and by $2.7(\Sigma m_\nu/0.05\text{ eV})\%$ at $z = 0$ [32, 49]. A 2% suppression, corresponding to the minimum Σm_ν allowed by oscillation data, $\Sigma m_\nu = 0.05$ eV, is smaller than could be detected with existing spectra, but a $\sim 20\%$ suppression by neutrinos with $\Sigma m_\nu = 0.5$ eV might be detectable.

Third, the amplitude and shape of the power spectrum on the smallest scales provides some of the best limits on the mass of warm dark matter (WDM). WDM suppresses small-scale power in a similar way to the active neutrinos, but the size and shape of the suppression is dependent on the production mechanism, the mass of the WDM particle, and the mass fraction of the total dark matter that consists of WDM particles[10]. New types of neutrinos with keV masses that are sterile, because they do not have normal weak force interactions, are a favored form of WDM, in part because the most popular explanations for the masses of the active neutrinos all require sterile neutrinos. These ideas are also connected to leptogenesis, through which the baryon asymmetry arises from a lepton number asymmetry [14]. In addition, if there is a small interaction between dark matter and photons, this will suppress power in a similar way as WDM. A constraint (from the suppression of power) on the amount of WDM can be converted into a bound on this interaction cross section, where a dark matter particle of mass 100 GeV and a cross section 10^{-6} times the Thompson scattering cross section suppresses the power like a WDM particle with a mass around 1 keV [4].

Fourth, the Lyα forest absorption contains information on the thermal history of the IGM. The Lyα absorption line widths as well as the amplitude of the power spectrum of the flux in the Lyα forest on the smallest scales ($k > 0.1$ s/km) are sensitive to the temperature of the IGM at and before the time of observation. Higher temperatures increase the doppler broadening of the Lyα absorption and this decreases the small-scale power. Higher temperatures bring increased collisional ionization, a reduction in the mean amount of Lyα absorption and a

decrease in the power on all scales. The gas pressure further reduces the power spectrum on small-scales by opposing the growth of small fluctuations [29, Eqn. 20].

Hydrodynamic numerical simulations are central to measuring the matter power from the Lyα forest because of the complex interplay between the density, velocity, ionization and temperature. In standard IGM simulations, the gas is heated to over 10^4 K at $z > 6$ when it is photoionized. Regions of the IGM with lower densities expand faster and cool faster than higher density regions. By redshifts $z \sim 2$, these standard simulations show a tight correlation between the density and temperature in most of the volume of the IGM [35].

Over the years, many simulations that incorporate this standard description of the IGM have been compared to the Lyα absorption in QSO spectra. While the parameters that specify the simulations can usually be varied to give a match to some of the statistics that describe the Lyα absorption [16, 68, 31, 69, 84, 37, 65], other studies have shown differences that suggest that this physical description of the IGM is incorrect [57, 90, 3, 7].

The immediate goal of this paper is to explore whether any of our standard simulations can make artificial spectra that can match the power spectrum of the flux in data. We attempt to simultaneously match five statistics of the IGM. We work directly with the output from the simulations, and we avoid the common practice of adjusting (post-processing) the outputs from simulations to better match data.

We will describe the hydrodynamic simulations of the IGM and then the cosmological and astrophysical input-parameters that specify these simulations, and the statistical quantities that we use to compare to the Lyα absorption in QSO spectra. We next show how we can predict the values of the statistics that we expect from arbitrary combinations of input-parameters. We find the sets of input-parameters that simultaneously match several of the statistics from data. We find that none of our simulations can match all of the statistics of the Lyα absorption.

In particular, we confirm our earlier finding [90] that the power on Mpc scales in both the low-resolution (Sloan Digital Sky Survey, SDSS) and high-resolution (HIRES on Keck, or UVES on the VLT) spectra is about a factor of 1.5 larger than in the simulations. We end with a discussion of the possible explanations and the implications.

2.3 Hydrodynamic simulations of the intergalactic medium

We use the same hydrodynamic simulations as in [37] where we examined only the mean amount of Lyα absorption and the characteristic Lyα absorption line width. In this paper we also examine the power spectrum of the flux in the Lyα forest that is related to the underlying matter power spectrum. We use the Eulerian (grid based) code ENZO [13, 12, 61, 63, 70, 62]. The Lagrangian code GADGET gives very similar results [64] for the IGM. Our simulations follow the growth of density fluctuations and peculiar velocities, and the heating and ionization due to the ultraviolet background radiation from early stars and later QSOs [98] and shocks from structure formation.

2.3.1 Input-parameters

In table 2.1 we list five input-parameters that we vary from one simulation to another. We will not vary other input-parameters that have small effects over the limited ranges allowed by other measurements. These other parameters include Ω_Λ, Ω_m, and Ω_b, which are the fraction of the closure density in the cosmological constant, in all matter (including baryons), and in baryons alone. We also do not vary the power spectrum scalar slope n_s and the Hubble constant, given by $100h$ km/s/Mpc. We list the fixed values of these other parameters in the first four columns of table 2.2. The standard values for these input-parameters are close to

those preferred by the WMAP 5-year data [24, 45], although we use a larger value of $n_s = 1$.

Table 2.1: The input-parameters that we use to specify our simulations.

Parameter	Description	Range
Box Size L	Length of a side of the simulation cube (comoving Mpc)	19.2-76.8
Cell Size C	Size of the simulation cells (comoving kpc)	37.5-150
X_{228}	Photoheating rate	0.4-5.4
γ_{912}	Photoionization rate	0.5-1.5
σ_8	Present linear matter power spectrum amplitude at $8h^{-1}$Mpc	0.7-1.1

Table 2.2: Standard values for the input-parameters.

Parameter	Standard Value	Parameter	Standard Value	Parameter	Standard Value
Ω'_b	0.044	γ'_{912}	1.3	Box size (L')	76.8 Mpc
Ω'_m	0.27	X'_{228}	1.1	Cell size (C')	18.75 kpc
Ω'_Λ	0.73	σ'_8	0.812	Redshift (z')	1.95
h'	0.71	n'	1.0		

The main differences between our simulations are controlled by three input parameters. The σ_8 is a measure of the amplitude of the primordial matter power. It is the current standard deviation of the density of matter (divided by the mean density) in a sphere of radius 8 h^{-1}Mpc. We use two astrophysical parameters that together adjust both the ionization and heating of the IGM. The parameter γ_{912} is the photoionization rate per neutral hydrogen atom, in units of the rate predicted from known ultraviolet sources and Lyman continuum absorbers by [50]. We expect $\gamma_{912} \sim 1$, unless there are additional unknown sources of ultraviolet photons. We use γ_{912} to adjust the fraction of the H that is neutral and hence the total Lyα absorption.

The parameter X_{228} is the heat input per ionization of He^+, again in units of that expected for the photon spectrum given by [50]. The value of γ_{912} controls the entire ionizing spectrum, including photons that can ionize H and He^+. Our ENZO simulations, like almost all others used to interpret the IGM, are optically-thin with exactly the same intensity of ionizing photons at all places at a given redshift. The X_{228} parameter was introduced to correct for the heat input that might have been experienced in optically-thick gas. By design we expect $X_{228} \sim 1$ will provide the best description of the IGM.

We previously presented the effects of varying box and cell size in [90]. We discovered that the gas in larger simulations is hotter at all densities and especially the largest densities. This is because the larger boxes contain longer density and velocity modes that cannot fit into the smaller boxes and these modes lead to higher flow velocities and more shock heating.

2.3.2 Output-statistics

We compare the simulations and QSO spectra using output-statistics that we measure in both the QSO spectra and in artificial spectra from the simulations. We must make the comparison using statistics because we do not know the initial

density and velocity fields in the specific parts of the IGM that we observe. We make artificial spectra from each simulation using the code described in [102] and in [37]. In this paper we use a set of five statistics that we list in table 2.3.

Table 2.3: Output-statistics used to compare simulations and QSO Lyα spectra.

Statistic	Description
b_σ	Characteristic Lyα absorption line width. Increases with the gas temperature, velocities and the distance across the density fluctuations
τ_{eff}	The amount of Lyα absorption (effective optical depth in the Lyα forest)
$P_{log(k)}$	Power spectrum of the flux in the Lyα forest (the flux-power) at 3 wave-numbers: $log(k) = -2, -1.5$ and -1, with k in (s/km)

The statistic b_σ measures the typical Lyα absorption line doppler width in km s^{-1}. We obtain this statistic by fitting the Hui & Rutledge function [36, Eqn. 5] to the distribution of Lyα absorption line widths, or b-values, where $b = \sqrt{2}\sigma$ and σ is the standard deviation of a Gaussian distribution. Larger values correspond to hotter gas, more bulk motion, and larger absorbing regions (larger difference in Hubble flow across each region).

A second statistic measures the mean amount of Lyα absorption. We first mark the continuum level on each spectrum. The continuum level is the spectrum of flux (erg/cm^2/s/Å) that we expect in the absence of absorption. It varies slowly with wavelength, except in the QSO emission lines. We then divide the flux in each pixel by the continuum level for that pixel, to obtain F1 [42, Eqn. 2], and we average this over all relevant wavelengths and many QSOs [88] to get the mean flux $\bar{F}$. In place of the mean flux, we use the mean effective optical depth, $\tau_{\rm eff} \equiv -ln(\bar{F})$, effective because we averaged over wavelengths and QSOs before we take the natural-log. At redshifts $z \sim 2$, the Lyα absorption removes only $\sim 13\%$ of the flux, and hence $\tau_{\rm eff} \simeq (1 - \bar{F})$ is the fraction of photons absorbed by Lyα transitions. The $\tau_{\rm eff}$ increases when the gas is cooler (less collisional ionization), less photoionized (less ionizing photons per proton) or denser (faster recombination for a fixed photon flux and temperature).

The three other output-statistics are the amplitude of the 1-dimensional power spectrum of the flux overdensity at three wavenumbers, $\log_{10}(k) = -2.0$, -1.5 and -1.0 (s/km). We take the power of the flux overdensity, $\delta F2 = (F1 - \bar{F}1)/\bar{F}1$, [42, Eqn. 3] where $\bar{F}1$ is the average of $F1$ over a segment of spectrum of length $\Delta z = 0.1$ [37] (see [37, §6.3] and [90, §8] for alternatives). We cut each spectrum into segments of this length, we measure the power in each segment and we average these power spectra over segments and QSOs. At a given k, the 1-D power is the integral of the 3-D power over smaller-scales. P_{-2} represents the power on larger-scales (the -2 is the value of $\log_{10}(k)$), large enough to be relatively insensitive to the gas temperature (for a given amount of absorption, [66, Fig.

8,9]) and large enough to be measured in numerous low-resolution spectra, but small enough to fit inside our typical simulation boxes. P_{-1} measures the power on small-scales where the gas temperature and bulk motions are more important. Measurements on scales smaller than this are complicated by absorption from elements other than hydrogen (metal lines [53]) and photon noise [18]. The value of P_{-2} comes in part from the large-scale distribution of matter in the IGM, and in part from shapes of the individual Lyα absorption features, while P_{-1} is almost entirely from the shapes [93, Fig. 1].

2.3.3 Dependence of flux-power on input-parameters

Since we have not run simulations for all sets of parameters that might most resemble data, we instead interpolate and extrapolate from the many simulations that we have run. We now describe how we calculate the output-statistics that we expect to obtain if we were to run a simulation with a particular set of input-parameters. We extend the technique that we first developed in [37] for the output parameters b_σ and $\tau_{\rm eff}$. We give scaling equations between individual inputs and outputs. We vary one input-parameter at a time, keeping the others fixed at standard values given in table 2.2.

We set the standard values as follows. We set σ_8 close to the WMAP 5-year data value [24, 45]. We set the two astrophysical standard input-parameters (γ_{912} and X_{228}) to give output-statistics that match data for four of the five output-statistics, all except the large-scale power P_{-2} (that we cannot match). We set the box size to 76.8 Mpc and the cell size to 18.75 kpc because these are the extremes from our simulations and the differences that would result with much larger boxes or much smaller cells are less than the errors with the observations [90]. If we run a simulation using all these standard input-parameter values, we should obtain the standard output-statistic values that we list in the top row of table 2.4. We have not run this simulation because it would be a 4096 cube that would be near the

limit of existing supercomputers and it would require significant computational time. We do not need to run this simulation because we can predict the output with sufficient accuracy.

Table 2.4: The output-statistics that we expect at $z = 1.95$ from a simulation with standard input-parameters (table 2.2). We list the mean and standard deviations of the statistics that we obtain when we use the scaling equations (§2.3) on the outputs from each of the simulations. We discuss the data in §3.

	P'_{-2}	$P'_{-1.5}$	P'_{-1}	$\tau'_{\rm eff}$	$b'_\sigma(\rm kms^{-1})$
Mean (Sim)	5.11	2.11	0.0827	0.1309	23.56
σ (Sim)	0.18	0.058	0.0043	0.0023	0.27
σ/mean	0.035	0.027	0.052	0.018	0.011
Data	8.8 ± 1.0	2.07 ± 0.14	0.0841 ± 0.0067	0.1335 ± 0.0115	23.6 ± 1.5

To calculate the output-statistic that we expect from a simulation with arbitrary input-parameters, we calculate one scaling factor for each parameter that will not be at its standard value. A scaling factor is a scaling equation from table 2.5 evaluated at the desired input value, divided by the same equation evaluated at the standard input-parameter value. The equivalent equations for τ_{eff} and b_σ are in [37, table 7]. We obtain the output-statistic we expect when we multiply the output of a simulation by the scaling factors. For example, the power we expect for a box of size L is $P_{-2} = P'_{-2}P_{-2}(L)/P_{-2}(L')$, where $P'_{-2} = 5.11$ is from table 2.4, $P_{-2}(L) = 3.28 + 0.135L^{0.600}$ is the power we expect for a box of size L, and $P_{-2}(L') = 3.28 + 0.135(L')^{0.600} = 5.106$ is the power for size $L' = 76.8$ Mpc.

Table 2.5: Scaling relationships that predict the output flux power P_{logk} for user chosen input-parameters all at $z = 1.95$.

Parameter	P_{-2}	$P_{-1.5}$	$log(P_{-1})$
Box size (L)	$3.28 + 0.135L^{0.600}$	$1.76 + 9.63 \times 10^{-6}L^{2.42}$	$2.05 - 3.00L^{0.00948}$
Cell size (C)	$4.03 + 0.314C^{0.423}$	$2.13 - 0.000225C^{1.47}$	$-1.07 - 0.000141C^{1.55}$
X_{228}	$8.10 - 2.91X_{228}^{0.287}$	$5.02 - 2.85X_{228}^{0.213}$	$-0.0804 - 0.968X_{228}^{0.372}$
γ_{912}	$1.08 + 4.97\gamma_{912}^{-0.794}$	$0.0879 + 2.51\gamma_{912}^{-0.828}$	$-0.156 - 0.801\gamma_{912}^{0.559}$
σ_8	$6.70 - 1.96\sigma_8$	$2.93 - 1.01\sigma_8$	$-0.825 - 0.317\sigma_8$

In table 2.4 we list both the mean and standard deviations of the output-statistics that we expect when we scale each simulation to the standard input-parameter values. The standard deviations are 1–5% of the mean values, showing that the cross-terms between the input-parameters are small. We can then vary all the input-parameters simultaneously by multiplying scaling factors together. For example, the power we expect for input-parameters L, C, X_{228}, γ_{912}, and σ_8 is

$$P_{-2} = P'_{-2} \frac{P_{-2}(L)}{P_{-2}(L')} \frac{P_{-2}(C)}{P_{-2}(C')} \frac{P_{-2}(X_{228})}{P_{-2}(X'_{228})} \frac{P_{-2}(\gamma_{912})}{P_{-2}(\gamma'_{912})} \frac{P_{-2}(\sigma_8)}{P_{-2}(\sigma'_8)}. \tag{2.1}$$

Figures 2.1 and 2.2 show the power after and before we apply the scaling equations. Each simulation is shown as a point in each panel. Figure 2.1 shows that the scaling equations provide an accurate description of the simulations. We found the scaling equations by first fitting a curve to each panel in figure 2.2. We used these interim equations to scale all the other panels in a row. We then iterated until the equations converged.

The trends in figure 2.1 have physical interpretations. The top left panel shows that larger boxes give spectra with more large-scale power, because they contain larger modes [90]. The top and bottom panels in the cell size column show trends that we previously noted [37, figure 7]. Increasing X_{228} heats the gas, leaving less neutral hydrogen [37, figure 24], less Lyα absorption and hence less power on all scales. Increasing γ_{912} has the same effects through photoionization of the neutral hydrogen. The last column shows that the flux-power decreases on all scales when the matter power (σ_8) is increased. This counter-intuitive anti-correlation arises because the increase in σ_8 makes the $\tau_{\rm eff}$ fall ([37] figure 20), which causes the flux-power to fall by more than the increase caused directly by the σ_8 increase. Comparing the top two rows, we see that the intermediate-scale and large-scale power are more sensitive to γ_{912} (and hence to $\tau_{\rm eff}$) than to the other input-parameters (including σ_8) for the ranges that we show. This illustrates the most important trait of the flux-power [19, 88, 94], that it is to first order a

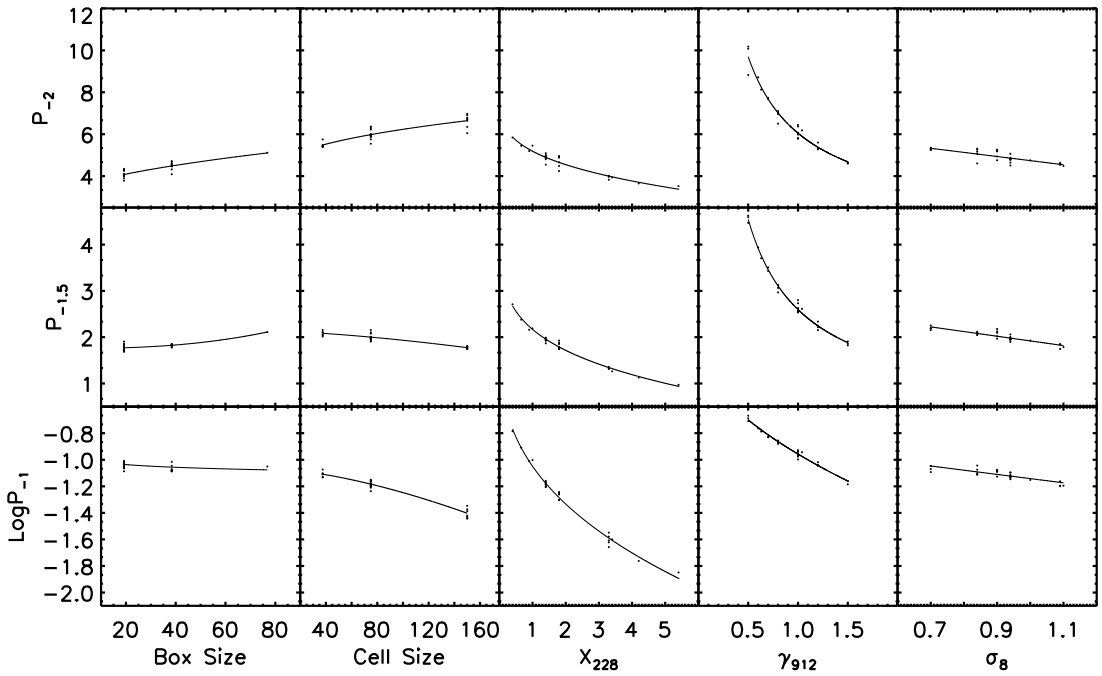

Figure 2.1: Power (vertically) of the Lyα flux (km/s) in spectra from simulations of the IGM as a function of simulation input-parameters (horizontally). In each frame we show each simulation as a point. We used the equations in table 2.5 to scale the power that we measured from each simulation to the values we expect for the standard input-parameters in table 2.2. The curves show these equations. For each column, we do not scale the points by the quantity given on the horizontal axis of that column. The small scatter of points about the curves demonstrates the accuracy of the scalings.

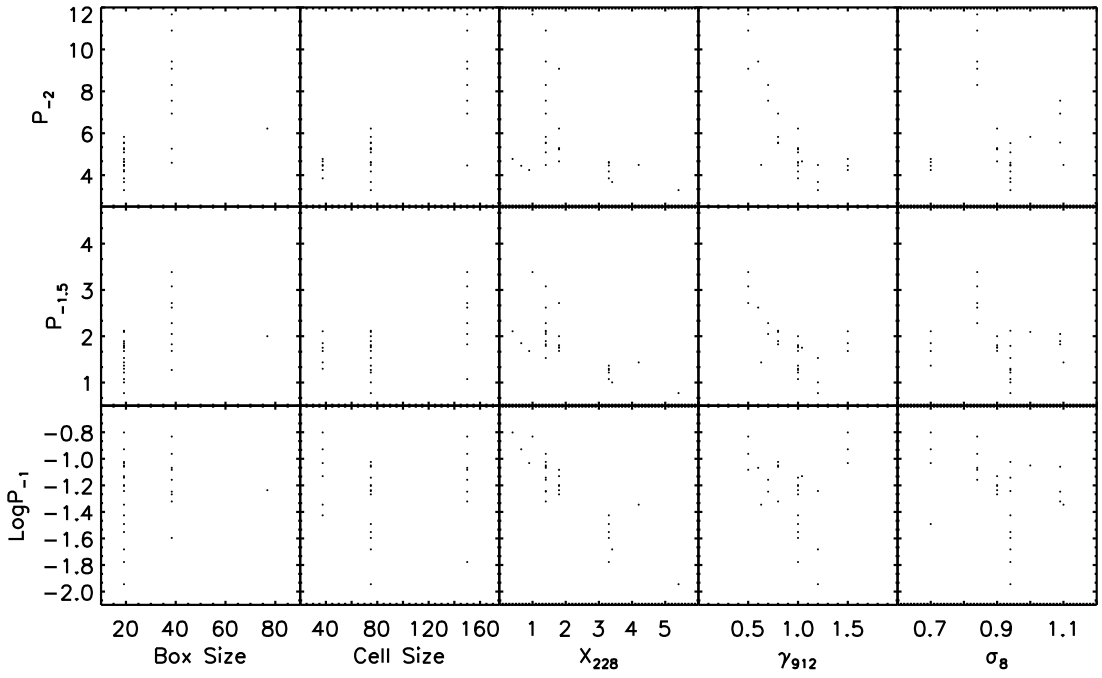

Figure 2.2: As figure 2.1, but now showing the raw unscaled flux-power, again with one point per simulation. All simulations appear in each panel and in general the simulations differ in all the input-parameters, not only that shown on the horizontal axis of a given panel.

measurement of the mean amount of Lyα absorption. Reference [56] showed that it is possible to break the degeneracy between the matter power (σ_8) and the γ_{912} because the shape of the power spectrum is sufficient to specify both parameters. As γ_{912} increases, the power spectrum becomes steeper, with the ratio $P_{-2}/P_{-1.5}$ increasing from 2.13 to 2.49 as γ_{912} increases from 0.5 to 1.5. This ratio also increases as σ_8 increases, but by different factors.

2.4 Comparison of the simulated and observed Lyα forest

The curves in figure 2.1 showed how the flux-power changes when we change one of the five inputs and we keep the others constant. This does not tell us how to find a simulation that simultaneously matches all output-statistics from data because a change in one input typically causes changes in all the outputs. In this section we simultaneously adjust three inputs to keep selected outputs constant at the values in table 2.4 from QSO spectra.

We use the same data values as [37]. Our simulations do not correctly simulate high column density absorbers and they do not include metal absorption, and so we remove these absorbers from the data. The observed flux-power was taken from [41] who excluded absorption by Lyα lines with neutral hydrogen column densities of log N_{HI}> 19.5 (cm^{-2}). Reference [37, Table 4] interpolated the power to $z = 1.95$ and they removed flux-power from absorption due to metals. According to [41, Fig. 3], at $z = 2.36$ metals contribute 20% of the power at $k = 0.1$ (s/km) and $\sim 7\%$ at $k = 0.01$ (s/km). We calculated the value of b_σ from the distribution of widths (b-values) of Lyα lines with $12.5 <$ log N_{HI}< 14.5 (cm^{-2}) [40, Fig. 10]. For $\tau_{\rm eff}$, we use the data from [89, 88] that includes only the absorption from the low density IGM, and not that from metal lines or the Lyα lines of Lyman limit absorbers with log N_{HI}> 17.2 (cm^{-2}) that we have not correctly simulated [90].

2.4.1 Matching the mean amount of absorption and typical line width

We first find sets of simulations that simultaneously match two statistics from data. Figures 25 and 26 of [37] showed that by reducing γ_{912} as σ_8 increases it is possible to obtain a set of simulations all with the same (observed) value of $\tau_{\rm eff}$. Figures 37, 38 and 39 of [37] showed the sets of values for X_{228}, γ_{912} and σ_8 that together give simulations that match both $\tau_{\rm eff}$ and b_σ simultaneously. With larger σ_8 we need larger X_{228} (to offset the narrower Lyα lines from larger σ_8) and smaller γ_{912} (to offset the reduced neutral hydrogen from larger X_{228} and the reduced $\tau_{\rm eff}$ from the larger σ_8 [88, §12.1.1]).

In figure 2.3, the solid red curves show the values that inputs X_{228}, γ_{912}, and σ_8 should take to simultaneously match measurements of $\tau_{\rm eff}$ and b_σ. The two other curves show the effects of moving the measurements by 1σ. As [37] showed, we have no trouble finding sets of input-parameters that give simulations that can simultaneously match the observed $\tau_{\rm eff}$ and b_σ; but this success is misleading because we cannot simultaneously match a third statistic such as the power.

2.4.2 Matching the mean amount of absorption, typical line width and flux-power

Reference [37, Fig. 40] showed that the power of the flux in the Lyα forest is larger in data than in some simulations, while reference [90] showed that this was not because simulations boxes were too small. We will now see that these results apply to simulations in general, even when we arbitrarily change the input-parameters to look for a match.

In figure 2.4, we attempt to match the flux-power in addition to $\tau_{\rm eff}$ and b_σ. To do this, we use the scaling technique of section 2.3.3 to scale the power to the sets of inputs that we know from figure 2.3 simultaneously match both $\tau_{\rm eff}$ and b_σ.

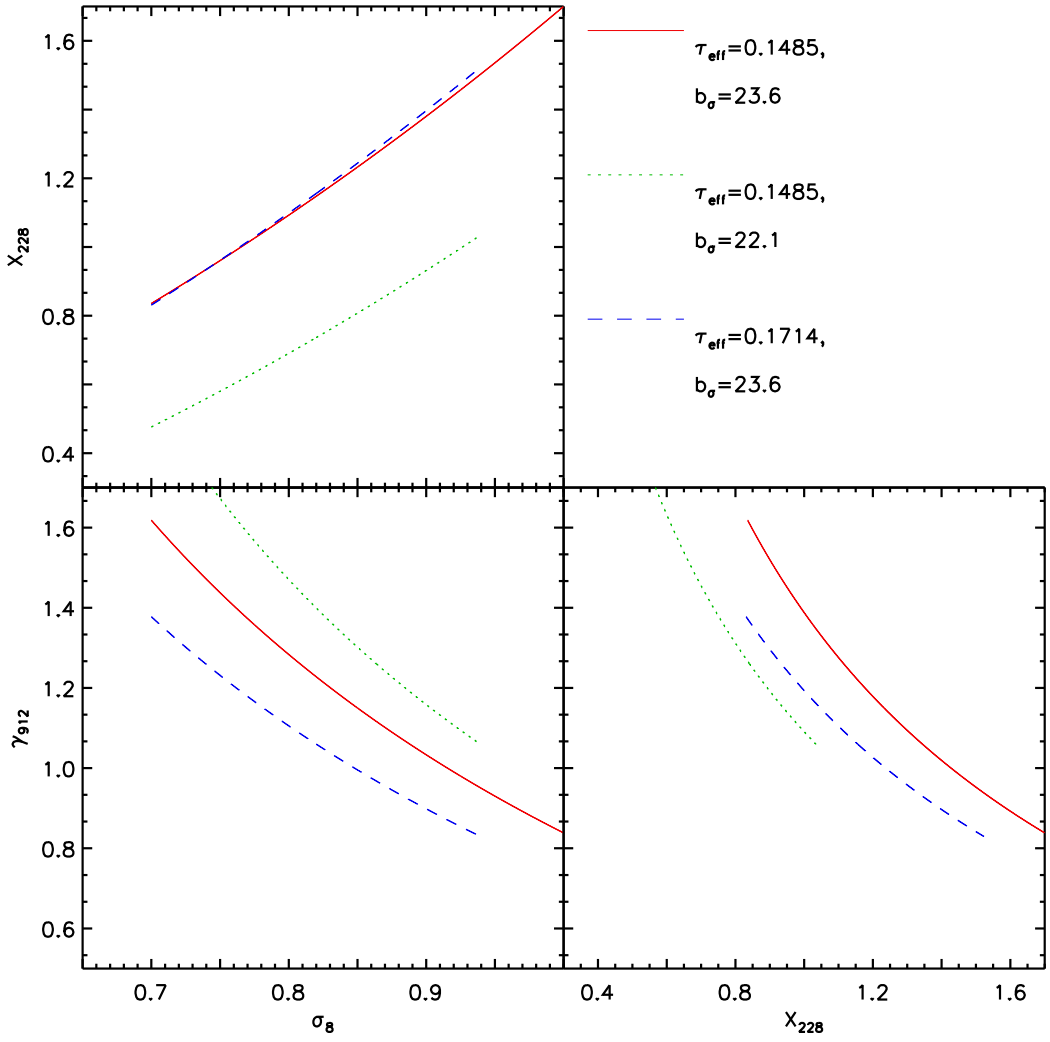

Figure 2.3: Projections onto the three faces of a cube showing the input-parameters (γ_{912}, X_{228}, and σ_8) for simulations that give simulated spectra that match the observed values for τ_{eff} and b_σ (solid red curves). The dotted (pale green) curve matches $b_\sigma - 1\sigma$, and the dashed (dark blue) curve $\tau_{\rm eff} + 1\sigma$.

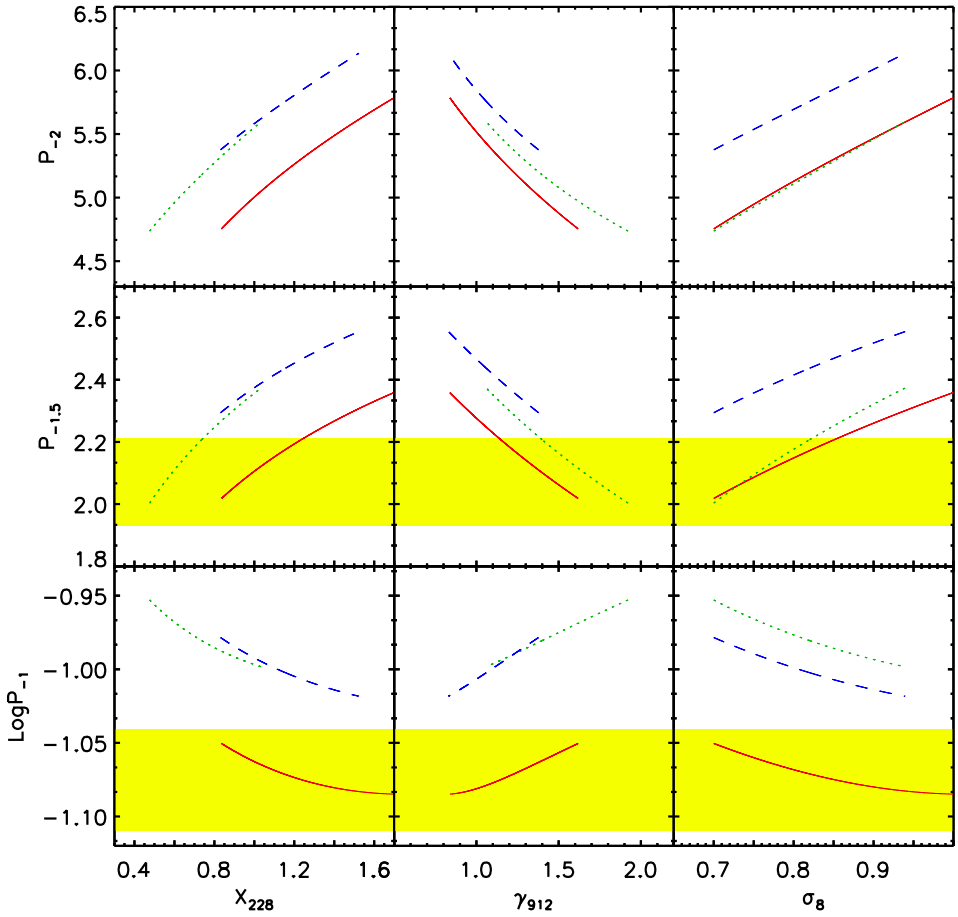

Figure 2.4: Power of the flux (km/s) in simulated spectra that lie on the lines defined in figure 2.3. In each panel, we vary the 3 input-parameters simultaneously, although we show only one at a time on the x-axis. The horizontal yellow bands on the lower two rows show the 1σ range of the observed power. The equivalent band for the top row is far off the top of the panels at $P_{-2} = 8.8 \pm 1.0$ (km/s).

Let us discuss some of the trends in figure 2.4. In figure 2.1 (where we adjusted only one input at a time and we allowed the outputs to float), the gradients of P_{-1}, $P_{-1.5}$ and P_{-2} with X_{228}, γ_{912} and σ_8 were all negative. Now in figure 2.4 five of these nine gradients have reversed sign, and the gradients of P_{-1} now have the opposite sign to the gradients of the other two powers. The different gradient for P_{-1} compared to the larger-scale powers means that increasing σ_8 (while we simultaneously increase X_{228} and decrease γ_{912}) will change the shape of the power spectrum, giving more power on larger-scales.

In figure 2.3, the relative displacements of the lines illustrate the sensitivity to the input-parameters. The top panel shows that if we decrease X_{228} or increase σ_8, we obtain a lower b_σ, moving, for example, from the solid (red) to the dotted (green) line. The two lower projections show how we should simultaneously adjust the γ_{912} if we want to keep the $\tau_{\rm eff}$ unchanged.

Figure 2.4 shows that a wide range of models, those along the solid line on the lower row of panels, can simultaneously match the $\tau_{\rm eff}$, b_σ and the P_{-1} from data. We cannot match all three if either the b_σ is lowered to 22.1 km s^{-1} (dotted green lines) or $\tau_{\rm eff}$ is raised to 0.145 (dashed blue lines). This suggests that the observed values for $\tau_{\rm eff}$, b_σ and P_{-1} are mutually-consistent and consistent with our simulations. These statistics alone place tight constraints on the input-parameters.

The middle row of figure 2.4 shows that only simulations with $X_{228}< 1.2$, $\gamma_{912}> 1.2$ and $\sigma_8< 0.85$ (those lying on the solid red line in the shaded yellow region) can match $\tau_{\rm eff}$, b_σ and the $P_{-1.5}$. These simulations all also match P_{-1}. Again, we cannot match b_σ and $P_{-1.5}$ if $\tau_{\rm eff}$ is raised to 0.145.

The top row of figure 2.4 shows that there are no simulations that match $\tau_{\rm eff}$, b_σ and P_{-2}. The large-scale power in all our simulations would remain below the observed value even if $\tau_{\rm eff}$ or b_σ were to change by several σ. The dashed blue line shows that by increasing the $\tau_{\rm eff}$ we can increase the P_{-2} to improve the match. However, this is not a solution, because linear extrapolation of the increase in P_{-2} shown in the top right panel of figure 2.4 shows we would need to increase

$\tau_{\rm eff}$ by 7σ to give $P_{-2} \simeq 8.8$, and such a large change is ruled out by mean flux measurements. In addition, the lower two rows show that such simulations would then have too much power at both $P_{-1.5}$ and P_{-1}. We also see from figure 2.4 that changing the b_σ in data does not have a large effect on the large-scale power, and hence this is unlikely to make data and simulations match.

2.4.3 Combined constraints

We saw in figure 2.4 that we can match the observed values of four but not all five statistics. We now explore in more detail the constraints that these statistics place on the input-parameters.

In figure 2.5, we show the values for three input-parameters (X_{228}, γ_{912} and σ_8) that simulations require to make artificial spectra that match the values for pairs of output-statistics. Since we have five statistics, we can make ten different pairings. We only show seven of the ten in the figure because there are no input-parameter values that match the large-scale power P_{-2} together with one of $\tau_{\rm eff}$, $P_{-1.5}$ or P_{-1}. The remaining match of P_{-2} with b_σ (shown by the solid line 7 in the lower parts of the lower two panels) is unusual in that it required values of γ_{912} less than half those required by the other pairs of statistics.

The closeness of the three lines in figure 2.5 that match ($\tau_{\rm eff}$ and P_{-1}, line 3), (τ_{eff} and b_σ, line 4) and (b_σ and P_{-1}, line 5) in all three panels shows that any two of these three statistics contains almost all the information in the third. Although this suggests that P_{-1} is largely determined by the combination of the line widths (b_σ) and the total amount of Lyα absorption ($\tau_{\rm eff}$), we will see later that b_σ does contain more information than is in the combination of $\tau_{\rm eff}$ and P_{-1}.

Near the left edge of the two lower panels of figure 2.5 we see that six of the seven lines pass through a small volume where the inputs are close to X_{228}= 0.96, γ_{912}= 1.47 and σ_8= 0.74. This means that simulations that use these input-parameters will match four of the five statistics, all except the large-scale power

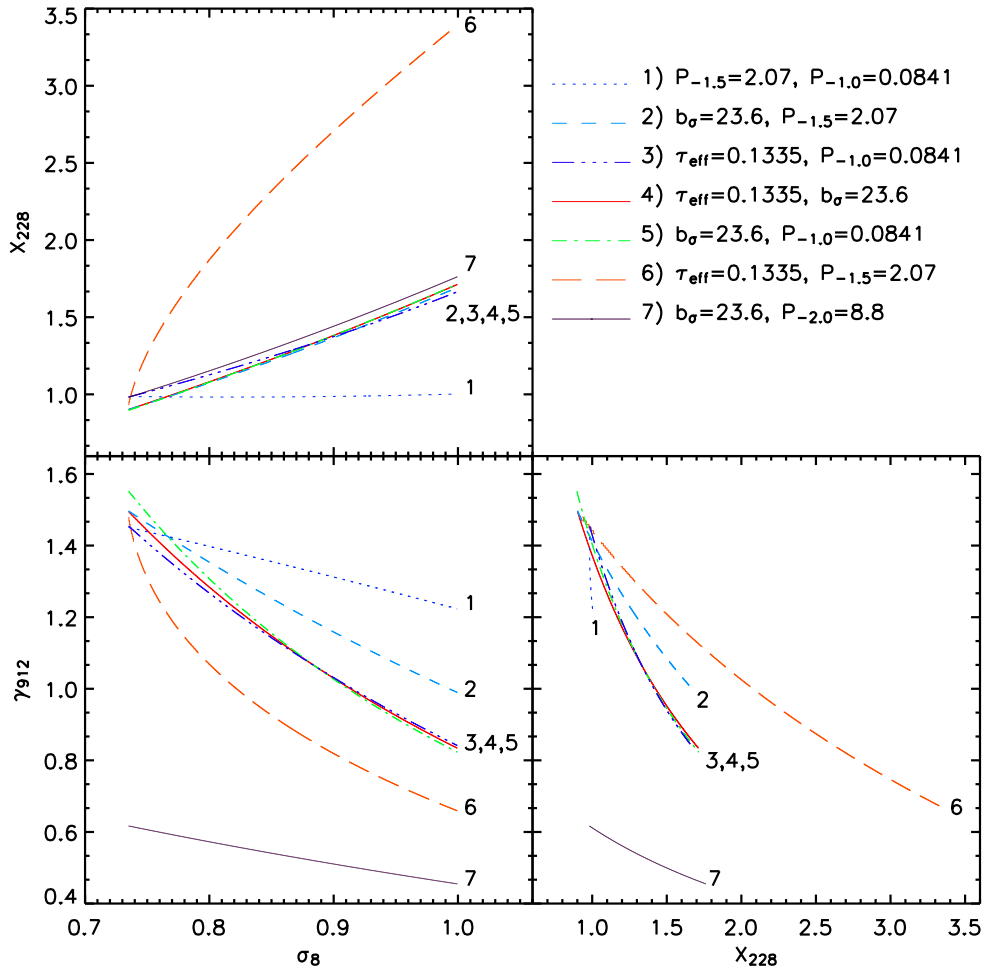

Figure 2.5: Projection of the three faces of a cube showing the values of γ_{912}, σ_8, and X_{228} that give simulated spectra that match various statistics from QSO spectra. Only if lines intersect can the simulated output-statistics match three or more statistics from observed data. We do not show lines for simulations that can match P_{-2} and any one of $P_{-1.5}$, P_{-1}, or τ_{eff}, because there are no such simulations. The scaling equations that we used to make this figure employ input-parameters (σ_8=0.9, γ_{912}=1.0, X_{228}=1.4) from [37] that differ slightly from those in table 2.2 because the latter did not give solutions for $\tau_{\rm eff}$ and $P_{-1.5}$. In general, we expect that the three input-parameters do not give enough freedom to be able to simultaneously exactly match several point statistics, with no errors.

P_{-2}. We set the standard model input-parameters that we list in table 2.2 to be similar to the values where the curves overlap, or more precisely, where the simulations give the same values of the statistics as does the Lyα absorption in QSO spectra.

In figure 2.6, we show the values of the astrophysical input-parameters for simulations that give artificial spectra that match each of the five statistics of the Lyα forest data. The widths of the bands show the approximate $\pm 1\sigma$ error ranges for the data from table 2.4. The vertical band is the limit given by the Lyα line widths; vertical because the value of γ_{912} has a minimal effect on the gas temperature [37, Fig. 23]. The figure shows that there are no simulations that can match the large-scale power at the same time as either the power on smaller scales or the total absorption.

In figure 2.7, we see the effect of increasing σ_8 from 0.812 to 1.0, a value that is 5.7σ above the value from WMAP 5-year data alone (0.796 ± 0.036 [24]) and 7σ above the value of 0.817 ± 0.026 for the combination of the WMAP 5-year data and data on the baryonic acoustic oscillations and supernovae distances [45, 67, 46].

Increasing σ_8 lowers the γ_{912} required to match both the power (on all scales) and the $\tau_{\rm eff}$. We also need larger X_{228} to maintain lines with the observed b_σ (see §3.1). While the curves are closer, they do not overlap even by $\sigma_8 = 1.1$, the largest value that we examined.

The improvement in the fit to the large-scale power with large σ_8 values is not enough to convince us that the Lyα forest prefers a large σ_8 value. Rather, we think that it is an accident that large σ_8 values compensate for some other problem with the data or simulations. From a larger perspective, the larger σ_8 does not improve the agreement between the simulations and data in general because we then also have the added penalty of being many σ away from the σ_8 values preferred by other data.

We previously saw in figure 2.5 that any pair of statistics from the triad b_σ, $\tau_{\rm eff}$ and P_{-1} contains almost all the information (on X_{228} and γ_{912}) in the third

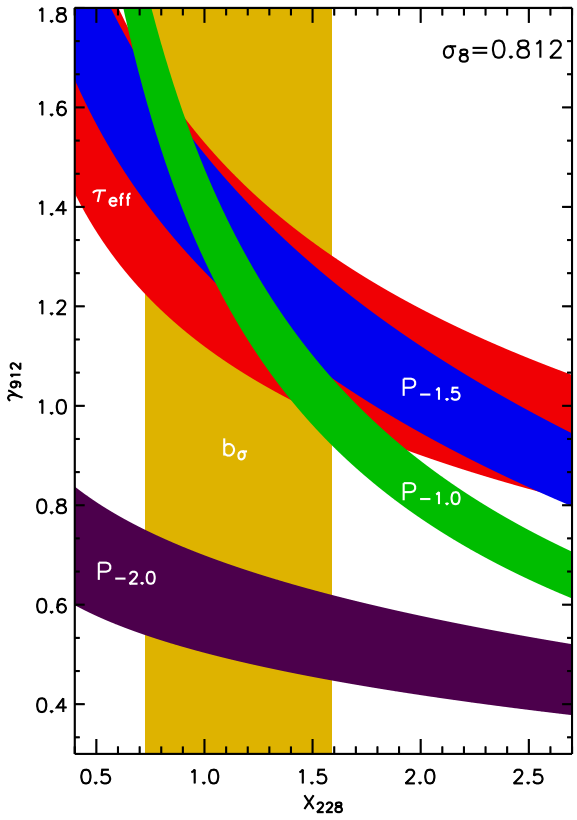

Figure 2.6: Simulations with input-parameters in a colored band match a statistic of the Lyα forest data. A simulation with heating X_{228} and photoionization rate γ_{912} that lies on the edge of a band gives that statistic $\pm 1\sigma$ from the data value in table 2.4. Hotter simulations are on the right, and more ionized ones at the top. The color scheme is as follows: P_{-2} = purple, $P_{-1.5}$ = blue, P_{-1} = green, τ_{eff} = red, and b_σ = mustard. Where the bands overlap, the simulations match more than one statistic. There are no simulations that match all statistics.

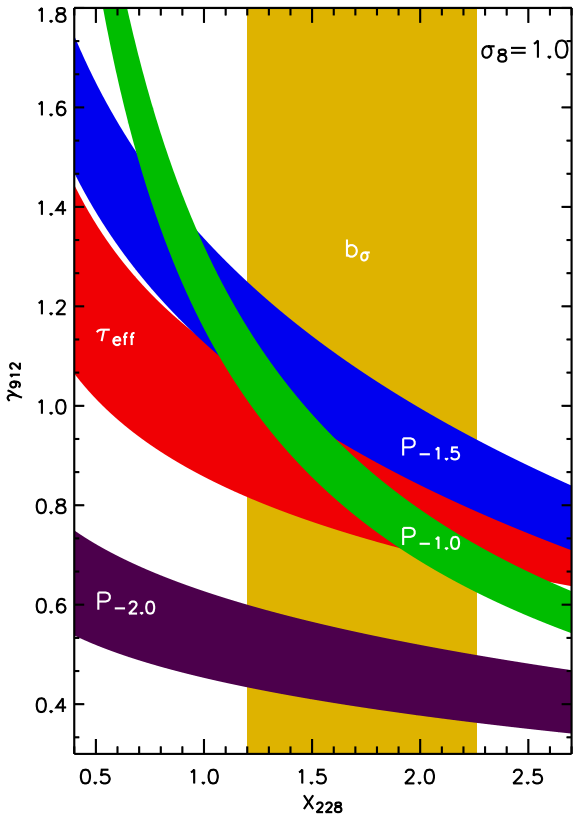

Figure 2.7: As figure 2.6, but with $\sigma_8 = 1.0$, that does not improve the match to data because this σ_8 value is multiple σ from other data sets. From top to bottom on the left side, the (top, middle and bottom) of the bands give simulations that match the following data values: (P_{-1} = 0.0774, 0.0841, 0.0908 km/s), ($P_{-1.5}$ = 1.93, 2.07, 2.21 km/s), ($\tau_{\rm eff}$= 0.122, 0.1335, 0.145) and (P_{-2} = 7.8, 8.8, 9.8 km/s). From left to right across the vertical band the simulations give (b_σ= 22.1, 23.6, 25.1 km s^{-1}).

statistic. We now see this again in figures 2.6 and 2.7 where the centers of the bands for b_σ, $\tau_{\rm eff}$ and P_{-1} (corresponding to the lines in figure 2.5) pass near to a point in the plane for either σ_8= 0.812 or 1.0. Moreover, the center of the P_{-1} (green) band passes near the intersection of one pair of edges of the $\tau_{\rm eff}$ and the b_σ bands (X_{228}= 0.72, γ_{912}= 1.7 for σ_8= 0.812), and then again near the other pair of edges near (X_{228}= 1.49, γ_{912}= 0.97 for σ_8= 0.812) and we see a similar pair of intersections for σ_8= 1.0. In other words, similar areas in the X_{228} – γ_{912} plane are required by the $\pm1\sigma$ ranges for any pair of the three statistics. These relations are a property of the simulations, and not an artifact of the method that we used to arrive at this plot.

We can understand the correlations amongst this triad of statistics. We know that b_σ lacks information on both the number of Lyα lines and their depths, and hence it is complemented by $\tau_{\rm eff}$ or P_{-1}. Similarly, $\tau_{\rm eff}$ lacks information on the line widths and clustering, and we can obtain this from either b_σ or P_{-1}. It is less clear why P_{-1} is lacking in information, since it is very sensitive to both the mean absorption ($\tau_{\rm eff}$) and to line shapes (b_σ). The key is how a spectrum changes as we move along the P_{-1} band, from the upper left where we have a few (large γ_{912} leaves less H I) narrow (small X_{228}) lines that make too little absorption (especially for σ_8= 1.0), to the lower right where we have many shallow lines and too much absorption. We can then complement P_{-1} using information from either b_σ or $\tau_{\rm eff}$ to disallow spectra at either end of the P_{-1} band where both the line widths and the mean amount of absorption do not match data.

Figure 2.6 further shows that other combinations of statistics are also partly redundant, since $\tau_{\rm eff}$, $P_{-1.5}$ and to a lesser extent P_{-1} all place similar demands on the two astrophysical parameters, X_{228} and γ_{912}.

2.4.4 Disagreements between data and simulations

We have shown that we can establish that simulations do not match data using only two output-statistics: the large-scale power P_{-2} and any one of $\tau_{\rm eff}$, $P_{-1.5}$ or P_{-1}. From P_{-2} and $\tau_{\rm eff}$ alone, we conclude that the simulations have too little power on large-scales for the mean amount of Lyα absorption. From P_{-2} and either $P_{-1.5}$ or P_{-1} we see that the simulated flux-power spectrum has the wrong shape; it is not steep enough. Figures 2.4, and [90, Fig.46,47]) show that the flux-power spectrum of the data rises faster (as the scale increases from wavenumbers $k = 0.1 - 0.03$ to 0.01 (s/km)) than the power from the simulated spectra.

What changes to the data would improve the match to the simulations? In figure 2.6, the bands are independent and fixed by their individual measurements. If we can change only one data value, the large-scale power is the only one that can improve the match.

A change to $\tau_{\rm eff}$ alone does not improve the match for three reasons; the change required is unreasonably large (§3.2), it would cause other mismatches, and we can establish the mismatch without using $\tau_{\rm eff}$.

A change to b_σ alone is also not going to improve the mismatch. We saw in figure 2.4 that a change in the measured b_σ value does not help match the large-scale power, and again, we can establish the mismatch without using b_σ.

2.5 Explanation for disagreements between Lyα forest data and simulations

Here we speculate on why the simulations do not match the statistics of the Lyα forest in QSO spectra. Following [90], we consider four classes of explanation: data, simulations, astrophysics and cosmology.

2.5.1 Data

First, the data may be inadequate. The large-scale power is the most obvious suspect, especially because the mismatch manifests over only a factor of 3 change in the wavenumber. Yet there are good reasons to accept that the power is valid; other measurements of the power agree in the sense of the mismatch, and at least two other statistics of the Lyα forest also do not match simulations.

Decreasing the measured large-scale power from 8.8 ± 1.0 to 5.11 would allow simulations to match all the data that we are considering. Although this is approximately a 3.7σ reduction, the errors are not well known, and this seems the most likely change to data that could bring the simulations and data into agreement.

However, three different measurements of the power at $logk = -2$ (s/km) are all above the power in the simulations. We use $P_{-2} = 8.8 \pm 1.0$ (km/s) from [41, 37]. Reference [90, Fig. 46,47] shows two other estimates of the power at $z = 2$ that are systematically larger than from simulations. The power estimate called PJ05 [37, §6.4] has $P_{-2} = 11.1$ (km/s) from high resolution spectra of six QSOs, while extrapolating the power from the SDSS spectra [55] from $z = 2.2$ down to $z = 2$ gives $P_{-2} = 6.9$ (km/s). For both these estimates, the power in data increases to about 1.5 times that in simulations as the wavenumber decreases from 0.01 to 0.001 (s/km).

A second statistic that does not match simulations is the number of Lyα lines as a function of their log N_{HI}, the column density distribution [87]. Figure 15 of [90] shows that simulations have too many absorption lines with small column densities (log $N_{HI} < 14$ cm^{-2}) and too few with large columns (log $N_{HI} > 16.9$ cm^{-2}). The latter come from regions of higher gas density, they make saturated Lyα absorption lines, and hence they will contribute more power per photon absorbed than do the lower column density (unsaturated) lines.

A third statistic that shows disagreement between simulations and data is

the distribution of the flux per pixel in a spectrum, the flux pdf. Reference [57] could not simultaneously match the flux pdf, the column density distribution and the b-value distribution, perhaps because the absorbing gas in their simulations was not hot enough [58, Fig. 17]. Reference [3] showed, and reference [39] confirmed that simulations have too few pixels where Lyα absorbs most of the flux. There are more places in spectra that have large amounts of Lyα absorption than in GADGET simulations [3], while [90, Fig. 10] showed a very similar disagreement, with too few pixels where 75–95% of the flux is absorbed in ENZO simulations.

The mismatch between the simulations and data in three different statistics could all have a single origin. The lack of high column density lines in simulations is a remote possibility. Lines need log $N_{HI}>$ 13.6 cm^{-2} to absorb $>$ 75% of the flux per pixel, and such lines arise in denser regions that we expect give the most flux-power per unit absorption. These lines likely have $13.6 <$ log $N_{HI} < 16.9$ cm^{-2} because we have excluded from QSO spectra most of the Lyα lines with column densities log $N_{HI}>$ 16.9 (cm^{-2}) where we know the simulations lack lines compared to data. The b_σ values use only lines with $12.5 <$ log $N_{HI}<$ 14.5 (cm^{-2}) and are not affected. We removed Lyα lines with log $N_{HI}>$ 17.2 (cm^{-2}) (and metal lines) from the $\tau_{\rm eff}$ measurement [88] leaving very few (from 16.9 – 17.2) remaining in the data where simulations are deficient. The power estimate PJ05 also excluded Lyα lines with log $N_{HI}>$ 17.2 (cm^{-2}) and metal lines. The power PF2I from [37, Table 4] that we use throughout this paper excluded Lyα lines with log $N_{HI}>$ 19.5 (cm^{-2}) and metals, while the SDSS power excluded the mean power from very strong Lyα lines, the typical metal lines and Si III absorption alone.

2.5.2 Simulations

A second class of explanations of why the simulations do not match data is that the simulations inadequately model known physics, especially the ionization and simultaneous heating of the IGM.

The photoionization of He^+ to He^{2+} occurs at $z \sim 3$ and might have a large effect on the temperature of the hydrogen that makes the Lyα forest at those redshifts [71, 86]. If the higher density regions ionize first [27] then they will have longer to cool adiabatically (in the Hubble expansion) and will be cooler by $z = 1.95$ than if the ionization occurred at the same time for all densities. We will then get more Lyα absorption from the higher density regions that we have argued will increase the power from a given amount of absorption. Lower temperatures for the higher density regions will also reduce the pressure smearing, allowing higher densities and deeper absorption lines [66, §4.1]. Both trends would reduce the disagreement between the simulations and data.

A second class of explanation of the mismatch is that the simulations lack the resolution and radiation transfer required to follow the fragmentation and cooling in denser regions [90, §12]. In a simulation with 2 h^{-1} kpc resolution, [44] were able to match the number of absorption systems with log N_{HI}> 17 cm^{-2}. Their simulation was in a box of size 4 h^{-1} Mpc that is too small to measure the Lyα forest. Perhaps a similar simulation of a large volume might match Lyα forest data.

The Lyα forest at $z = 1.95$ in our optically-thin simulations is insensitive to the details of the H ionization epoch. For example, [90, Fig. 48] found that changing the epoch of photoionization from 7 to 9 had a negligible effect on the Lyα forest at $z = 2$.

We do not suspect errors in the codes. In [90] we demonstrated the consistency of our ENZO simulations for a full range of Lyα forest statistics. Direct comparisons of ENZO to the independent GADGET code give very similar results [64]. Lidz (private communication) found essentially the same power from GADGET as we show in [90] from ENZO, while the flux pdf from ENZO [90, Fig. 10] is essentially identical to that shown by [7] from GADGET.

2.5.3 Astrophysics

As a third class of explanation, we may have misunderstood how the IGM is ionized and heated. Nearly all simulations assume that the IGM is ionized by the ultraviolet photons from early stars and later black holes that appear as active galactic nuclei and QSOs. The origin of the ionizing photons remains uncertain because sources at $z \sim 11$ are too faint for existing telescopes, and we have not been able to find the required number of sources at even $z \sim 6$ [82, 9]. The simulations might not match data because there is significant ionization or heating from other sources, such as X-rays [72, 8], cosmic rays [73], decaying particles [77, 81] or winds that flow out from galaxies [17, 85, 5, 51, 48].

Both the radiative transfer in the He^+ ionization and alternative heating mechanisms could invalidate the common assumption that there is a tight correlation between the temperature and density in the IGM [6]. If the temperature is not tightly correlated with the density, then most published attempts to measure the matter power from the Lyα forest will be invalid.

2.5.4 Cosmology

Finally, the cosmological model could be wrong. Major changes might include changes in the primordial power spectrum, the addition of warm dark matter, decaying dark matter, evolving dark energy, and violations in general relativity on cosmological scales.

We saw in the right hand column of figure 2.4 that an increase in σ_8, while we adjust X_{228} and γ_{912} to hold $\tau_{\rm eff}$ and b_σ constant, does make the shape of the flux-power spectrum more like data, with more power on large-scales. However, we also saw that values of $\sigma_8 > 1.1$ would be needed, such values might not match all the statistics, and such large σ_8 values are inconsistent with other data. Instead we would need a change in the primordial power other than the general increase parameterized by σ_8.

A change in the overall tilt of the primordial power spectrum is also unlikely to help simulations match data. In slow roll inflation, the deviation of the primordial power spectrum from scale invariance ($n_s = 1$) depends on how slowly the inflaton field rolled and on the strength of the damping. From [92, Fig. 3] we see that decreasing the n_s from 1.0 to 0.95 decreases the large-scale P_{-2} power by about 3%, a change in the wrong direction and too small by a factor of ten.

Deviation from a power law, or running, can be as large as $n_s - 1$ [23]. If there are fewer than 30 e-foldings of expansion during inflation, then the scalar index n_s can (but does not have to) change with $dn_s/dlnk \leq -0.02$ [25]. However, this is an insufficient number of e-foldings to account for the large-scale homogeneity and isotropy of the universe, whether inflation occurs before the electroweak phase transition, or at the GUT scale. Larger values for the running of the spectral index require a more complicated model of inflation, possibly with two or more interacting fields.

A sharp increase in the power on the scales $k = 0.001$ – 0.01 (s/km) (or 5 - 0.5 Mpc) at $z = 2$ is a potential solution. While such features are not expected from inflaton, they are possible, for example in the Broken Scale Invariance model. Reference [38] use the BSI model [83] to produce a sharp decrease in the primordial power on small-scales ($k > 4.5h$/Mpc or $k > 0.016$ s/km at $z = 2$) to help yield fewer minihalos or dwarf galaxies around our Galaxy.

Power spreads to other wavenumbers through non-linear mode coupling. A sharply defined feature at a limited range of k in the primordial power spectrum will spread to a wider range of k at lower z [99]. For the Lyα forest, these non-linear corrections drive the 3-D power spectrum to a $k^{-1.4}$ shape nearly independent of the initial conditions [101]. It is then unclear if we can obtain the increase in power at $z = 2$ and over $k = 0.001$ – 0.01 (s/km) (or 0.5 - 5 Mpc) without simultaneously also obtaining too much power on related scales where galaxy clustering data apply, and there is a need for reduced, not increased power.

Warm dark matter will steepen the power spectrum over a small range of

wavenumbers, improving the match with data. Let us explore the effects of WDM by first assuming that the simulations correctly predict P_{-2}. Figure 1 shows that we can match the observed P_{-2} using a low value for $\gamma_{912}\sim$ 0.6. A standard simulation with γ_{912}= 0.6 will give $P_{-1.5}$ and P_{-1} values that are too large, but if we change the simulation by replacing some or all of the CDM with WDM we might be able to reduce $P_{-1.5}$ and P_{-1} back to the data values. The WDM would also change the b_σ, and we might be able to adjust X_{228} to match the observed b_σ. However, this scenario is likely to fail to match the $\tau_{\rm eff}$. Since this WDM simulation would have a very low γ_{912}, and since it would have more flux power (on large-scales alone), we expect it gives more absorption than data. Since we use both γ_{912} and X_{228} to match other statistics, we have no remaining freedom to adjust the simulation to match the $\tau_{\rm eff}$.

A second problem with WDM is that the changes are largest at high redshifts and the limit of $m > 4$ keV for a WDM particle and $m > 28$ keV for sterile neutrinos that [91] find using Lyα forest spectra at $2.5 < z < 5.5$, especially near 5.5, are large enough that we will not see a noticeable effect at $z = 1.95$.

2.6 Consequences

If we are to extract quantitative information about the IGM or the primordial perturbations, we will have to closely match the Lyα forest data. This is because even simple equations for gas in an equilibrium with pressure balancing gravity, and photoionization, without any dark matter are sufficient to give the order of magnitude properties of the gas causing the Lyα forest absorption [74, 87, 75]. We can obtain simulated Lyα forest spectra that look qualitatively reasonable without knowing the details of the cosmological model, such as the primordial perturbations [57].

Standard simulations of the IGM do not match data on the Lyα forest. Provided the data are reliable, this mismatch implies that these simulations are

unrealistic. We then do not know the regions of the IGM that cause the Lyα absorption, and we cannot use these simulations to reliably extract information from the Lyα forest. We now discuss some of the wide reaching web of consequences, for the temperature of the absorbing IGM gas, its density, the correlation between the density and temperature and hence the volume of the IGM that contains heavy elements, the intensity of the ultraviolet background, the primordial power spectrum and the limits on the neutrino masses.

2.6.1 The temperature of the intergalactic medium

We obtain a new estimate of the temperature of the IGM of $T_o = 10,300$ K at $z = 1.95$ from a simulation that uses our standard input-parameter values (table 2.4). This is the most common (mode) temperature of cells at the mean baryon density, where we used [37, table 9] to relate T_o to box size and X_{228}. This simulation matches four statistics from data: the mean absorption ($\tau_{\rm eff}$), the power spectrum of the flux on intermediate and small-scales and the b_σ value. Following [88, Fig. 18], we expect that this simulation will also match the b-value distribution. Hence, this temperature estimate uses an amalgam of two methods, one using the lower-boundary of the b-values as a function of the column density [35, 43, 76], and the other the shape of the power spectrum on small-scales [100, 94, 54].

We likely know the approximate IGM temperature but not the precise distribution or mean value. The Lyα line widths depend on a combination of the temperature, (turbulent) bulk motions and Hubble flow (expansion) across the size of the absorbing regions [74, 66]. We can obtain an approximate lower limit to the IGM temperature from the narrowest Lyα lines, assuming the line width comes from the temperature, and ignoring bulk motions. These temperatures are in the (wide) range expected from heating during photoionization, followed by adiabatic cooling [60, 15], with harder spectra and more recent ionization leaving higher temperatures.

Simulations are required for precise temperature estimates, to associate temperature and density, and to include shock heating. The effects of shock heating are significant at densities as low as the mean gas density. We see this in [90, Fig. 24] where larger simulation boxes contain longer wavelength perturbations that give higher velocity shocks, more shocks of a given velocity and hotter gas at all densities.

There are signs that the standard simulations do not give good descriptions of the IGM temperatures. In an attempt to measure the matter power from the Lyα forest, [92] reported that their fit to SDSS spectra favored "either an implausibly large temperature or an implausibly steep temperature – density relation". A larger temperature in simulations will make the flux-power spectrum fall more steeply towards small-scales, which will improve the match with the shape of the flux-power in data. In [66, Fig. 8] an artificial increase of all temperatures by a factor of 2.4, and a simultaneous decrease in γ_{912} (to stop the $\tau_{\rm eff}$ decreasing) leaves P_{-2} unchanged while P_{-1} drops by a factor of 10.

The temperature estimates will also be in error if the size of the absorbing regions is inaccurate, or in general if the wrong regions of the simulation are making the Lyα forest absorption. Further, we know that the temperature distribution in these simulations is in error because they do not model the transfer of the ionizing radiation and the progress of the He^+ photoionization, when the gas temperature can increase by $\sim 5,000$ K [6].

2.6.2 The gas density and the temperature-density correlation

There are many ways to change the density of the gas in simulations that is causing the Lyα absorption. A change in the primordial power spectrum can obviously change the density distribution. A change in the thermal history will lead to a differing profile of pressure over time, and a change in the "filtering scale" [28]

and the size and density of the absorbing regions. A change in the temperature leads to a change in the neutral fraction and again a change in the gas density for a given column density. Reference [66] shows that the flux pdf is sensitive to the density of the regions that make the Lyα forest, hence the mismatch in that statistic [3, 7] suggests that the wrong parts of the IGM are making the Lyα forest in standard simulations.

The standard simulations produce a tight positive correlation between the typical temperature and the gas density [59, 71], with higher temperatures at higher densities because those regions expand less and cool less. This correlation has often been used to relate the observed column densities back to gas density, and ionization, for example in estimates of the temperature at a given density [76], and the fraction of the volume of the IGM that shows absorption lines from heavy elements that came from inside stars [2]. The He^+ photoionization alone will give a more complex distribution of temperature as a function of density [86, 6], and the failure of the standard simulations to match data means that the tight temperature – density correlation is a questionable assumption.

2.6.3 The intensity of the ultraviolet background that can ionize hydrogen

A simulation using our standard input-parameter values also gives a new estimate of Γ, the rate of ionization per neutral hydrogen atom that comes from the intensity of the UV background. At $z = 1.95$, a simulation using the standard values (table 2.2) requires γ_{912}= 1.34 times the intensity estimated by reference [50], or $\Gamma = 1.78 \times 10^{-12}$ (s^{-1}). Alternatively, if we estimate the σ_8 from the Lyα forest data, we find (figure 2.5) σ_8= 0.74, γ_{912}= 1.47 and $\Gamma = 1.95 \times 10^{-12}$ (s^{-1}). While these estimates may be more accurate than those in the literature that came from simulations that were even farther from matching the Lyα forest, we should regard all such estimates as suspect because none come from simulations

that match all the Lyα forest data.

An error in the temperature distribution (as a function of gas density) will propagate into an error in the intensity of the ionizing UV background. The neutral fraction depends on the balance between the photoionization and temperature dependent collisional ionization rates and the temperature dependent recombination rate. If the density distribution and the mean amount of absorption are unchanged, but the temperature distribution changes, then the intensity of the ionizing radiation must change in compensation. An error in the UV background intensity can also come directly from an error in the density of the absorbing gas, since the neutral hydrogen density $n_{HI} \propto n^2 T^{-0.7}$, where the first term is for the faster recombination at higher gas density n, and the second term accounts for the collisional ionization. In standard simulations, the hydrogen temperature $T \propto n^{0.6}$, but we now question this common assumption.

2.6.4 The matter power spectrum from the Lyα forest

We cannot use the Lyα forest data to make reliable estimates of the primordial matter power spectrum because these estimates need realistic simulations of the IGM that we do not have. The underlying idea that there is more Lyα absorption in places with higher gas and matter density is reasonable, but the detailed relationship between the matter power and the observed flux power relies upon simulations. Only recently have large hydrodynamic simulations been used and these do not match data. Earlier work used approximate simulations, idealized temperature – density relations and various nuisance parameters that in combination hid the mismatch.

Reference [19] were the first to estimate the matter power from a large sample of high resolution spectra. They used collisionless N-body simulations to measure the density field. They made artificial spectra by converting the gas density n to optical depth τ assuming $\tau \propto n_{HI} \propto n^2 T^{-0.7}$ and that the temperature

is a power law of the density, $T = T_0 n^{0.6}$ with $T_0 = 15,000$ (K). They multiply all optical depths by a constant to match the observed mean $\tau_{\rm eff}$. They then found the simulation that gave 3-D flux power most like data, and they converted the observed 3-D flux power (P_F) to matter power (P_m) using the bias $b(k) = P_F(k)/P_m(k)$ taken from that simulation.

Reference [92] summarizes some of the many ways in which various measurements of matter power from the Lyα forest could be in error. The SDSS spectra used by [56, 78] are of low resolution, and low signal-to-noise ratio. Hence, metal lines and high column density absorbers could not be identified and the continuum levels were poorly known. They explored a thirty-four parameter model using Hydro Particle Mesh simulations [30] with particles moving under gravity plus pseudo-pressure computed from an artificial temperature – density relation. They computed and applied a large number of complex and relatively large correction terms.

Reference [92] found that their fit to SDSS spectra alone (the same set of SDSS spectra that were used by [56, 78]) led to implausibly large temperatures or implausibly steep temperature – density relations. They felt that this most likely reflected a systematic uncertainty that is not understood, rather than a temperature error. We agree, since our figures 2.4 and 2.5 show that we cannot solve the mismatch using a higher temperature (from larger X_{228}) while we simultaneously adjust γ_{912} and σ_8 to keep the line widths and mean absorption constant.

Our results demonstrate how a fit to the power spectrum shape and amplitude favors an unrealistically hot IGM. When we extrapolate the trends in figure 6 to large X_{228} (we have many simulations with X_{228}= 3.3 and one with 5.4) the green, blue and purple bands that show the power look as if they would converge at $X_{228}\sim$ 8 . This is not an acceptable model because the Lyα lines would be unacceptably wide, and the $\tau_{\rm eff}$ in simulations matching the power would be unacceptably large (low γ_{912}). Published measurements of the matter-power from the flux-power did not consider the b-values, and this made it harder for them to see

that their high temperature solutions were unrealistic.

2.6.5 Limits on the masses of the light active neutrinos

We know from the oscillations of atmospheric neutrinos [26] that the sum of the masses of the three neutrinos is $\Sigma m_\nu > 0.05$ eV. If this sum is < 0.1 eV, then the mass hierarchy is normal [47, 1] with mass-eigenstates $m_1 < m_2 \ll m_3 \sim 0.05$ eV. Alternatively, if the sum of the masses is > 0.1 eV, a second possibility is the inverted hierarchy with $m_3 < m_1 \sim m_2$. The upper limit on the masses from laboratory measurements of the tritium beta decay is around 2.2 eV for the electron neutrino and hence 6.6 eV for the sum of the masses. The limit on the sum of the masses from cosmological measurements is < 0.66 eV from the WMAP 5-year CMB data plus data on baryon acoustic oscillations and supernovae [24, 45].

Reference [80] claim a lower limit of $\Sigma m_\nu < 0.17$ eV using the CMB data, baryon acoustic oscillations, and the Lyα absorption in 3300 low resolution QSO spectra from the Sloan Digital Sky Survey plus high-resolution spectra of 8 QSOs from HIRES on the Keck telescope. Reference [56] found that SDSS spectra prefer a high IGM temperature. This increases the ionization and reduces the amount of absorption and the flux power. To match the observed flux power, those simulations began with a higher amplitude of primordial power than is required by the CMB. We suggested in §2.4.3 that it is an accident that the Lyα forest spectra prefer a large σ_8 value. Instead, we suspect that the large σ_8, and the large temperature, are convenient degrees of freedom that compensate for some other problem with the data or simulations. The SDSS Lyα spectra are barely compatible with the CMB data without massive neutrinos, and adding massive neutrinos increases the tension between the two data sets. This tension was misinterpreted as an unusually low upper-limit on the neutrino masses.

Our simulations are typically larger and include a more accurate treatment of the gas physics than those used to derive the matter power spectrum and neu-

trino mass limits from the Lyα forest. We have also attempted to match the Lyα line widths that other groups typically ignored, and this helps us see that none of our simulations match Lyα forest data. We conclude that the upper-limits on the masses of neutrinos that have used Lyα forest spectra are unreliable.

2.6.6 Limits on the mass of sterile neutrinos as warm dark matter

Attempts have been made to use the growth of structure on small-scales in the Lyα forest from redshifts 5 to 2 to place constraints on the minimum mass for sterile neutrino dark matter [95, 96, 91, 79, 10]. There is a claim that sterile neutrinos are ruled out as the (only) dark matter particle [79], because the lower limits from Lyα forest power spectra overlaps the upper limits from the absence of X-rays from radiative decays. Here we agree with [11] that the list of issues with the Lyα forest power spectrum [10] make it too early to rule out WDM.

2.7 Conclusions

We reach the following conclusions.

1. We find that standard large fully-hydrodynamic, optically-thin simulations of the intergalactic medium do not match data on the Lyα forest at $z = 1.95$.

2. We can detect the mismatch using the power on large-scales ($k = 0.01$ s/km) together with one other statistic. When the second statistic is the power on intermediate ($\log k = -1.5$) or small-scales ($k = 0.1$), we see that the power in the simulations is a different shape from that in data. The simulation power rises too slowly as the scale increases. When the second statistic is the mean amount of absorption ($\tau_{\rm eff}$), we see that the simulations have too little large-scale power for the mean amount of absorption.

3. If there is a problem with data, the large-scale flux-power is the most likely suspect. However, different measurements of the power from Keck HIRES spectra, from VLT UVES spectra and from the SDSS all show more power than in the simulations (§2.5.1). In addition, there are also mismatches between simulations in two other statistics, the distribution of column densities of the Lyα absorption lines, and the number of pixels in a spectrum (of flux against wavelength) with a given amount of absorption. Simulated spectra have too few high column density Lyα lines and too few pixels where 75 – 95% of the flux is absorbed. The mismatch between the simulations and three statistics might have a common origin.

4. A change in the $\tau_{\rm eff}$ from QSO spectra will not remove the mismatch because we would need an unreasonably large 7σ increase that would create new mismatches with the intermediate and small-scale power (figure 2.4). Similarly, a change in the typical line width b_σ will not remove the mismatch.

5. Simulations that use X_{228}= 0.96, γ_{912}= 1.47, σ_8=0.74 (figure 2.5) in addition to the other standard input-parameter values from table 2.4 match four of the five output-statistics, all except the large-scale power P_{-2}. If we require a larger σ_8= 0.812 preferred by other data, the favored parameters change slightly to X_{228}= 1.04 and γ_{912}= 1.34 (figures 2.5, 2.7) and the match to the four statistics remains excellent.

6. Simulations with $\sigma_8 > 1$ come closer to matching the large-scale power, but not sufficiently close for this to be a preferred solution, and such large σ_8 values are disfavored by other data. Rather, we think it is an accident that large σ_8 values compensate for some other problem with the data or simulations.

7. We have a new estimate of the intensity of the ultraviolet background radiation that ionizes hydrogen in the intergalactic medium. A simulation that uses the standard input-parameter values (table 2.4) will best match four of

the five statistics (not the large-scale power) of the Lyα forest when it has γ_{912}= 1.3 times the intensity calculated by [50], or $\Gamma = 1.78 \times 10^{-12}$ (s^{-1}) ionizations per hydrogen atom. Figure 2.5 shows how these values decrease as σ_8 increases.

8. We have made a new estimate for the temperature of the IGM, from an amalgam of two methods that were used in the past, one using line widths and the other the power spectrum shape. We find that a simulation that uses the standard input-parameter values that matches four of the five statistics of the Lyα forest data have a most common temperature of 10,300 K at the mean baryon density.

9. A possible explanation for the mismatch is that standard simulations lack Lyα absorption lines with neutral hydrogen column densities $13.6 < \log N_{HI} < 16.9$ cm^{-2}. These lines can absorb $> 75\%$ of the flux in a pixel, improving the match to the flux distribution, and they will make more flux-power for a given amount of absorption, increasing the P_{-2}. A simulation will have more absorption at these column densities if its high density gas is less ionized, or cooler than in a standard simulation. To match the column density distribution and to leave the total absorption unchanged, lower density gas should make less absorption, because it is more ionized or hotter than in standard simulations.

10. We discussed two physical explanations. Our simulations are optically-thin and do not correctly model the transfer of radiation through the structures of the IGM. Hence they do not correctly distribute the heating that accompanies the He^+ ionization. If higher density regions ionize first, by $z = 1.95$ they will be relatively cooler and make more Lyα absorption than otherwise. A second class of explanation is that our simulations lack the resolution and radiation transfer required to correctly model the denser regions that cool and fragment to make many clumped absorption lines.

11. It is possible that the simulations do not match Lyα forest data because the IGM is not exclusively ionized and heated by ultraviolet photons from QSOs and stars. Alternatives include cosmic rays, or X-rays from early black holes or decaying particles.

12. There might be a problem with the cosmological model. A change in the primordial power spectrum seems unlikely since the Lyα forest needs more power on a very restricted range of wavenumbers at $z \sim 2$. Yet the relatively low numbers of dwarf galaxies in our halo [38] and the mass distribution near the core of galaxies [22] both argue for less power on similar small scales. A change in the primordial power that is restricted to a narrow range of wavenumbers will spread to a wider range of wavenumbers before $z \sim 2$.

13. Since we do not have simulations that match Lyα forest data, and we do not know why the standard simulations do not match data, we must question the wide web of results that have been obtained using such simulations. The temperature of the parts of the intergalactic medium that cause the Lyα absorption will be more uncertain than claimed. We no longer know the density of the gas causing the absorption. The tight correlation between the density and temperature that is seen in standard simulations is an uncertain assumption, and the flux of UV ionizing radiation that is required to make the observed Lyα absorption will also be inaccurate.

14. We question the accuracy of measurements of the matter power spectrum and the upper limits on neutrino masses that have come from Lyα forest data. Simulations are essential to such measurements and our simulations that do not match data are at least as reliable as those used to extract this information. Past measurements did not check to see if their simulations could match the Lyα line widths and hence it was harder for them to see that their simulations did not match data. In some cases they found solutions

that required temperatures that are far above those allowed by the Lyα line widths.

We thank Richard Ellis for information on the ionizing background. This work was supported by NSF grant AST-0808168. Simulations were produced using the facilities of the NCSA SDSC supercomputer centers with LRAC allocation MCA98N020.

This chapter is currently being prepared for submission for publication of the material. Day, Aaron; Tytler, David; Kirkman, David; Norman, Michael.

Bibliography

[1] F. B. Abdalla and S. Rawlings. Determining neutrino properties using future galaxy redshift surveys. *MNRAS*, 381:1313–1328, Nov. 2007.

[2] A. Aguirre, J. Schaye, L. Hernquist, S. Kay, V. Springel, and T. Theuns. Confronting Cosmological Simulations with Observations of Intergalactic Metals. *ApJ*, 620:L13, Feb. 2005.

[3] G. D. Becker, M. Rauch, and W. L. W. Sargent. The Evolution of Optical Depth in the Lyα Forest: Evidence Against Reionization at z˜6. *ApJ*, 662:72–93, June 2007.

[4] C. Boehm, A. Riazuelo, S. H. Hansen, and R. Schaeffer. Interacting dark matter disguised as warm dark matter. *Phys. Rev. DFIX*, 66(8):083505–+, Oct. 2002.

[5] J. S. Bolton and M. G. Haehnelt. The nature and evolution of the highly ionized near-zones in the absorption spectra of z ˜= 6 quasars. *MNRAS*, 374:493–514, Jan. 2007.

[6] J. S. Bolton, S. P. Oh, and S. R. Furlanetto. Photoheating and the fate of hard photons during the reionization of HeII by quasars. *MNRAS*, 395:736–752, May 2009.

[7] J. S. Bolton, M. Viel, T. . Kim, M. G. Haehnelt, and R. F. Carswell. Possible evidence for an inverted temperature-density relation in the intergalactic medium from the flux distribution of the Lyman-alpha forest. *ArXiv e-prints 0711.2064*, 711, Nov. 2007.

[8] S. Borgani and M. Viel. The evolution of a pre-heated intergalactic medium. *MNRAS*, 392:L26–L30, Jan. 2009.

[9] R. J. Bouwens, G. D. Illingworth, M. Franx, R. Chary, G. R. Meurer, C. J. Conselice, H. Ford, M. Giavalisco, and P. van Dokkum. UV Continuum Slope and Dust Obscuration from z˜6 to z˜2: The Star Formation Rate Density at High Redshift. *ArXiv e-prints*, Sept. 2009.

[10] A. Boyarsky, J. Lesgourgues, O. Ruchayskiy, and M. Viel. Lyman-α constraints on warm and on warm-plus-cold dark matter models. *Journal of Cosmology and Astro-Particle Physics*, 5:12–+, May 2009.

[11] A. Boyarsky, J. Lesgourgues, O. Ruchayskiy, and M. Viel. Realistic Sterile Neutrino Dark Matter with KeV Mass does not Contradict Cosmological Bounds. *Physical Review Letters*, 102(20):201304–+, May 2009.

[12] G. L. Bryan and M. L. Norman. Simulating X-Ray Clusters with Adaptive Mesh Refinement. In D. A. Clarke and M. J. West, editors, *Computational Astrophysics; 12th Kingston Meeting on Theoretical Astrophysics*, volume 123 of *Astronomical Society of the Pacific Conference Series*, page 363, 1997.

[13] G. L. Bryan, M. L. Norman, J. M. Stone, R. Cen, and J. P. Ostriker. A piecewise parabolic method for cosmological hydrodynamics. *Computer Physics Communications*, 89:149–168, Aug. 1995.

[14] W. Buchmüller, P. di Bari, and M. Plümacher. Leptogenesis for pedestrians. *Annals of Physics*, 315:305–351, Feb. 2005.

[15] R. Cen. The Universe Was Reionized Twice. *ApJ*, 591:12, July 2003.

[16] R. Cen, J. Miralda-Escude, J. P. Ostriker, and M. Rauch. Gravitational collapse of small-scale structure as the origin of the Lyman-alpha forest. *ApJ*, 437:L9–L12, Dec. 1994.

[17] R. Cen, K. Nagamine, and J. P. Ostriker. Quantitative Signatures of Galactic Superwinds on Lyα Clouds and Metal-Line Systems. *ApJ*, 635:86–99, Dec. 2005.

[18] R. A. C. Croft, L. Hernquist, V. Springel, M. Westover, and M. White. High-Redshift Galaxies and the Lyα Forest in a Cold Dark Matter Universe. *ApJ*, 580:634, Dec. 2002.

[19] R. A. C. Croft, D. H. Weinberg, M. Bolte, S. Burles, L. Hernquist, N. Katz, D. Kirkman, and D. Tytler. Toward a Precise Measurement of Matter Clustering: Lyα Forest Data at Redshifts 2-4. *ApJ*, 581:20, Dec. 2002.

[20] R. A. C. Croft, D. H. Weinberg, N. Katz, and L. Hernquist. Recovery of the Power Spectrum of Mass Fluctuations from Observations of the Ly alpha Forest. *ApJ*, 495:44, Mar. 1998.

[21] R. A. C. Croft, D. H. Weinberg, M. Pettini, L. Hernquist, and N. Katz. The Power Spectrum of Mass Fluctuations Measured from the LYalpha Forest at Redshift Z=2.5. *ApJ*, 520:1–23, July 1999.

[22] W. J. G. de Blok. The Core-Cusp Problem. *Advances in Astronomy*, 2010, 2010.

[23] S. Dodelson and E. Stewart. Scale dependent spectral index in slow roll inflation. *Phys. Rev. DFIX*, 65(10):101301–+, May 2002.

[24] J. Dunkley, E. Komatsu, M. R. Nolta, D. N. Spergel, D. Larson, G. Hinshaw, L. Page, C. L. Bennett, B. Gold, N. Jarosik, J. L. Weiland, M. Halpern, R. S. Hill, A. Kogut, M. Limon, S. S. Meyer, G. S. Tucker, E. Wollack, and E. L. Wright. Five-Year Wilkinson Microwave Anisotropy Probe Observations: Likelihoods and Parameters from the WMAP Data. *ApJS*, 180:306–329, Feb. 2009.

[25] R. Easther and H. V. Peiris. Implications of a running spectral index for slow roll inflation. *Journal of Cosmology and Astro-Particle Physics*, 9:10–+, Sept. 2006.

[26] Y. Fukuda, T. Hayakawa, E. Ichihara, K. Inoue, K. Ishihara, H. Ishino, Y. Itow, T. Kajita, J. Kameda, S. Kasuga, K. Kobayashi, Y. Kobayashi, Y. Koshio, M. Miura, M. Nakahata, S. Nakayama, A. Okada, K. Okumura, N. Sakurai, M. Shiozawa, Y. Suzuki, Y. Takeuchi, Y. Totsuka, S. Yamada, M. Earl, A. Habig, E. Kearns, M. D. Messier, K. Scholberg, J. L. Stone, L. R. Sulak, C. W. Walter, M. Goldhaber, T. Barszczxak, D. Casper, W. Gajewski, P. G. Halverson, J. Hsu, W. R. Kropp, L. R. Price, F. Reines, M. Smy, H. W. Sobel, M. R. Vagins, K. S. Ganezer, W. E. Keig, R. W. Ellsworth, S. Tasaka, J. W. Flanagan, A. Kibayashi, J. G. Learned, S. Matsuno, V. J. Stenger, D. Takemori, T. Ishii, J. Kanzaki, T. Kobayashi, S. Mine, K. Nakamura, K. Nishikawa, Y. Oyama, A. Sakai, M. Sakuda, O. Sasaki, S. Echigo, M. Kohama, A. T. Suzuki, T. J. Haines, E. Blaufuss, B. K. Kim, R. Sanford, R. Svoboda, M. L. Chen, Z. Conner, J. A. Goodman, G. W. Sullivan, J. Hill, C. K. Jung, K. Martens, C. Mauger, C. McGrew, E. Sharkey, B. Viren, C. Yanagisawa, W. Doki, K. Miyano, H. Okazawa, C. Saji, M. Takahata, Y. Nagashima, M. Takita, T. Yamaguchi, M. Yoshida, S. B. Kim, M. Etoh, K. Fujita, A. Hasegawa, T. Hasegawa, S. Hatakeyama, T. Iwamoto, M. Koga, T. Maruyama, H. Ogawa, J. Shirai, A. Suzuki, F. Tsushima, M. Koshiba, M. Nemoto, K. Nishijima, T. Futagami, Y. Hayato, Y. Kanaya, K. Kaneyuki, Y. Watanabe, D. Kielczewska, R. A. Doyle, J. S. George, A. L. Stachyra, L. L. Wai, R. J. Wilkes, and K. K. Young. Evidence for Oscillation of Atmospheric Neutrinos. *Physical Review Letters*, 81:1562–1567, Aug. 1998.

[27] S. R. Furlanetto and S. P. Oh. The History and Morphology of Helium Reionization. *ApJ*, 681:1–17, July 2008.

[28] N. Y. Gnedin. Probing the Universe with the Lyalpha forest - II. The column density distribution. *MNRAS*, 299:392, Sept. 1998.

[29] N. Y. Gnedin and A. J. S. Hamilton. Matter power spectrum from the Lyman-alpha forest: myth or reality? *MNRAS*, 334:107, July 2002.

[30] N. Y. Gnedin and L. Hui. Probing the Universe with the Lyalpha forest - I. Hydrodynamics of the low-density intergalactic medium. *MNRAS*, 296:44, May 1998.

[31] L. Hernquist, N. Katz, D. H. Weinberg, and M. Jordi. The Lyman-Alpha Forest in the Cold Dark Matter Model. *ApJ*, 457:L51, Feb. 1996.

[32] W. Hu, D. J. Eisenstein, and M. Tegmark. Weighing Neutrinos with Galaxy Surveys. *Physical Review Letters*, 80:5255–5258, June 1998.

[33] L. Hui. Recovery of the Shape of the Mass Power Spectrum from the Lyalpha Forest. *ApJ*, 516:519, May 1999.

[34] L. Hui, S. Burles, U. Seljak, R. E. Rutledge, E. Magnier, and D. Tytler. On Estimating the QSO Transmission Power Spectrum. *ApJ*, 552:15, May 2001.

[35] L. Hui and N. Y. Gnedin. Equation of state of the photoionized intergalactic medium. *MNRAS*, 292:27, Nov. 1997.

[36] L. Hui and R. E. Rutledge. The B Distribution and the Velocity Structure of Absorption Peaks in the Lyalpha Forest. *ApJ*, 517:541, June 1999.

[37] T. Jena, M. L. Norman, D. Tytler, D. Kirkman, N. Suzuki, A. Chapman, C. Melis, P. Paschos, B. O'Shea, G. So, D. Lubin, W. Lin, D. Reimers, E. Janknecht, and C. Fechner. A concordance model of the Lyman α forest at z= 1.95. *MNRAS*, 361:70–96, July 2005.

[38] M. Kamionkowski and A. R. Liddle. The Dearth of Halo Dwarf Galaxies: Is There Power on Short Scales? *Physical Review Letters*, 84:4525–4528, May 2000.

[39] T.-S. Kim, J. Bolton, M. Viel, M. G. Haehnelt, and R. F. Carswell. An improved measurement of the flux distribution of the Ly-alpha forest in QSO absorption spectra: the effect of continuum fitting, metal contamination and noise properties. *ArXiv e-prints 0711.1862*, 711, Nov. 2007.

[40] T.-S. Kim, S. Cristiani, and S. D'Odorico. The Lyalpha forest at $1.5 < z < 4$. *A&A*, 373:757, July 2001.

[41] T.-S. Kim, M. Viel, M. G. Haehnelt, B. Carswell, and S. Cristiani. Erratum: The power spectrum of the flux distribution in the Lyman α forest of a large sample of UVES QSO Absorption Spectra (LUQAS)*. *MNRAS*, 351:1471, July 2004.

[42] T.-S. Kim, M. Viel, M. G. Haehnelt, R. F. Carswell, and S. Cristiani. The power spectrum of the flux distribution in the Lyman α forest of a large sample of UVES QSO absorption spectra (LUQAS) (also erratum). *MNRAS*, 347:355, Jan. 2004.

[43] D. Kirkman and D. Tytler. Intrinsic Properties of the z $\sim$ 2.7 Lyman alpha Forest from Keck Spectra of Quasar HS 1946+7658. *ApJ*, 484:672, July 1997.

[44] K. Kohler and N. Y. Gnedin. Lyman Limit Systems in Cosmological Simulations. *ApJ*, 655:685–690, Feb. 2007.

[45] E. Komatsu, J. Dunkley, M. R. Nolta, C. L. Bennett, B. Gold, G. Hinshaw, N. Jarosik, D. Larson, M. Limon, L. Page, D. N. Spergel, M. Halpern, R. S. Hill, A. Kogut, S. S. Meyer, G. S. Tucker, J. L. Weiland, E. Wollack, and E. L. Wright. Five-Year Wilkinson Microwave Anisotropy Probe Observations: Cosmological Interpretation. *ApJS*, 180:330–376, Feb. 2009.

[46] M. Kowalski, D. Rubin, G. Aldering, R. J. Agostinho, A. Amadon, R. Amanullah, C. Balland, K. Barbary, G. Blanc, P. J. Challis, A. Conley, N. V. Connolly, R. Covarrubias, K. S. Dawson, S. E. Deustua, R. Ellis, S. Fabbro, V. Fadeyev, X. Fan, B. Farris, G. Folatelli, B. L. Frye, G. Garavini, E. L. Gates, L. Germany, G. Goldhaber, B. Goldman, A. Goobar, D. E. Groom, J. Haissinski, D. Hardin, I. Hook, S. Kent, A. G. Kim, R. A. Knop, C. Lidman, E. V. Linder, J. Mendez, J. Meyers, G. J. Miller, M. Moniez, A. M. Mourao, H. Newberg, S. Nobili, P. E. Nugent, R. Pain, O. Perdereau, S. Perlmutter, M. M. Phillips, V. Prasad, R. Quimby, N. Regnault, J. Rich, E. P. Rubenstein, P. Ruiz-Lapuente, F. D. Santos, B. E. Schaefer, R. A. Schommer, R. C. Smith, A. M. Soderberg, A. L. Spadafora, L.-G. Strolger, M. Strovink, N. B. Suntzeff, N. Suzuki, R. C. Thomas, N. A. Walton, L. Wang, W. M. Wood-Vasey, and J. L. Yun. Improved Cosmological Constraints from New, Old, and Combined Supernova Data Sets. , 686:749–778, Oct. 2008.

[47] J. Lesgourgues and S. Pastor. Massive neutrinos and cosmology. *Phys. Rep.*, 429:307–379, July 2006.

[48] A. Lidz, M. McQuinn, M. Zaldarriaga, L. Hernquist, and S. Dutta. Quasar Proximity Zones and Patchy Reionization. *astro-ph/0703667*, Mar. 2007.

[49] A. Loeb and J. S. B. Wyithe. Possibility of Precise Measurement of the Cosmological Power Spectrum with a Dedicated Survey of 21cm Emission after Reionizatio n. *Physical Review Letters*, 100(16):161301–+, Apr. 2008.

[50] P. Madau, F. Haardt, and M. J. Rees. Radiative transfer in a clumpy universe. III. the nature of cosmological ionizing sources. *ApJ*, 514:648–659, 1999.

[51] A. Maselli, S. Gallerani, A. Ferrara, and T. R. Choudhury. On the size of HII regions around high-redshift quasars. *MNRAS*, 376:L34–L38, Mar. 2007.

[52] P. McDonald. Toward a Measurement of the Cosmological Geometry at z ˜ 2: Predicting Lyα Forest Correlation in Three Dimensions and the Potential of Future Data Sets. *ApJ*, 585:34, Mar. 2003.

[53] P. McDonald, J. Miralda-Escudé, M. Rauch, W. L. W. Sargent, T. A. Barlow, R. Cen, and J. P. Ostriker. The Observed Probability Distribution Function, Power Spectrum, and Correlation Function of the Transmitted Flux in the Lyα Forest. *ApJ*, 543:1–23, Nov. 2000.

[54] P. McDonald, U. Seljak, S. Burles, , et al. The Lyα Forest Power Spectrum from the Sloan Digital Sky Survey. *ApJS*, 163:80–109, Mar. 2006.

[55] P. McDonald, U. Seljak, R. Cen, P. Bode, and J. P. Ostriker. Physical effects on the Lyα forest flux power spectrum: damping wings, ionizing radiation fluctuations and galactic winds. *MNRAS*, 360:1471–1482, July 2005.

[56] P. McDonald, U. Seljak, R. Cen, D. Shih, D. H. Weinberg, S. Burles, D. P. Schneider, D. J. Schlegel, N. A. Bahcall, J. W. Briggs, J. Brinkmann, M. Fukugita, Ž. Ivezić, S. Kent, and D. E. Vanden Berk. The Linear Theory Power Spectrum from the Lyα Forest in the Sloan Digital Sky Survey. *ApJ*, 635:761–783, Dec. 2005.

[57] A. Meiksin, G. Bryan, and M. Machacek. Hydrodynamical simulations of the Lyα forest: data comparisons. *MNRAS*, 327:296, Oct. 2001.

[58] A. A. Meiksin. The physics of the intergalactic medium. *Reviews of Modern Physics*, 81:1405–1469, Oct. 2009.

[59] J. Miralda-Escude, R. Cen, J. P. Ostriker, and M. Rauch. The Ly alpha Forest from Gravitational Collapse in the Cold Dark Matter + Lambda Model. *ApJ*, 471:582, Nov. 1996.

[60] J. Miralda-Escudé and M. Rees. Re-ionization and thermal evolution of a photo-ionized intergalactic medium. *MNRAS*, 266:343, 1994.

[61] M. L. Norman and G. L. Bryan. Cosmological Adaptive Mesh Refinement. In *ASSL Vol. 240: Numerical Astrophysics*, page 19, 1999.

[62] M. L. Norman, G. L. Bryan, R. Harkness, J. Bordner, D. Reynolds, B. O'Shea, and R. Wagner. Simulating Cosmological Evolution with Enzo. *ArXiv e-prints 0705.1556*, 705, May 2007.

[63] B. W. O'Shea, G. Bryan, J. Bordner, M. L. Norman, T. Abel, R. Harkness, and A. Kritsuk. Intoducing ENZO, an AMR cosmology application. In *Adaptive Mesh Refinement – Theory and Applications. Eds. T. Plewa, T. Linde & V.G. Weirs, Springer Lecture Notes in Computational Science and Engineering.* , 2004.

[64] B. W. O'Shea, K. Nagamine, V. Springel, L. Hernquist, and M. L. Norman. Comparing AMR and SPH Cosmological Simulations. I. Dark Matter and Adiabatic Simulations. *ApJS*, 160:1–27, Sept. 2005.

[65] P. Paschos, T. Jena, D. Tytler, D. Kirkman, and M. L. Norman. The Lyα forest at redshifts 0.1-1.6: good agreement between a large hydrodynamic simulation and HST spectra. *MNRAS*, 399:1934–1953, Nov. 2009.

[66] M. S. Peeples, D. H. Weinberg, R. Davé, M. A. Fardal, and N. Katz. Pressure Support vs. Thermal Broadening in the Lyman-alpha Forest I: Effects of the Equation of State on Longitudinal Structure. *ArXiv e-prints*, Oct. 2009.

[67] W. J. Percival, S. Cole, D. J. Eisenstein, R. C. Nichol, J. A. Peacock, A. C. Pope, and A. S. Szalay. Measuring the Baryon Acoustic Oscillation scale using the Sloan Digital Sky Survey and 2dF Galaxy Redshift Surv ey. *MNRAS*, 381:1053–1066, Nov. 2007.

[68] P. Petitjean, J. P. Mueket, and R. E. Kates. The LY alpha forest at low redshift: Tracing the dark matter filaments. *A&A*, 295:L9–L12, Mar. 1995.

[69] M. Rauch, J. Miralda-Escude, W. L. W. Sargent, T. A. Barlow, D. H. Weinberg, L. Hernquist, N. Katz, R. Cen, and J. P. Ostriker. The Opacity of the Ly alpha Forest and Implications for Omega B and the Ionizing Background. *ApJ*, 489:7, Nov. 1997.

[70] J. A. Regan, M. G. Haehnelt, and M. Viel. Numerical simulations of the Lyman α forest - a comparison of GADGET-2 and ENZO. *MNRAS*, 374:196–205, Jan. 2007.

[71] M. Ricotti, N. Y. Gnedin, and J. M. Shull. The Evolution of the Effective Equation of State of the Intergalactic Medium. *ApJ*, 534:41, May 2000.

[72] M. Ricotti and J. P. Ostriker. Reionization, chemical enrichment and seed black holes from the first stars: is Population III important? *MNRAS*, 350:539–551, May 2004.

[73] S. Samui and et al. Can Cosmic Rays Heat the Intergalactic Medium? In *International Cosmic Ray Conference*, volume 9 of *International Cosmic Ray Conference*, pages 215–+, 2005.

[74] W. Sargent, P. Young, A. Boksenberg, and D. Tytler. The Distribution of Lyman-Alpha Absorption Lines in the Spectra of six Quasars: Evidence for an Intergalactic Origin. *ApJS*, 42:41, 1980.

[75] J. Schaye. Model-independent Insights into the Nature of the Lyα Forest and the Distribution of Matter in the Universe. *ApJ*, 559:507–515, Oct. 2001.

[76] J. Schaye, T. Theuns, M. Rauch, G. Efstathiou, and W. L. W. Sargent. The thermal history of the intergalactic medium*. *MNRAS*, 318:817, Nov. 2000.

[77] D. W. Sciama. Decaying neutrinos and the opacity of the universe at the He II edge. *ApJL*, 426:L65+, May 1994.

[78] U. Seljak, A. Makarov, P. McDonald, and and others. Cosmological parameter analysis including SDSS Lyα forest and galaxy bias: Constraints on the primordial spectrum of fluctuations, neutrino mass, and dark energy. *PhysRevD*, 71(10):3515, May 2005.

[79] U. Seljak, A. Makarov, P. McDonald, and H. Trac. Can Sterile Neutrinos Be the Dark Matter? *Physical Review Letters*, 97(19):191303–+, Nov. 2006.

[80] U. Seljak, A. Slosar, and P. McDonald. Cosmological parameters from combining the Lyman-α forest with CMB, galaxy clustering and SN constraints. *Journal of Cosmology and Astro-Particle Physics*, 10:14–+, Oct. 2006.

[81] S. K. Sethi. Radiatively Decaying Neutrinos and Photoionization of the Universe at High Redshifts. *ApJ*, 474:13–+, Jan. 1997.

[82] D. P. Stark, A. J. Bunker, R. S. Ellis, L. P. Eyles, and M. Lacy. A New Measurement of the Stellar Mass Density at z˜5: Implications for the Sources of Cosmic Reionization. *ApJ*, 659:84–97, Apr. 2007.

[83] A. A. Starobinsky. Spectrum of adiabatic perturbations in the universe when there are singularities in the inflationary potential. *Soviet Journal of Experimental and Theoretical Physics Letters*, 55:489–494, May 1992.

[84] T. Theuns, A. Leonard, G. Efstathiou, F. Pearce, and P. Thomas. Dependencies of QSO Lyα absorption line statistics on cosmological parameters. *MNRAS*, 303:L58, 1998.

[85] T. Theuns, M. Viel, S. Kay, J. Schaye, R. F. Carswell, and P. Tzanavaris. Galactic Winds in the Intergalactic Medium. *ApJ*, 578:5, 2002.

[86] E. R. Tittley and A. Meiksin. Reionization scenarios and the temperature of the intergalactic medium. *MNRAS*, 380:1369–1386, Oct. 2007.

[87] D. Tytler. The distribution of QSO absorption system column densities - Evidence for a single population. *ApJ*, 321:49–68, Oct. 1987.

[88] D. Tytler, D. Kirkman, J. M. O'Meara, N. Suzuki, A. Orin, D. Lubin, P. Paschos, T. Jena, W. Lin, M. L. Norman, and A. Meiksin. Cosmological Parameters σ_8, the Baryon Density Ω_b, the Vacuum Energy Density Ω_Λ, the Hubble Constant and the UV Background Intensity from a Calibrated Measurement of H I Lyα Absorption at z=1.9. *ApJ*, 617:1, Dec. 2004.

[89] D. Tytler, J. M. O'Meara, N. Suzuki, D. Kirkman, D. Lubin, and A. Orin. The Kast Ground-based Ultraviolet Spectral Survey of 79 Quasi-stellar Objects at Redshift 2 for Lyα Forest and Metal Absorption. *AJ*, 128:1058, Sept. 2004.

[90] D. Tytler, P. Paschos, D. Kirkman, M. L. Norman, and T. Jena. The effect of large-scale power on simulated spectra of the Lyα forest. *MNRAS*, 393:723–758, Mar. 2009.

[91] M. Viel, G. D. Becker, J. S. Bolton, M. G. Haehnelt, M. Rauch, and W. L. W. Sargent. How Cold Is Cold Dark Matter? Small-Scales Constraints from the Flux Power Spectrum of the High-Redshift Lyman-α Forest. *Physical Review Letters*, 100(4):041304–+, Feb. 2008.

[92] M. Viel and M. G. Haehnelt. Cosmological and astrophysical parameters from the Sloan Digital Sky Survey flux power spectrum and hydrodynamical simulations of the Lyman α forest. *MNRAS*, 365:231–244, Jan. 2006.

[93] M. Viel, M. G. Haehnelt, R. F. Carswell, and T.-S. Kim. The effect of (strong) discrete absorption systems on the Lyman α forest flux power spectrum. *MNRAS*, 349:L33–L37, Apr. 2004.

[94] M. Viel, M. G. Haehnelt, and V. Springel. Inferring the dark matter power spectrum from the Lyman α forest in high-resolution QSO absorption spectra. *MNRAS*, 354:684–694, Nov. 2004.

[95] M. Viel, J. Lesgourgues, M. G. Haehnelt, S. Matarrese, and A. Riotto. Constraining warm dark matter candidates including sterile neutrinos and light gravitinos with WMAP and the Lyman-α forest. *Phys. Rev. D*, 71(6):063534–+, Mar. 2005.

[96] M. Viel, J. Lesgourgues, M. G. Haehnelt, S. Matarrese, and A. Riotto. Can Sterile Neutrinos Be Ruled Out as Warm Dark Matter Candidates? *Physical Review Letters*, 97(7):071301–+, Aug. 2006.

[97] M. Viel, S. Matarrese, T. Theuns, D. Munshi, and Y. Wang. Dark energy effects on the Lyman α forest. *MNRAS*, 340:L47, Apr. 2003.

[98] M. Volonteri and N. Y. Gnedin. Relative Role of Stars and Quasars in Cosmic Reionization. *ApJ*, 703:2113–2117, Oct. 2009.

[99] M. White and R. A. C. Croft. Suppressing Linear Power on Dwarf Galaxy Halo Scales. *ApJ*, 539:497–504, Aug. 2000.

[100] M. Zaldarriaga, L. Hui, and M. Tegmark. Constraints from the Lyα Forest Power Spectrum. *ApJ*, 557:519–526, Aug. 2001.

[101] M. Zaldarriaga, R. Scoccimarro, and L. Hui. Inferring the Linear Power Spectrum from the Lyα Forest. *ApJ*, 590:1, June 2003.

[102] Y. Zhang, P. Anninos, M. L. Norman, and A. Meiksin. Spectral Analysis of the Ly alpha Forest in a Cold Dark Matter Cosmology. *ApJ*, 485:496, Aug. 1997.

Chapter 3

Neutrino mass constraints loosened by a new, carefully calibrated measurement of the power spectrum of the Lyα forest from HIRES spectra

3.1 Abstract

We present the flux power spectrum of the Lyα forest from 91 HIRES QSO spectra. This is the largest high resolution sample to date, yielding the smallest statistical errors. We remove damped Lyα absorbers from the spectra through the use of Voigt profile fits, and we report the power spectrum both with and without these absorbers removed. We subtract metal lines statistically based on metal absorption on the red side of the Lyα emission peak. We find that when performing a statistical subtraction of metal lines, a systematic offset due to the blending of metal and hydrogen lines must be taken into account. This offset was

not accounted for in previous analyses, and requires up to a 3% reduction in the SDSS Lyα forest flux power spectrum, increasing the allowed neutrino mass. For the first time in a Lyα forest power spectrum measurement from high resolution spectra, we avoid the artificial amplification of the power on small scales caused by spectral leakage, by applying Welch's spectral window function. Our careful treatment of metal line removal as well as our elimination of errors due to spectral leakage leads to an accurate measurement of the Lyα forest power spectrum at the smallest scales. We find evidence that previously published values of the power are systematically too high at scales $logk \geq -1.3$, which implies a hotter IGM than previously interpreted from the Lyα forest flux power spectrum.

3.2 Introduction

The Lyα absorption lines found in the spectra of high redshift quasars that make up the Lyα forest provide a probe of the neutral hydrogen distribution along the line of sight to the quasar. Observational data interpreted through theoretical models including hydrodynamic computer simulations have led to the understanding that the neutral hydrogen which gives rise to the Lyα forest maps the underlying dark matter distribution in a straight forward way [3, 23, 10, 30]. By the redshifts relevant to the Lyα forest, hydrogen in the intergalactic medium (IGM) is highly ionized by a nearly uniform ionizing background radiation. Photoionizations are balanced by the temperature dependent radiative recombination rate, leading to a neutral hydrogen distribution that is dependent on the total matter density as well as the temperature. Cosmological expansion cools the gas in much of the IGM, while photoionizations cause heating. The dependence of the heating and cooling processes on the density gives rise to a strong relationship between temperature and density. The thermal history sets the pressure profile and leads to a filtering scale at which gravitational collapse is inhibited. Thus at large scales, the neutral hydrogen maps the dark matter distribution, while at the

smallest scales, the temperature and ionization history of the IGM are imprinted.

The power spectrum of Lyα forest spectra provides information about the cosmological matter power spectrum at small scales, where because of their high redshift, the density fluctuations are only mildly nonlinear [6, 7, 9, 12, 20, 32, 5, 22]. The Lyα forest power spectrum also contains information about the temperature, which leads to doppler broadening of the absorption lines and sets the shape and amplitude of the power at the smallest scales present in the Lyα forest [11, 31, 26, 19, 37, 14]. Information about the temperature allows a more accurate model of the IGM to be made, from which the matter power spectrum can be extracted. When combined with large scale probes, such as the CMB, the Lyα forest offers constraints on the shape of the matter power spectrum, including the spectral index and the running of the spectral index [29, 17, 8]. The Lyα forest can also be used to place constraints on the masses of active neutrinos and WDM particles [27, 28, 34, 35, 33, 4, 1, 2]. These light particles leave a characteristic suppression of the matter power spectrum at a scale determined by their masses due to the free-streaming out of gravitational potential wells.

While large numbers of Lyα forest spectra continue to be obtained by the Baryon Oscillation Spectroscopic Survey (BOSS), these spectra are limited in the smallest scales they can probe by the resolution of the instrument. HIRES spectra on the other hand fully resolve the HI absorption lines of the Lyα forest allowing the analysis to push down to the smallest scales allowed by the IGM and absorption line physics.

We present the flux power spectrum of 91 QSO spectra collected with the HIRES spectrograph on the KECK telescope. The outline of this paper is as follows. The data sample is described in §3.3. The technical details of our power spectrum calculation, including how we avoid spectral leakage, subtract noise, and deal with gaps in the spectra is discussed in §3.4. We present our results, including the power removed for metal absorption and damped Lyα (DLA) systems, as well as the Lyα forest power spectrum excluding these absorbers. We discuss our

conclusions in §3.6.

3.3 Data Sample

3.3.1 Sample description

Our data set consists of 91 high resolution QSO spectra observed using the Keck telescope with the HIRES spectrograph and reduced with the standard MAKEE (MAuna Kea Echelle Extraction) reduction software. This number is about a factor of 3 greater than any previously published high resolution data set used to measure the Lyα forest flux power spectrum. The larger size of our data set reduces cosmic variance, which is still the dominant source of error in the measurement of the power spectrum at the smallest scales. The resolution is 8 km/s FWHM with the spectra rebinned into 2.1 km/s pixels. This resolution is sufficient to fully resolve HI lines, thus allowing a measurement of the power spectrum at the smallest possible scales. The Lyα forest data is taken at rest wavelengths 1070 Å$\leq \lambda \leq$ 1190 Å, with the lower wavelength chosen to avoid prominent emission lines, and the higher wavelength chosen to avoid the proximity effect near the quasar. We obtained our data set from the Keck Archive, and 30 of our spectra are the same as those used in the power spectrum measurement presented by [5]. A complete list of the QSOs is given in Table 3.3. We divide our results into redshift bins of width $\Delta z = 0.4$, with the exception of our highest redshift bin, which contains all data with $z > 3.8$ with a width of $\Delta z = 0.78$. Table 3.1 provides basic statistics for each redshift bin for our Lyα forest data. All spectra have S/N greater than 10. For statistics on metal absorption, we use the rest wavelength range 1268 Å$\leq \lambda \leq$ 1380 Å. Table 3.2 provides basic statistics for each redshift bin for our metal data.

Table 3.1: Basic Lyα forest statistics for each z-bin of our data sample. The Lyα forest data is taken at rest wavelengths 1070 Å$\leq \lambda \leq$ 1190 Å.

$\bar{z}$	z range	Δz	# spectra	S/N
2.01	1.8-2.2	4.13	23	30.3
2.40	2.2-2.6	5.33	30	36.2
2.82	2.6-3.0	8.00	34	35.5
3.14	3.0-3.4	3.84	18	31.2
3.60	3.4-3.8	0.811	3	30.2
4.21	3.8-4.58	1.63	4	35.5

Table 3.2: Basic metal statistics for each z-bin of our data sample. The metal data is taken at rest wavelengths 1268 Å$\leq \lambda \leq$ 1380 Å.

$\bar{z}$	z range	Δz	# spectra	S/N
2.12	1.8-2.2	1.49	10	21.4
2.36	2.2-2.6	3.21	19	23.8
2.83	2.6-3.0	2.64	15	28.9
3.21	3.0-3.4	2.81	16	27.8
3.57	3.4-3.8	4.01	16	25.5
4.11	3.8-4.65	1.14	5	26.2

Table 3.3: QSO coordinates and redshifts

Coordinates	z_{em}	Coordinates	z_{em}
Q0005+0524	1.89	Q0528-2505	2.77
Q0747+4259	1.90	Q0055+0059	2.77
Q0747+4259	1.90	Q1343+2847	2.84
Q1517+2356	1.90	Q0119+1432	2.87
Q0122-0421	1.93	Q0805+0441	2.88
Q0848+1623	1.93	Q2038-0116	2.90
Q0935+4141	1.94	Q1406+6508	2.95
Q0100+0211	1.95	Q1107+4847	2.96
Q0058+0155	1.96	Q1946+7658	2.99
Q0757+3551	1.98	Q1437+3007	3.00
Q0421+0157	2.04	Q0130-4021	3.02
Q1202+5937	2.05	Q1946+7658	3.05
Q0348+0610	2.05	Q0324-4047	3.06
Q2337-0110	2.09	Q0940-1050	3.09
Q1307+4617	2.13	Q1222+4847	3.09
Q0424-1309	2.17	Q0449-1325	3.09
Q1225+3145	2.20	Q1017+1055	3.11
Q1103+6416	2.20	Q0746+4200	3.12
Q1106+6400	2.20	Q1011+4315	3.13
Q1520+5213	2.21	Q1005+3638	3.13

Table 3.3 – continued from previous page

Coordinates	z_{em}	Coordinates	z_{em}
Q0237-2322	2.22	Q2100-0641	3.14
Q2120-0103	2.26	Q0636+6801	3.17
Q1417+5936	2.30	Q0636+6801	3.18
Q0450-1310	2.30	Q0336-0143	3.20
Q1626+6433	2.32	Q0741+4741	3.21
Q0153+7428	2.34	Q0347-3819	3.22
Q2048+1938	2.36	Q0757+5218	3.24
Q1122-1648	2.40	Q0302-0019	3.29
Q1122-1648	2.40	Q0956+1217	3.30
Q1337+2832	2.52	Q0857+4227	3.30
Q1347-2457	2.53	Q0322-3213	3.30
Q1015-2031	2.55	Q0014+8118	3.37
Q1243+3047	2.56	Q1623+3804	3.38
Q0953+5454	2.59	Q0926+2838	3.40
Q1310+4308	2.60	Q1732+5402	3.43
Q1623+2651B	2.60	Q0043-2633	3.44
Q1009+2956	2.62	Q1020+5158	3.45
Q0818+3117	2.62	Q2300-0955	3.45
Q0105+1619	2.64	Q1153+0547	3.46
Q1442+2931	2.67	Q1500+0431	3.66
Q0449-1645	2.68	Q1645+5520	4.04
Q0100+1300	2.68	Q1055+4611	4.14
Q1217+4957	2.70	Q0131+3252	4.53
Q1337+2123	2.70	Q1202-0725	4.70
Q0809+3217	2.71	Q0008+1429	4.97
Q1700+6416	2.74		

3.4 Technical details

3.4.1 Power spectrum definition

We use the standard definition of the flux power spectrum, in which the power spectrum is taken of the flux overdensity, which is defined to be:

$$\delta_f \equiv \frac{f - \bar{f}}{\bar{f}}, \tag{3.1}$$

where f is the flux in units of the continuum level, and $\bar{f}$ is the mean flux of an individual spectrum. The flux power spectrum is then given by:

$$P_F(k) = \delta_f(k)^* \delta_f(k), \tag{3.2}$$

where $\delta_f(k)$ is the Fourier Transform of the flux overdensity.

We focus on the measurement of P_F at wavenumbers $-2.5 \leq logk \leq -1.0$. As has been done in prior measurements of P_F from high resolution QSO spectra [20, 5, 15], we use the Lomb-Scargle Periodogram [18, 25, 24] to compute P_F, which is effectively a least-squares fit to sinusoids. This method can handle the gaps that are present in our data due to discontinuous echelle order joins and removal of high column density absorbers.

3.4.2 Effects of continuum fitting

For each QSO spectrum, we fit a continuum level which represents the flux that would be observed in the absence of absorption by HI and metals along the line of sight. The continua are used to normalize the spectra, so as to disregard QSO physics we are not interested in, allowing us to look at absorption line physics on a flux scale that ranges from 0 (fully absorbed) to 1 (no absorption). We work with the normalized flux throughout this paper.

Since we divide by the mean flux in the definition of P_F, it is insensitive to systematic offsets in the continuum fits to the Lyα forest spectra. However, any deviation from the true shape of the quasar continuum can lead to errors in the flux power spectrum. First, there is the possibility that the accuracy of the continuum fit is dependent on the level of absorption, since it can be difficult to determine the true continuum level in regions with large amounts of absorption.

Second, imperfections in the blaze function corrections may give rise to distortions in the power spectrum, particularly on scales around an echelle order. Third, the accuracy of the continuum fit of a quasar spectrum is dependent on the signal to noise.

To determine the size of the continuum fitting error caused by the finite S/N, we created 6 artificial spectra with S/N 5-20. These artificial spectra are different than the simple spectra discussed in §3.4.5. Since our continuum fitting is a manual process, it is important that these artificial spectra mimic the real spectra in every important way. We created these spectra using the technique discussed in [16], which includes emission lines, cosmic ray hits, echelle blaze and flux calibration errors.

We then fitted continua to them as if they were actual HIRES spectra. Figure 3.1 shows the change in P_F when using the fitted continuum compared to using the actual continuum. For S/N 10 and above, the change in P_F is less than 2% over the wavenumber range we report. Some of this small distortion is random in nature, so when averaging over several spectra, the size of the error will only decrease further. This test also demonstrates our ability to fit the continuum in regions with absorption, since any deviation would also be displayed in Figure 3.1.

It has been commented [15] that the shape of the continuum fit could be questionable around an echelle order, and that this could lead to a distortion in the power spectrum at small wavenumbers. To avoid this issue, we do not calculate the power at wavenumbers smaller than $logk = 2.5$. This scale is much smaller than the echelle order size, and so any oscillations in the continuum due to the echelle order will not influence our power measurement. We tested that for a subset of 30 spectra, when 2 different people fit the continua, the calculated power spectrum varied by less than 1%. We don't lose much from dropping wavenumbers less than

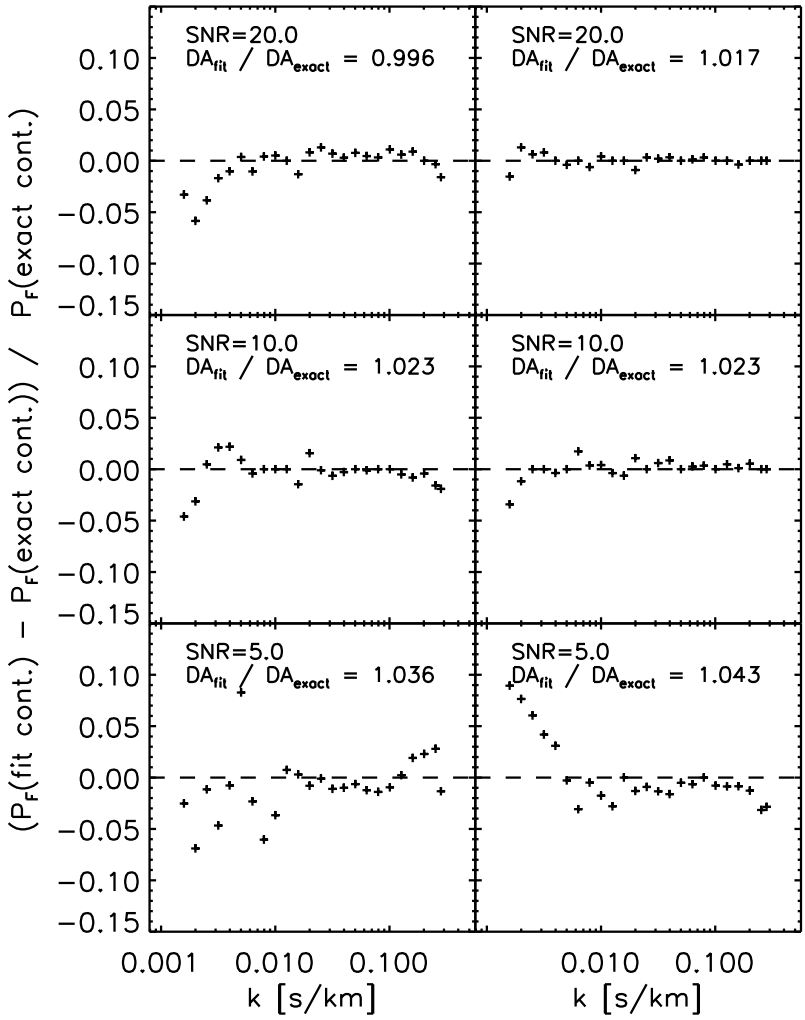

Figure 3.1: Continuum fitting to artificial QSO spectra at $z_{em} = 2.85$. Each plot shows the difference in P_F when calculated with a continuum fitted by hand, or with the actual known continuum. At S/N 10.0 and above, the continuum fit has almost no measurable effect on P_F for the wavenumbers of interest, $-2.5 <= logk <= -1.0$. Scatter at small k is mostly due to the small number of values in a bin.

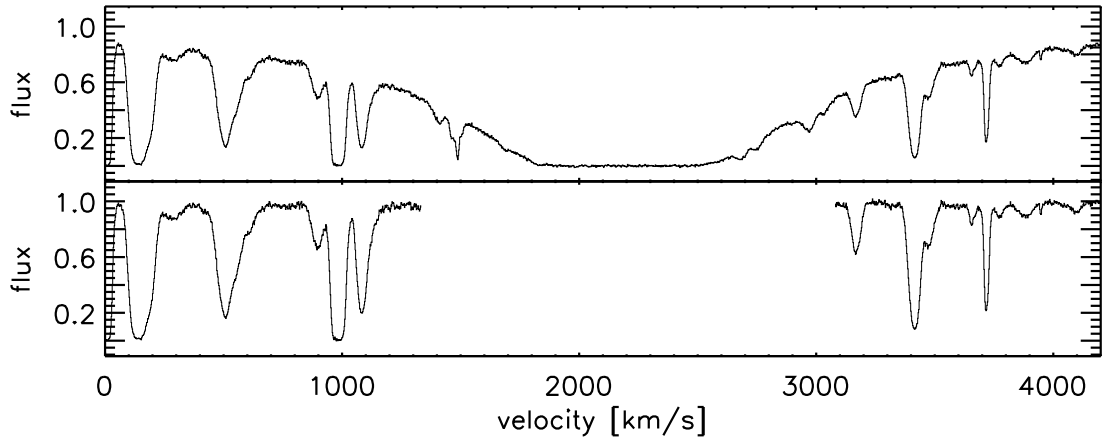

Figure 3.2: DLA line subtraction from a region of one of our HIRES spectra. The spectrum in the top panel is the unmodified raw flux. In the bottom spectrum, we removed the DLA line.

$logk = 2.5$, since smaller wavenumbers contain fewer modes per bin, and would have large error bars. Also, the power spectrum from the SDSS does not have this issue since it did not use an echelle spectrograph, and so it should be reliable at small wavenumbers [21]. Our data set augments the SDSS data set, which is not capable of measuring the small scales we measure here with HIRES spectra.

3.4.3 Damped Lyα line fitting and subtraction

We perform Voigt profile fits to all DLA absorbers in our spectra. We use these fits to separate the contribution to the power spectrum from DLA systems and other Lyα absorbers. We define DLA lines as those with $N(HI) \geq 10^{19} cm^{-2}$. The removal of these lines facilitates the comparison to simulations, which generally do not resolve these high density regions. We cut out regions with absorption greater than 50%, and divide the flux by the fits otherwise. Dividing by the absorption line flux is equivalent to subtracting the optical depth. Figure 3.2 shows an example of the subtraction of a DLA absorber from a region of one of

our spectra.

3.4.4 Metal line subtraction

We subtract metals statistically using a modification of the technique used for the SDSS Lyα forest flux power spectrum [21]. As was done by the SDSS group, we treat the metals on the red side of the Lyα emission peak as representative of the metals that are present in the Lyα forest at lower redshift. We follow their choice of using the rest wavelength range 1268 Å$\leq \lambda \leq$ 1380 Å.

Since we are using high resolution spectra which resolve individual absorption lines, and our spectra have high SNR, we have the ability to measure the effect of the blending of the HI lines with the metal lines. Simply subtracting the metal signal from the red side of the Lyα emission peak would not be strictly accurate, particularly since it is the optical depth of the absorbers that is additive, and not the signal which is the decrement in flux.

To measure this blending effect, we artificially take the pure metal signal on the red side of the Lyα emission peak, and add its optical depth to the Lyα forest creating a new spectrum that contains additional metals. If there were no effect from the blending process, we would expect that the power of the new spectrum would be equal to the sum of the power of the metals alone and the power of the original Lyα forest spectrum alone. We find that the combined spectrum has systematically more power than would be estimated by the assumption that the power is additive.

For each redshift bin, we create artificial spectra as described above for each pair of Lyα forest spectrum and metal spectrum. Given that absorption lines sometimes overlap, and sometimes don't, this introduces both a systematic and statistical error. For our calculation of the Lyα forest power spectrum with metal

lines subtracted, we take the power of the Lyα forest and subtract the metals found on the red side of the Lyα emission peak corrected for the blending effect.

Our metal subtraction method is superior to all previous methods. Compared to the most widely used data set from SDSS [21], we account for both the systematic and statistical error which had previously been neglected. While this error is small, it could lead to up to a 3% reduction in the power reported at the smallest scales, possibly loosening neutrino mass constraints which require a high degree of precision.

Previously published data from high resolution spectra have either ignored the metal contribution altogether [5, 15] or subtracted the metals by cutting out regions of the spectrum [20]. The gaps in the spectra that are introduced by cutting out the metals are known to distort the power spectrum calculation, particularly at the smallest scales [20].

3.4.5 Artificial spectra

To test our methodology, we utilize large numbers of artificial Lyα forest spectra. These spectra are generated from an ENZO simulation using the algorithm described in [14] and initially developed in [38]. The artificial spectra have the same velocity resolution as our HIRES spectra, and are roughly the same length (20000 pixels at 2.1 km/s per pixel). We do not expect that these spectra are equivalent to real HIRES spectra. Instead, we use them to show how well our power spectrum calculation technique deals with issues such as short spectrum segments, gaps in the spectra, and noise subtraction.

3.4.6 Spectral windows

Because some of our spectra start inside the Lyα forest and because we bin our data by S/N and redshift, we need to average P_F over spectrum segments of varying length. We find that P_F is amplified at our largest wavenumbers when using segments of length smaller than around a quarter of a spectrum. This amplification is due to spectral leakage, caused by the finite length of the spectrum segments. The finite length acts as a rectangular window function, for which the leakage falls off slower than P_F drops with increasing wavenumber. To solve this problem, we apply the Welch Window function [36] to the data before calculating P_F. This amounts to multiplying each pixel in the spectrum by the Welch Window function, defined by:

$$W(i) = 1 - [(i - (N-1)/2)/((N+1)/2)]^2 \tag{3.3}$$

where i is the pixel number, and N is the number of pixels in a segment. Use of the Welch Window function causes a loss of information at the edges of the spectrum, which can in part be circumvented by using Welch's Method [36], where each spectrum is cut into smaller overlapping segments. The smaller segments overlap by 50%, with each subsequent segment starting at the midpoint of the prior segment. The application of Welch's method combined with the Welch Window function results in data loss of about 1/3 of the size of the segment size we choose, due to the tapering of the spectrum segment at the edges. The Welch Window function is imperfect however, as it causes a systematic increase in power at small wavenumbers, where the shape of the window function is imprinted. Thus we must make a tradeoff between the distortion of the power at small wavenumbers if using small segments, and the loss of data if using long segments.

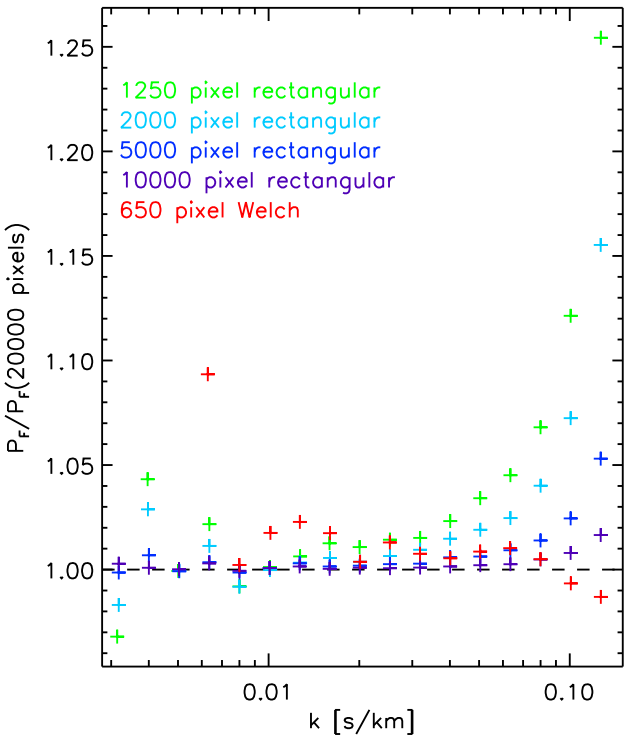

Figure 3.3: Distortion of the power spectrum of 3025 artificial Lyα forest spectra due to the data window function. The average of P_F is calculated with the specified window applied to the spectra, and the result is divided by the average of P_F calculated using the entire 20000 pixel spectrum. The rectangular windows cut the spectra into segments of equal length. The red points show the effect of multiplying the Lyα forest flux by the Welch window function before taking the power spectrum.

Figure 3.3 shows the distortion of P_F due to the windowing effects. For this plot, we used 3025 artificial spectra, which are only used to show relative effects due to the choice of window function. The rectangular windows show the effect of cutting the spectrum into segments of the specified length and then taking the power spectrum of the segments. For segments shorter than about a quarter of a spectrum, there is an amplification of the power by several percent at the largest wavenumbers. When using a Welch Window of length 650 pixels, the systematic error is eliminated at the highest wavenumbers. Since spectral leakage when using a rectangular window function is only significant at large wavenumbers, we choose to use a rectangular window function for $logk >= -1.5$, and the Welch Window function for $logk < -1.5$. We choose a rectangular window function of size 2000 pixels, and a Welch Window size of 650 pixels. This method is a major improvement over all past analyses of high resolution spectra, none of which used a smoothing window.

3.4.7 Gaps in the spectra

Although the Lomb-Scargle Periodogram algorithm can be used to calculate the power spectrum of a data set with gaps present, the gaps do cause some distortion. To measure this effect, we used our simulated ENZO Lyα forest spectra. For each of our actual HIRES QSO spectra with $S/N >= 10$, we created 50 artificial spectra with exactly the same length and with gaps that are the same size and in the same positions. We then calculated the power of these artificial spectra, both with and without the gaps. Since the positions of hydrogen absorbers relative to the position of the gaps is random, this demonstrates the severity of any deficiencies in the Lomb-Scargle Periodogram algorithm in dealing with the gaps. While this problem causes a systematic offset in the power spectrum measurement,

it is difficult to remove, because the size of the offset is dependent on the actual power present in an individual spectrum. Here we attempt only to show that the size of the offset is small in spectra with similar properties to our real HIRES spectra.

Figure 3.4 shows the size of this offset in the simulated spectra. Note that for this figure, we turned on all sources of gaps, including the removal of DLA absorbers. For removal of high column density HI absorbers, we have no choice but to cut out regions with absorption greater than 50%, since replacing the region with the continuum flux would bias our results. For the highest wavenumbers, it is crucial that the metal lines do not produce gaps in the data, as can be seen in Figure 3.5, where we cut the metal lines out by introducing a gap in the spectrum up to the point where the metal line absorption is less than 2%. Our method is therefore a major improvement over past analyses, which used the Lomb Periodogram algorithm and removed metals lines by introducing gaps in the spectra [20], or did not attempt to remove metal lines at all [15, 5, 7].

3.4.8 Noise correction

We estimate the effect of the noise on the power spectrum by calculating P_F of noise spectra. For each HIRES spectrum, we generate 200 noise spectra with each pixel in a noise spectrum generated from a gaussian random number corresponding to the S/N of the pixel as calculated during the data reduction process. We calculate P_F for each noise spectrum, calculate the mean, and then subtract this power from P_F of the Lyα forest. This gives a similar result as the rough estimate of the pixel noise contribution used by [15] in their calculation of P_F, originally given by [13] of $2(\delta v/\bar{f})(S/N)^{-2}$, where δv is the pixel size, $\bar{f}$ is the mean flux, and S/N is the signal-to-noise ratio. Our S/N is very high compared to

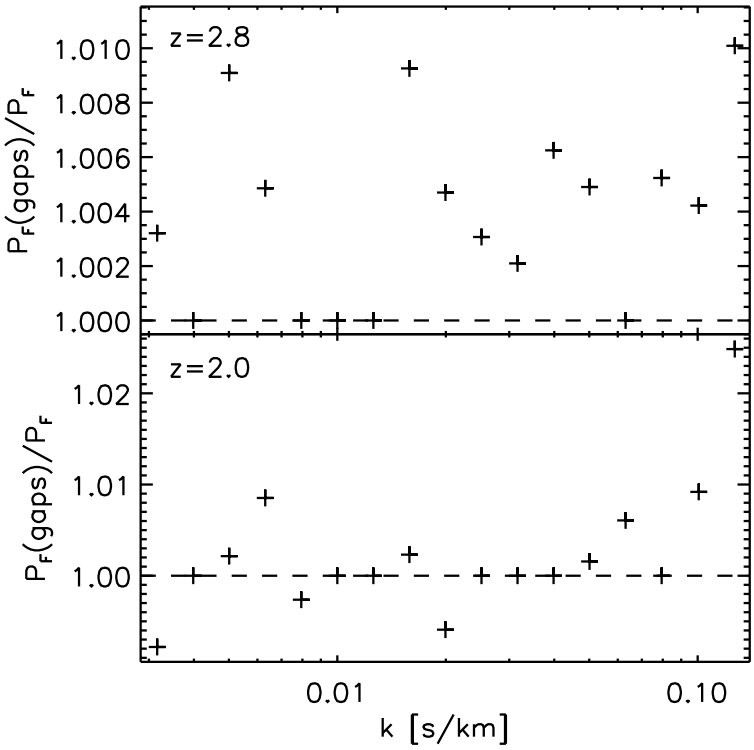

Figure 3.4: Distortion of the power spectrum of 1400 artificial Lyα forest spectra due to the presence of gaps in the spectra. Gaps are caused by discontinuous echelle order joins as well as removal of DLA absorbers. Note that our technique for removing metal lines does not introduce gaps.

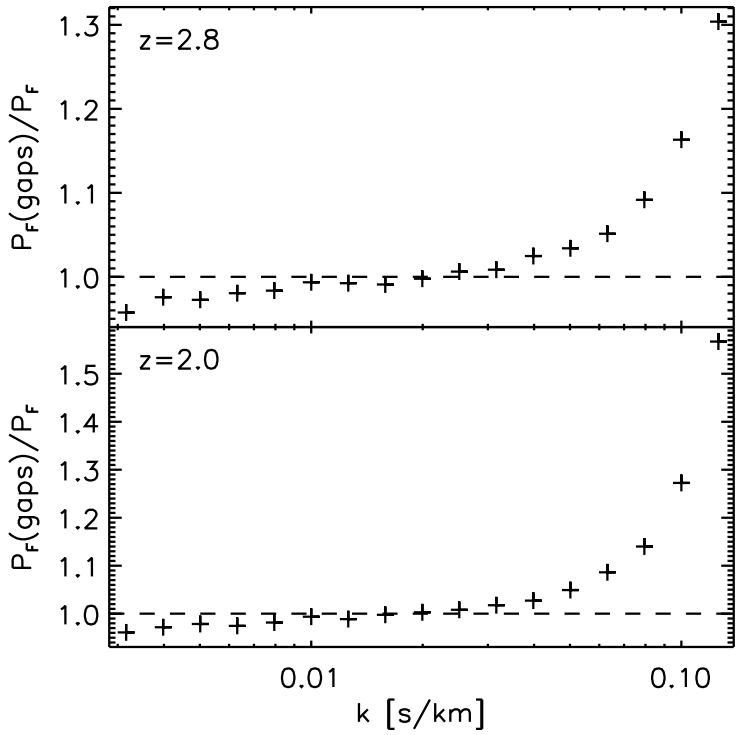

Figure 3.5: As Figure 3.4, but with segments of the spectra removed for metal lines. Our metal removal method avoids this large systematic offset.

the widely used SDSS P_F measurement [21], where in many cases the noise power was higher than the signal being measured. To ensure that our estimate of the noise power has little effect on our final answer, we explicitly exclude wavenumbers that have an estimated noise power greater than 10% of the mean P_F. Since P_F drops sharply at high wavenumbers, while the noise power remains roughly flat, we only drop a few of the highest wavenumbers in our lowest S/N spectra.

3.5 Results

3.5.1 Metal contribution

Figure 3.6 shows the relative contribution to the power spectrum by metal absorption. The metal contribution is calculated as the power of the Lyα forest minus the power of the Lyα forest with metal absorption removed. The dominant effect of removing metal absorption lines from the spectra is the reduction of the amplitude at wavenumbers corresponding to the velocity width of the absorption lines. A secondary, but still significant effect, is the reduction of the amplitude of the Lyα forest power spectrum due to the removal of the clustering of metal lines with each other, as well as with Lyα lines. The metal line contribution increases with increasing wavenumber, because the narrow line widths of the metals corresponds to the higher end of our wavenumber range. Metal lines cause a non-negligible increase in the power at all wavenumbers for redshifts less than about 3.2. For our two highest redshift bins, the metal contribution is low in part because the Lyα forest power spectrum amplitude is much higher due to the higher neutral fraction of hydrogen at higher redshift.

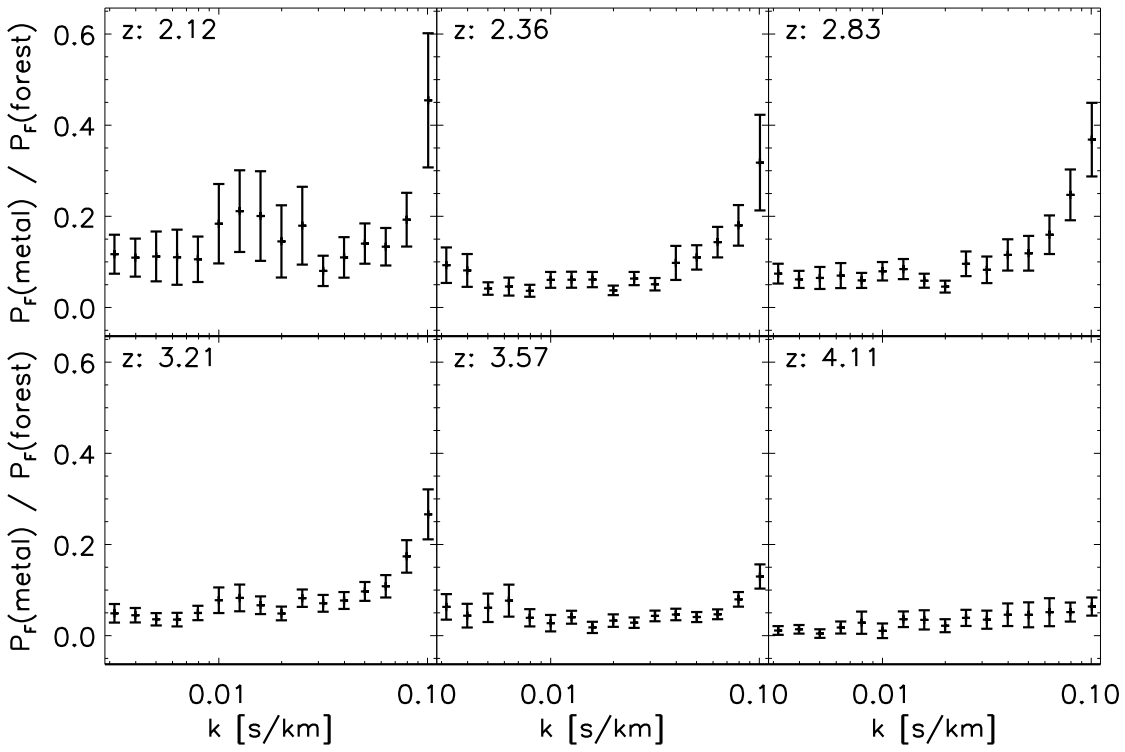

Figure 3.6: Power removed by metal subtraction divided by power of the Lyα forest with metals. The power removed by metal subtraction is calculated as the power of the forest minus the power of the forest with metals removed. Error bars are the bootstrap errors of this definition of the power removed by metal subtraction, divided by the Lyα forest power.

3.5.2 High column density line contribution

The presence of DLAs in Lyα forest spectra is problematic for two reasons. First, since they are relatively rare, in small sample sizes their effect will be dominated by shot noise. Second, modern computer simulations of the IGM, which are a necessary tool in interpreting Lyα forest flux statistics, do not yet produce the right distribution of the high density regions that produce DLAs.

Despite occupying a small fraction of the volume of the IGM, DLAs can have a large effect on the total absorption in a spectrum due to their long damping wings, and as such they cannot be ignored. We remove DLA lines from our spectra by cutting out regions where absorption is greater than 50% and otherwise dividing

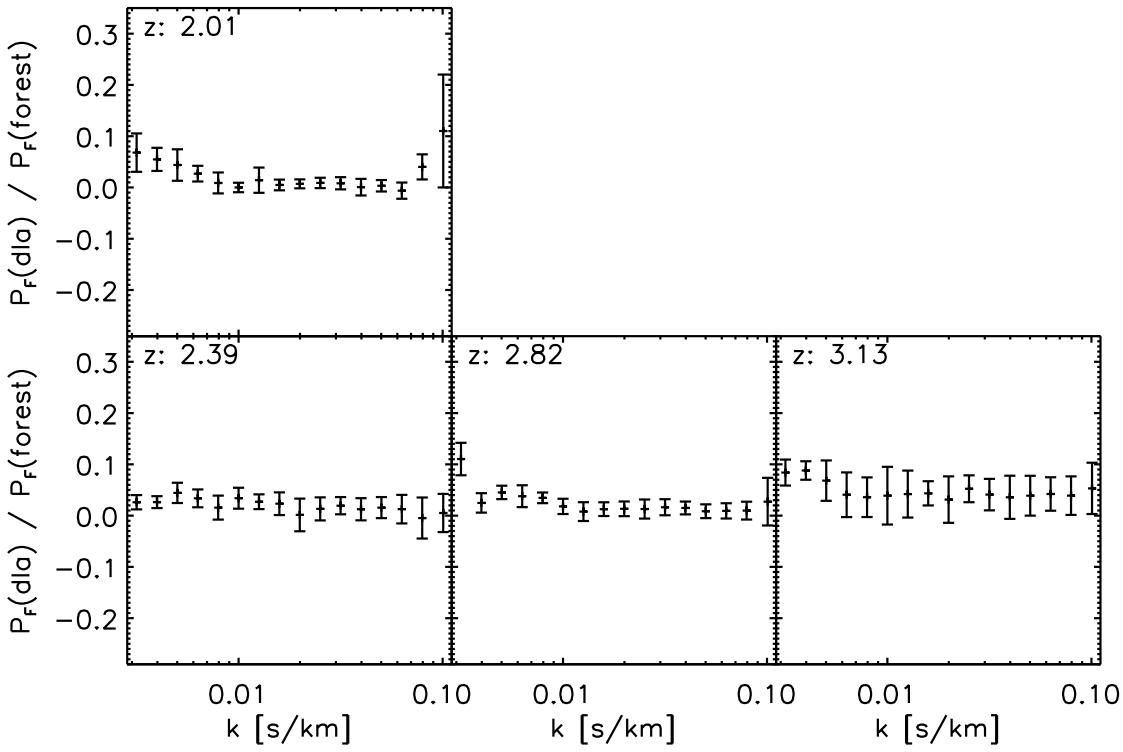

Figure 3.7: As Figure 3.6, but with DLA absorbers rather than metal lines.

the flux by the Voigt profile we have fit to the DLA line. DLA lines are present in 41 of our spectra. We report P_F both with and without these lines removed. DLA lines are easily identified in our spectra, and so their removal is straight forward. Figure 3.7 shows the contribution to the power spectrum from DLA lines. The mean effect is fairly small, contributing less than about 10% of the power at nearly all wavenumbers across all redshift bins. There are no DLA lines in the spectra of our 2 highest redshift bins.

3.5.3 Metal lines blending with HI lines

The power spectrum of the metal absorption on the red side of the QSO Lyα emission peak has been measured in HIRES spectra [15] and in SDSS spectra [21]. In the SDSS Lyα forest power spectrum estimate, a simple subtraction of the

red side metal power was done, with the reported power spectrum of HI absorption in the Lyα forest calculated as the average of the power of all absorption in the Lyα forest wavelength range minus the average of the power spectrum of the metals in the wavelength range 1268-1380 Å. This subtraction assumes that blending of the metal lines with HI lines does not alter the power spectrum of the metals which lie in the Lyα forest an assumption that is not entirely accurate. Blending of metal lines with HI lines alters the power of the metal lines for 2 reasons. First, the total absorption is not additive, but rather it is the optical depth that is summed. A metal line that lies inside the Lyα forest can be partially erased by an HI line at a nearby wavelength. Second, there is additional power added from the positions of the metal lines relative to the HI lines.

To demonstrate the effect of the blending of HI and metal lines, we used the metal absorbers in the wavelength range 1268-1380 Å, and artificially shift them into the Lyα forest . We created new blended spectra from all possible pairs of Lyα forest spectra and red side metal spectra, trimming the new spectrum length to the minimum of the length of the 2 contributing spectra. We then calculated the power spectrum of 3 quantities: the Lyα forest absorption alone ($P_F(forest)$), the metal absorption alone ($P_F(metal)$), and the artificially created blended spectrum ($P_F(blended)$). If the blending has no effect, as has been assumed in the past, then we would find that: $(P_F(blended) - P_F(forest))/P_F(metal) = 1$. We plot this quantity in Figure 3.8. There is a clear systematic increase in this value over that expected, which must be accounted for in any statistical subtraction of metal power from the Lyα forest. The effect is larger at higher redshifts, due to the higher mean absorption.

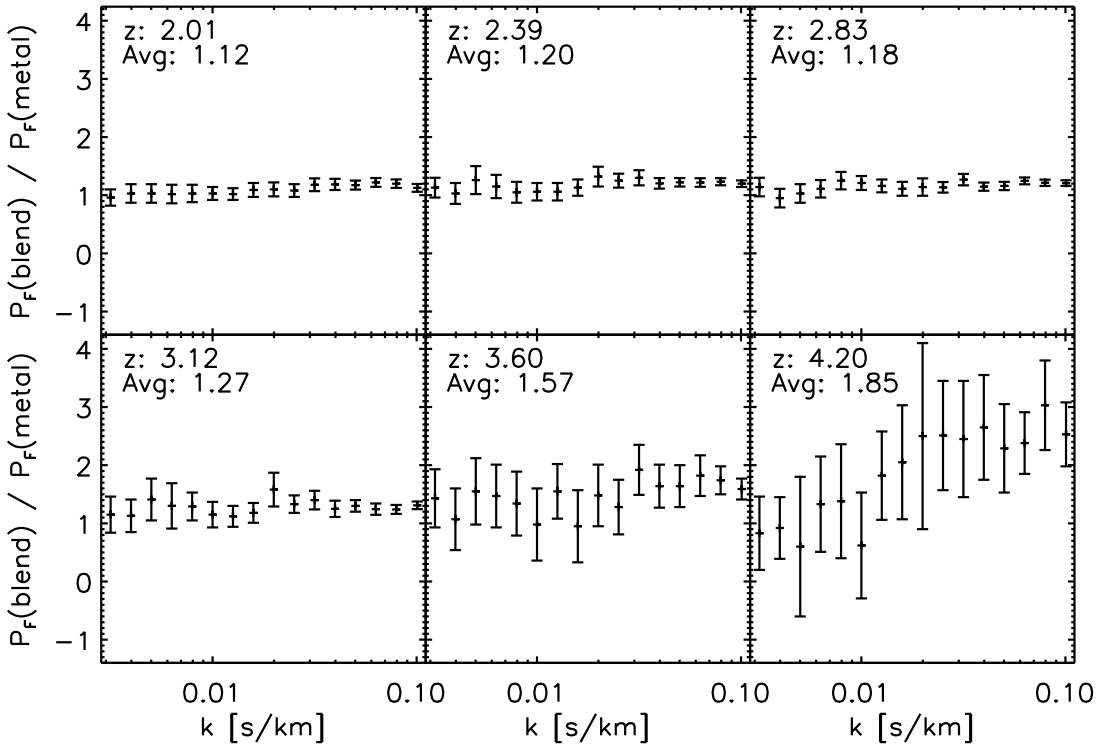

Figure 3.8: The increase in the Lyα forest power due to the presence of metal lines relative to the power of the metal lines alone. We artificially blended metal lines found in the wavelength range 1268-1380 Å with the Lyα forest. The value plotted is: $(P_F(blended) - P_F(forest))/P_F(metal)$, where $P_F(blended)$ is the power of the blended spectrum, $P_F(forest)$ is the power of the Lyα forest, and $P_F(metal)$ is the power of the metal lines alone.

3.5.4 Lyα forest power spectrum

Figure 3.9 shows the power spectrum with DLA absorbers removed and metals subtracted statistically. We present the data used in this plot in Table 3.4. We calculated the errors with the bootstrap method. Errors are larger for smaller wavenumbers because there are fewer values per wavenumber bin. The redshift bin at $z = 2.82$ contains the most spectra, and as a result, has the smallest errors and the smoothest plot. Although the matter power spectrum amplitude increases with decreasing redshift due to the gravitational collapse of overdense regions with time, the Lyα forest power spectrum has the opposite evolution. This is because there are fewer sources of ionizing radiation at higher redshifts, and as a result there is a higher neutral fraction of hydrogen and a larger optical depth to Lyα scattering.

3.5.5 Comparison with previous Lyα forest power measurements

Figure 3.10 shows our P_F measurement compared with all previously published values. It should be noted when viewing Figure 3.10 that our P_F values are strongly correlated across around 3 wavenumber bins, which accounts for some of the clustering of points that can be seen. Full covariance matrices for each redshift bin will be posted online when submitted for publication.

Although nearly all data is consistent within error bars, our values have a noticeable systematic offset compared to other high resolution values. In most cases, our data is lower than that of other groups, particularly at the largest wavenumbers, where metal removal, noise subtraction, spectral window functions, and gaps in the data become important. Given our discussion in §3.4, we do

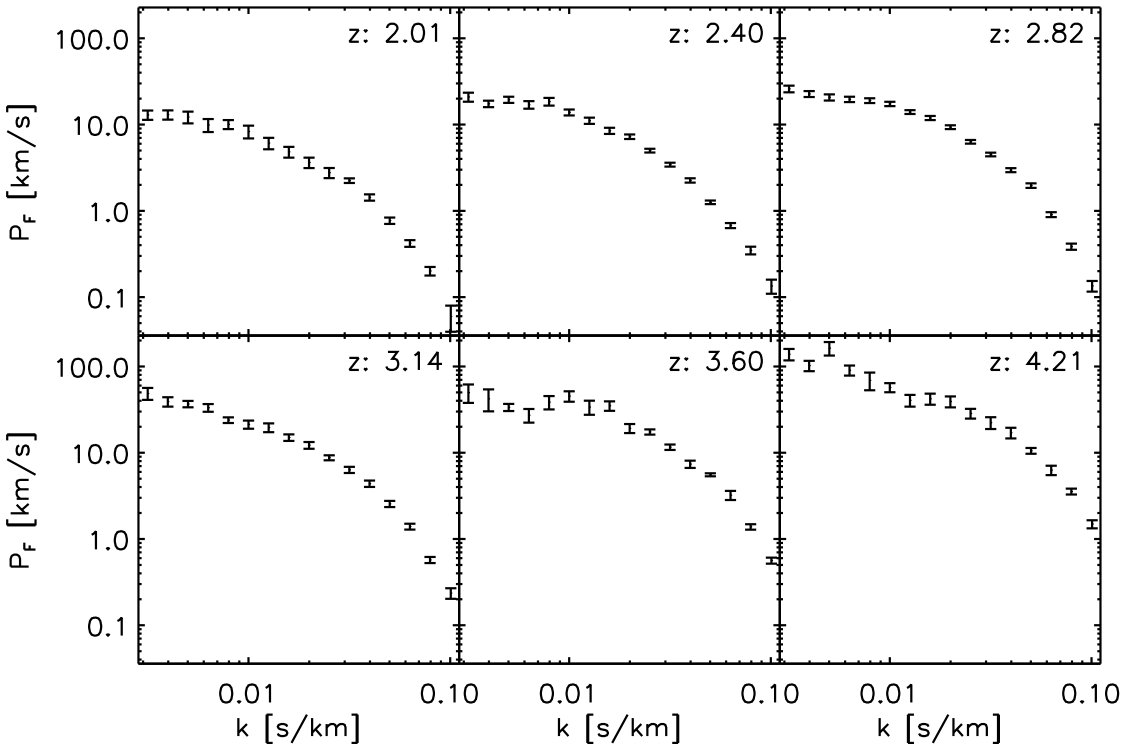

Figure 3.9: The power spectrum of the Lyα forest with DLA and metal lines removed. Only spectra with $S/N > 10$ were used for this plot. Data values are given in Table 3.4.

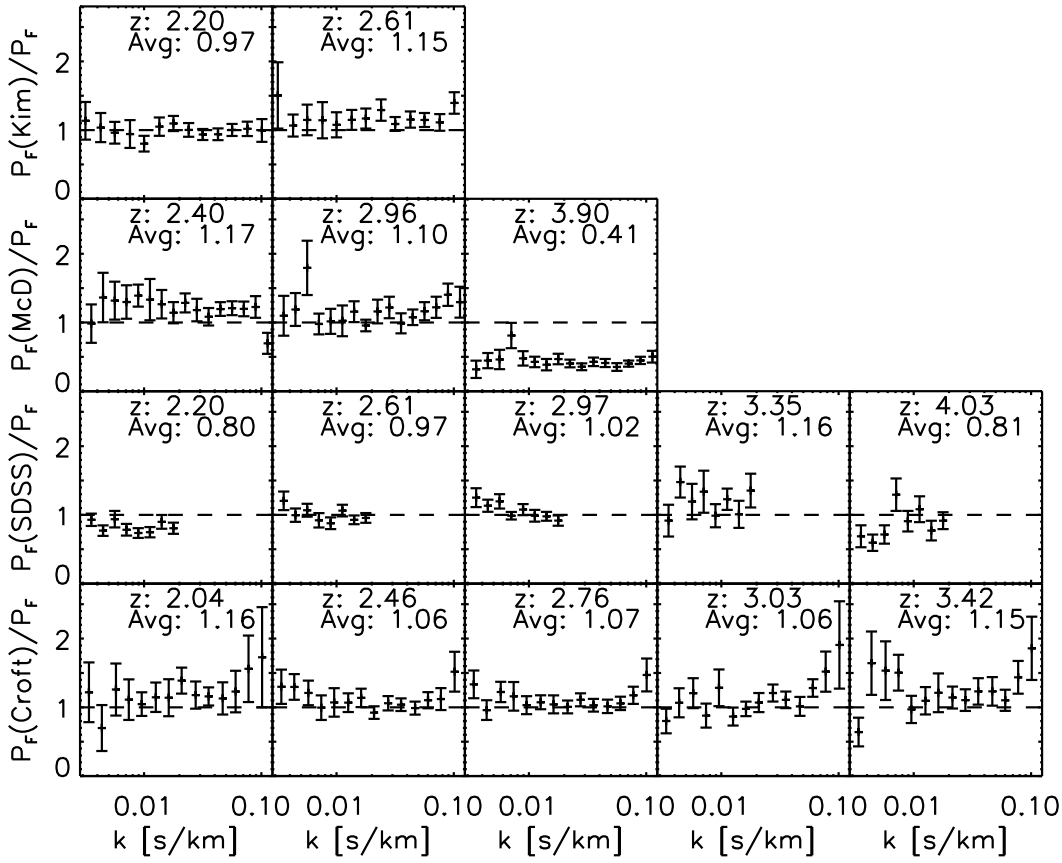

Figure 3.10: Comparison of our P_F measurement with that of previously published values. Kim data is from [15], McD data from [20], SDSS data from [22], and Croft data from [5]. For this plot only, we rebinned our P_F data to match the redshift and wavenumber binning of the data we are comparing against. We have removed DLAs and metals from the data we plot here. Note that only the SDSS and McD power [20, 22] removed metals from their data. The average values reported on the plots are weighted by the size of the errors for each wavenumber.

not expect the P_F values from [20] to be accurate at wavenumbers larger than around $logk = -1.3$ due to the gaps they introduced in their spectra for metal subtraction. Fortunately, when this data set was combined with the SDSS P_F in [22], the HIRES data was cut to $logk \leq -1.3$. Since no other group has previously removed metals from HIRES spectra for a P_F measurement, our reported values are the first to remove the systematic offset due to metal absorption at the smallest scales available in the Lyα forest, $-1.3 < logk <= -0.9$.

It can be seen from Figure 3.6 that metals are an important factor at all scales, particularly for $z < 3.4$. Since metals were not removed in [5] or [15], these data sets must have somewhat higher P_F than that of the Lyα forest alone, accounting for some of the offset we see in Figure 3.10. While the HIRES P_F reported by [20] should have fairly accurate metal subtraction at $logk <= -1.3$, our data set is more than 10 times as large as their 8 spectra.

We notice that the z = 3.87 redshift bin for the HIRES data set from [20] is farther below our measured values. It is difficult to see how this can be explained, particularly given our general agreement with the SDSS data at the closest redshift bin at z = 4.03.

3.5.6 Effects of our systematically lower small scale power

IGM temperature

As was discussed in §3.5.5, we find a systematic offset compared to previously published results due to metal absorption at the smallest scales available in the Lyα forest, $-1.3 < logk <= -0.9$. The power at these small scales is strongly related to the temperature, with a higher temperature leading to a reduction in power due to wider absorption lines. Given that our P_F is lower than previously

published data on the smallest scales, this leads to a higher temperature than would previously have been interpreted from the Lyα forest power spectrum [37].

Neutrino mass

In §3.5.3, we showed that there is a systematic offset in the Lyα forest flux power spectrum when subtracting metal power statistically if the blending of the metal lines with the HI lines is not taken into account. From Figure 3.8, a rough estimate of the systematic increase in the effect of metal absorption over the wavenumber range of SDSS ($k < 0.01778 s/km$) is around 15%. This corresponds to up to a 3% offset in their Lyα forest flux power spectrum measurement, with the largest effect being at low redshift and high wavenumber. This is only up to a third of an error bar for most of their data, but is significant, given that it masks the suppression of the power spectrum caused by the free streaming of massive neutrinos.

In reference [33], the SDSS data set was used to place the constraint: $\Sigma m_\nu \leq 0.9eV (2\sigma C.L.)$. This constraint was based on hydrodynamic cosmological simulations, which showed a 7% reduction in the Lyα forest flux power for $\Sigma m_\nu = 0.6eV$, and a $\sim 15\%$ reduction for $\Sigma m_\nu = 1.2eV$. The constraint reported implies that no suppression of the power spectrum was detected, and that a suppression of around $\sim 10\%$ could have been detected. Subtracting 3% from the SDSS power to account for the blending of metal lines with HI lines would allow for the presence of a larger neutrino mass, loosening the previously published constraints. The systematic offset due to the blending of metal and HI lines will need to be determined to greater precision for the upcoming BOSS measurement of P_F, for which the statistical errors will be significantly below 15% of the metal power amplitude.

3.6 Conclusions

We have presented a carefully calibrated measurement of the Lyα forest flux power spectrum from 91 high resolution, high S/N QSO spectra at redshifts $2.01 \leq z \leq 4.18$ and at scales $-2.5 \leq logk \leq -1.0 s/km$. We provide power spectrum measurements both with and without metal and DLA absorption removed. Through the use of the Welch spectral window function and Welch's Method, we avoid distortions caused by spectral leakage. We also avoid distortions that would be caused by placing gaps in the spectra for metal line removal by instead dividing the spectrum by the Voigt profile fits to the metal lines. By avoiding distortions caused by spectral leakage, metal absorption, and gaps in the spectra, we have achieved the first Lyα forest flux power spectrum measurement accurate down to scales as small as $k = 0.1 s/km$.

Our improvements to the power spectrum calculation method lead to a smaller power spectrum amplitude at the smallest scales compared to previous measurements, which in turn implies a hotter temperature of the IGM than previous estimates based on the Lyα forest flux power spectrum. The bulk of our results are consistent with previously published values within error bars, with a general trend of our data showing a moderate systematic reduction in power compared to other data sets.

We have also provided a measurement of the metal contribution to the power spectrum in the Lyα forest wavelength range. We have shown that the increase in the amplitude of the Lyα forest flux power spectrum due to metal absorption lines is greater than the power of the metal lines alone. This offset must be taken into account when subtracting metal power statistically, as will be necessary in the upcoming large sample of low resolution spectra that make up the BOSS data set. Taking this offset into account likely raises the allowed neutrino mass compared

to previous estimates based on the SDSS Lyα forest flux power spectrum.

Acknowledgments

This chapter is currently being prepared for submission for publication of the material. Day, Aaron; Tytler, David; Kirkman, David; Lopez, Liliana; Liang, Jia.

Table 3.4: Units of k are s/km, units of P_F are km/s. Each P_F measurement includes the QSO flux in the rest wavelength range 1070-1190 Å. For the measurements excluding DLA absorption, we adjust the flux through the use of Voigt profile line fits before we calculate P_F. For the measurement excluding metal absorption, the metals are subtracted statistically. Note that when we subtract DLA absorption, we also subtract metal absorption. A small amount of noise has been subtracted from all values, with the maximum noise subtraction less than 10% of the reported P_F value.

z	$logk$	P_F	P_F -M	P_F -M, DLA
2.01	-2.5	15.7 ± 1.6	14.0 ± 1.7	12.9 ± 1.6
	-2.4	15.4 ± 1.7	14.0 ± 1.8	13.0 ± 1.6
	-2.3	14.2 ± 1.8	12.8 ± 1.9	12.2 ± 1.9
	-2.2	11.4 ± 1.6	10.1 ± 1.7	9.9 ± 1.7
	-2.1	11.4 ± 1.1	10.2 ± 1.3	10.1 ± 1.2
	-2.0	10.2 ± 1.1	8.3 ± 1.5	8.3 ± 1.4
	-1.9	7.84 ± 0.61	6.13 ± 0.95	6.10 ± 0.92
	-1.8	6.06 ± 0.37	4.87 ± 0.69	4.83 ± 0.69
	-1.7	4.28 ± 0.38	3.67 ± 0.51	3.63 ± 0.50
	-1.6	3.40 ± 0.24	2.77 ± 0.38	2.77 ± 0.37
	-1.5	2.46 ± 0.12	2.27 ± 0.15	2.24 ± 0.14
	-1.4	1.61 ± 0.095	1.43 ± 0.12	1.43 ± 0.12
	-1.3	0.899 ± 0.052	0.772 ± 0.066	0.770 ± 0.066
	-1.2	0.482 ± 0.030	0.418 ± 0.036	0.420 ± 0.037
	-1.1	0.259 ± 0.018	0.211 ± 0.023	0.201 ± 0.023
	-1.0	0.121 ± 0.016	0.072 ± 0.023	0.060 ± 0.020
2.40	-2.5	23.6 ± 2.4	21.4 ± 2.6	20.9 ± 2.5
	-2.4	19.5 ± 1.4	17.9 ± 1.6	17.4 ± 1.5
	-2.3	21.2 ± 1.6	20.5 ± 1.7	19.4 ± 1.6
	-2.2	18.4 ± 1.7	17.6 ± 1.7	17.0 ± 1.7

Table 3.4 – continued from previous page

z	$logk$	P_F	P_F -M	P_F -M, DLA
	-2.1	19.5 ± 2.0	18.8 ± 2.0	18.5 ± 1.9
	-2.0	15.2 ± 1.1	14.3 ± 1.2	13.9 ± 1.1
	-1.9	12.15 ± 0.96	11.50 ± 0.98	11.11 ± 0.92
	-1.8	9.25 ± 0.72	8.72 ± 0.74	8.49 ± 0.70
	-1.7	7.54 ± 0.50	7.29 ± 0.50	7.24 ± 0.44
	-1.6	5.40 ± 0.27	5.07 ± 0.28	5.00 ± 0.25
	-1.5	3.69 ± 0.19	3.50 ± 0.19	3.43 ± 0.18
	-1.4	2.53 ± 0.12	2.31 ± 0.14	2.25 ± 0.13
	-1.3	1.434 ± 0.060	1.279 ± 0.071	1.257 ± 0.061
	-1.2	0.800 ± 0.037	0.686 ± 0.045	0.676 ± 0.046
	-1.1	0.423 ± 0.028	0.349 ± 0.034	0.348 ± 0.036
	-1.0	0.197 ± 0.013	0.149 ± 0.018	0.134 ± 0.025
2.82	-2.5	31.2 ± 2.3	28.9 ± 2.4	26.0 ± 2.3
	-2.4	24.8 ± 1.6	23.0 ± 1.7	22.7 ± 1.8
	-2.3	23.1 ± 1.7	21.4 ± 1.8	20.7 ± 1.7
	-2.2	21.9 ± 1.6	20.4 ± 1.7	19.6 ± 1.4
	-2.1	20.9 ± 1.3	19.6 ± 1.3	19.0 ± 1.2
	-2.0	19.2 ± 1.1	17.8 ± 1.2	17.4 ± 1.0
	-1.9	15.40 ± 0.72	14.13 ± 0.79	13.99 ± 0.71
	-1.8	12.84 ± 0.68	12.01 ± 0.71	11.93 ± 0.65
	-1.7	9.92 ± 0.54	9.39 ± 0.56	9.34 ± 0.48
	-1.6	7.08 ± 0.27	6.35 ± 0.34	6.32 ± 0.31
	-1.5	4.99 ± 0.20	4.55 ± 0.25	4.50 ± 0.22
	-1.4	3.40 ± 0.13	2.99 ± 0.18	2.96 ± 0.16
	-1.3	2.25 ± 0.11	1.96 ± 0.14	1.97 ± 0.12
	-1.2	1.087 ± 0.042	0.906 ± 0.064	0.905 ± 0.059
	-1.1	0.516 ± 0.018	0.382 ± 0.035	0.385 ± 0.032
	-1.0	0.219 ± 0.010	0.144 ± 0.021	0.135 ± 0.019
3.14	-2.5	55.5 ± 8.1	53.0 ± 8.2	48.7 ± 7.7
	-2.4	44.5 ± 5.2	42.3 ± 5.3	39.1 ± 4.9
	-2.3	40.7 ± 3.3	39.1 ± 3.3	36.8 ± 3.1
	-2.2	35.8 ± 3.5	34.6 ± 3.5	33.2 ± 3.4
	-2.1	26.0 ± 2.0	24.7 ± 2.0	23.9 ± 1.8
	-2.0	24.0 ± 2.0	22.0 ± 2.1	21.3 ± 2.3
	-1.9	22.3 ± 2.1	20.4 ± 2.2	19.6 ± 2.3
	-1.8	16.8 ± 1.5	15.4 ± 1.6	15.0 ± 1.3
	-1.7	13.2 ± 1.1	12.5 ± 1.1	12.2 ± 1.1
	-1.6	10.05 ± 0.71	9.24 ± 0.74	8.76 ± 0.58
	-1.5	7.11 ± 0.58	6.58 ± 0.60	6.34 ± 0.52
	-1.4	4.92 ± 0.39	4.51 ± 0.40	4.38 ± 0.37

Table 3.4 – continued from previous page

z	$logk$	P_F	P_F -M	P_F -M, DLA
	-1.3	2.94 ± 0.22	2.62 ± 0.23	2.55 ± 0.21
	-1.2	1.63 ± 0.12	1.43 ± 0.13	1.39 ± 0.11
	-1.1	0.720 ± 0.048	0.583 ± 0.055	0.572 ± 0.046
	-1.0	0.337 ± 0.029	0.247 ± 0.035	0.235 ± 0.033
3.60	-2.5	53 ± 11	50 ± 12	50 ± 12
	-2.4	44 ± 12	42 ± 12	42 ± 12
	-2.3	35.8 ± 3.0	34.4 ± 3.1	34.4 ± 3.1
	-2.2	29.5 ± 4.8	27.8 ± 4.9	27.8 ± 4.9
	-2.1	40.1 ± 6.8	38.1 ± 6.8	38.1 ± 6.8
	-2.0	46.6 ± 6.3	45.4 ± 6.3	45.4 ± 6.3
	-1.9	35.2 ± 6.3	33.7 ± 6.3	33.7 ± 6.3
	-1.8	35.7 ± 4.3	35.2 ± 4.4	35.2 ± 4.4
	-1.7	19.9 ± 2.3	19.2 ± 2.3	19.2 ± 2.3
	-1.6	17.9 ± 1.2	17.4 ± 1.2	17.4 ± 1.2
	-1.5	12.13 ± 0.83	11.72 ± 0.84	11.72 ± 0.84
	-1.4	7.74 ± 0.71	7.41 ± 0.72	7.41 ± 0.72
	-1.3	5.79 ± 0.21	5.54 ± 0.22	5.54 ± 0.22
	-1.2	3.38 ± 0.38	3.25 ± 0.39	3.25 ± 0.39
	-1.1	1.501 ± 0.096	1.377 ± 0.099	1.377 ± 0.099
	-1.0	0.644 ± 0.039	0.562 ± 0.043	0.562 ± 0.043
4.21	-2.5	140 ± 21	139 ± 21	139 ± 21
	-2.4	103 ± 14	102 ± 14	102 ± 14
	-2.3	164 ± 29	163 ± 29	163 ± 29
	-2.2	92 ± 12	91 ± 12	91 ± 12
	-2.1	71 ± 16	69 ± 16	69 ± 16
	-2.0	57.7 ± 6.8	56.7 ± 6.9	56.7 ± 6.9
	-1.9	41.9 ± 6.2	40.5 ± 6.2	40.5 ± 6.2
	-1.8	43.8 ± 6.1	42.3 ± 6.2	42.2 ± 6.2
	-1.7	40.1 ± 5.7	39.2 ± 5.7	39.2 ± 5.7
	-1.6	29.7 ± 3.7	28.7 ± 3.7	28.7 ± 3.7
	-1.5	23.1 ± 3.5	22.0 ± 3.5	22.0 ± 3.5
	-1.4	17.9 ± 2.4	17.0 ± 2.4	17.0 ± 2.4
	-1.3	11.04 ± 0.75	10.43 ± 0.83	10.43 ± 0.83
	-1.2	6.62 ± 0.75	6.24 ± 0.78	6.24 ± 0.78
	-1.1	3.75 ± 0.27	3.55 ± 0.28	3.55 ± 0.28
	-1.0	1.59 ± 0.16	1.48 ± 0.16	1.48 ± 0.16

Bibliography

[1] A. Boyarsky, J. Lesgourgues, O. Ruchayskiy, and M. Viel. Lyman-α constraints on warm and on warm-plus-cold dark matter models. *Journal of Cosmology and Astro-Particle Physics*, 5:12–+, May 2009.

[2] A. Boyarsky, J. Lesgourgues, O. Ruchayskiy, and M. Viel. Realistic Sterile Neutrino Dark Matter with KeV Mass does not Contradict Cosmological Bounds. *Physical Review Letters*, 102(20):201304–+, May 2009.

[3] R. Cen, J. Miralda-Escude, J. P. Ostriker, and M. Rauch. Gravitational collapse of small-scale structure as the origin of the Lyman-alpha forest. *ApJ*, 437:L9–L12, Dec. 1994.

[4] R. A. C. Croft, W. Hu, and R. Davé. Cosmological Limits on the Neutrino Mass from the LyAlpha Forest. *Physical Review Letters*, 83:1092, Aug. 1999.

[5] R. A. C. Croft, D. H. Weinberg, M. Bolte, S. Burles, L. Hernquist, N. Katz, D. Kirkman, and D. Tytler. Toward a Precise Measurement of Matter Clustering: Lyα Forest Data at Redshifts 2-4. *ApJ*, 581:20, Dec. 2002.

[6] R. A. C. Croft, D. H. Weinberg, N. Katz, and L. Hernquist. Recovery of the Power Spectrum of Mass Fluctuations from Observations of the Ly alpha Forest. *ApJ*, 495:44, Mar. 1998.

[7] R. A. C. Croft, D. H. Weinberg, M. Pettini, L. Hernquist, and N. Katz. The Power Spectrum of Mass Fluctuations Measured from the LYalpha Forest at Redshift Z=2.5. *ApJ*, 520:1–23, July 1999.

[8] J. Dunkley, E. Komatsu, M. R. Nolta, D. N. Spergel, D. Larson, G. Hinshaw, L. Page, C. L. Bennett, B. Gold, N. Jarosik, J. L. Weiland, M. Halpern, R. S. Hill, A. Kogut, M. Limon, S. S. Meyer, G. S. Tucker, E. Wollack, and E. L. Wright. Five-Year Wilkinson Microwave Anisotropy Probe Observations: Likelihoods and Parameters from the WMAP Data. *ApJS*, 180:306–329, Feb. 2009.

[9] N. Y. Gnedin and A. J. S. Hamilton. Matter power spectrum from the Lyman-alpha forest: myth or reality? *MNRAS*, 334:107, July 2002.

[10] L. Hernquist, N. Katz, D. H. Weinberg, and M. Jordi. The Lyman-Alpha Forest in the Cold Dark Matter Model. *ApJ*, 457:L51, Feb. 1996.

[11] E. M. Hu, T. Kim, L. L. Cowie, A. Songaila, and M. Rauch. The Distribution of Column Densities and B Values in the Lyman-Alpha Forest. *AJ*, 110:1526, Oct. 1995.

[12] L. Hui. Recovery of the Shape of the Mass Power Spectrum from the Lyalpha Forest. *ApJ*, 516:519, May 1999.

[13] L. Hui, S. Burles, U. Seljak, R. E. Rutledge, E. Magnier, and D. Tytler. On Estimating the QSO Transmission Power Spectrum. *ApJ*, 552:15, May 2001.

[14] T. Jena, M. L. Norman, D. Tytler, D. Kirkman, N. Suzuki, A. Chapman, C. Melis, P. Paschos, B. O'Shea, G. So, D. Lubin, W. Lin, D. Reimers, E. Janknecht, and C. Fechner. A concordance model of the Lyman α forest at z= 1.95. *MNRAS*, 361:70–96, July 2005.

[15] T.-S. Kim, M. Viel, M. G. Haehnelt, R. F. Carswell, and S. Cristiani. The power spectrum of the flux distribution in the Lyman α forest of a large sample of UVES QSO absorption spectra (LUQAS) (also erratum). *MNRAS*, 347:355, Jan. 2004.

[16] D. Kirkman, D. Tytler, N. Suzuki, C. Melis, S. Hollywood, K. James, G. So, D. Lubin, T. Jena, M. L. Norman, and P. Paschos. The H I opacity of the intergalactic medium at redshifts $1.6 < z < 3.2$. *MNRAS*, 360:1373–1380, July 2005.

[17] E. Komatsu, J. Dunkley, M. R. Nolta, C. L. Bennett, B. Gold, G. Hinshaw, N. Jarosik, D. Larson, M. Limon, L. Page, D. N. Spergel, M. Halpern, R. S. Hill, A. Kogut, S. S. Meyer, G. S. Tucker, J. L. Weiland, E. Wollack, and E. L. Wright. Five-Year Wilkinson Microwave Anisotropy Probe Observations: Cosmological Interpretation. *ApJS*, 180:330–376, Feb. 2009.

[18] N. R. Lomb. Least-squares frequency analysis of unequally spaced data. *Ap&SS*, 39:447–462, Feb. 1976.

[19] P. McDonald, J. Miralda-Escudé, M. Rauch, W. L. W. Sargent, T. A. Barlow, and R. Cen. A Measurement of the Temperature-Density Relation in the Intergalactic Medium Using a New Lyα Absorption-Line Fitting Method. *ApJ*, 562:52–75, 2001.

[20] P. McDonald, J. Miralda-Escudé, M. Rauch, W. L. W. Sargent, T. A. Barlow, R. Cen, and J. P. Ostriker. The Observed Probability Distribution Function, Power Spectrum, and Correlation Function of the Transmitted Flux in the Lyα Forest. *ApJ*, 543:1–23, Nov. 2000.

[21] P. McDonald, U. Seljak, S. Burles, , et al. The Lyα Forest Power Spectrum from the Sloan Digital Sky Survey. *ApJS*, 163:80–109, Mar. 2006.

[22] P. McDonald, U. Seljak, R. Cen, D. Shih, D. H. Weinberg, S. Burles, D. P. Schneider, D. J. Schlegel, N. A. Bahcall, J. W. Briggs, J. Brinkmann, M. Fukugita, Ž. Ivezić, S. Kent, and D. E. Vanden Berk. The Linear Theory

Power Spectrum from the Lyα Forest in the Sloan Digital Sky Survey. *ApJ*, 635:761–783, Dec. 2005.

[23] P. Petitjean, J. P. Mueket, and R. E. Kates. The LY alpha forest at low redshift: Tracing the dark matter filaments. *A&A*, 295:L9–L12, Mar. 1995.

[24] W. H. Press and G. B. Rybicki. Fast algorithm for spectral analysis of unevenly sampled data. *ApJ*, 338:277–280, Mar. 1989.

[25] J. D. Scargle. Studies in astronomical time series analysis. II - Statistical aspects of spectral an alysis of unevenly spaced data. *ApJ*, 263:835–853, Dec. 1982.

[26] J. Schaye, T. Theuns, M. Rauch, G. Efstathiou, and W. L. W. Sargent. The thermal history of the intergalactic medium*. *MNRAS*, 318:817, Nov. 2000.

[27] U. Seljak, A. Makarov, P. McDonald, and and others. Cosmological parameter analysis including SDSS Lyα forest and galaxy bias: Constraints on the primordial spectrum of fluctuations, neutrino mass, and dark energy. *PhysRevD*, 71(10):3515, May 2005.

[28] U. Seljak, A. Makarov, P. McDonald, and H. Trac. Can Sterile Neutrinos Be the Dark Matter? *Physical Review Letters*, 97(19):191303–+, Nov. 2006.

[29] D. N. Spergel, L. Verde, H. V. Peiris, E. Komatsu, M. R. Nolta, C. L. Bennett, M. Halpern, G. Hinshaw, N. Jarosik, A. Kogut, M. Limon, S. S. Meyer, L. Page, G. S. Tucker, J. L. Weiland, E. Wollack, and E. L. Wright. First-Year Wilkinson Microwave Anisotropy Probe (WMAP) Observations: Determination of Cosmological Parameters. *ApJS*, 148:175–194, Sept. 2003.

[30] T. Theuns, A. Leonard, G. Efstathiou, F. Pearce, and P. Thomas. Dependencies of QSO Lyα absorption line statistics on cosmological parameters. *MNRAS*, 303:L58, 1998.

[31] T. Theuns and S. Zaroubi. A wavelet analysis of the spectra of quasi-stellar objects. *MNRAS*, 317:989–995, Oct. 2000.

[32] M. Viel, M. G. Haehnelt, and V. Springel. Inferring the dark matter power spectrum from the Lyman α forest in high-resolution QSO absorption spectra. *MNRAS*, 354:684–694, Nov. 2004.

[33] M. Viel, M. G. Haehnelt, and V. Springel. The effect of neutrinos on the matter distribution as probed by the intergalactic medium. *Journal of Cosmology and Astro-Particle Physics*, 6:15–+, June 2010.

[34] M. Viel, J. Lesgourgues, M. G. Haehnelt, S. Matarrese, and A. Riotto. Constraining warm dark matter candidates including sterile neutrinos and light gravitinos with WMAP and the Lyman-α forest. *Phys. Rev. D*, 71(6):063534–+, Mar. 2005.

[35] M. Viel, J. Lesgourgues, M. G. Haehnelt, S. Matarrese, and A. Riotto. Can Sterile Neutrinos Be Ruled Out as Warm Dark Matter Candidates? *Physical Review Letters*, 97(7):071301–+, Aug. 2006.

[36] P. D. Welch. The Use of Fast Fourier Transform for the Estimation of Power Spectra: A Method Based on Time Averaging Over Short, Modified Per iodograms. *IEEE Trans. Audio Electroacoust.*, AU-15:70–73, 1967.

[37] M. Zaldarriaga, L. Hui, and M. Tegmark. Constraints from the Lyα Forest Power Spectrum. *ApJ*, 557:519–526, Aug. 2001.

[38] Y. Zhang, P. Anninos, M. L. Norman, and A. Meiksin. Spectral Analysis of the Ly alpha Forest in a Cold Dark Matter Cosmology. *ApJ*, 485:496, Aug. 1997.

3.7 Appendix: Technical details

In this appendix, we describe technical details of the process that we took to calculate the power spectrum. These details are only discussed in this thesis, and not in the original paper. While they are not necessary to present our results or show their accuracy, they do show the level of work that was required to complete this thesis.

3.7.1 Data reduction

After reducing the data using the standard MAKEE reduction software, we then used our proprietary software to fit continua to the spectra, and to provide absorption line fits to DLA absorption lines. The end result of this process is an ascii file for each QSO, containing the observed wavelength, absolute raw flux level, continuum flux level, error value, and the flux value of any fitted lines.

3.7.2 Power spectrum calculation

We wrote over 12000 lines of C++ code to perform the Lyα forest flux power spectrum calculation. The code parses the QSO spectrum files output from the data reduction process, calculates the SNR of a spectrum, performs SNR and redshift binning, handles bad pixels, estimates the power spectrum of the noise, calculates the power spectrum of the Lyα forest performs wavenumber binning, handles the details of the statistical subtraction of the power spectrum of the metals, and calculates errors using the bootstrap method. To ensure consistency, the code is also able to calculate the power spectrum of artificial QSO spectra created from computer simulations. This code has been extensively tested for accuracy and consistency. Most importantly, we have tested that the power spectrum calculation we perform using the Lomb-Scargle Periodogram method yields the same result as a simple FFT for spectra without gaps.

Data binning

Before calculating the power spectrum, the QSO spectra are binned by both redshift and S/N. Redshift binning is straight forward, since the observed wavelength corresponds to a specific redshift. S/N binning is complicated by the fact that in an absorber the flux can drop to 0, while clearly the signal is not 0 in this case. Also, the noise level in a single QSO spectrum is a function of wavelength. To handle this, we fit a best fit line to the S/N level in each spectrum. We then use the equation for this line to define the S/N level for a given wavelength in the spectrum. Using this definition, if the S/N is less than 10, we discard the data as discussed in §3.4.8.

Error pixels and noise power

The error values for each pixel represent an estimate of the noise level as calculated by the data reduction process. Negative values indicate bad pixels, which are present in every spectrum due to cosmic rays which hit the CCD detector during the data acquisition process, or due to order join gaps in the spectra due to limitations of the spectrograph when observing at particular wavelengths. A bad pixel is defined as a pixel with SNR < 2.0 or a negative error value. If there are fewer than 25 consecutive bad pixels, then a bad pixel is replaced by the value of the flux at the previous acceptable pixel. If there are greater than 25 consecutive bad pixels, then that region of the spectrum is not used in the Lomb-Scargle Periodogram method. The number 25 was chosen through tests of the effect of gaps on the power spectrum calculation. We used thousands of artificially created QSO spectra from cosmological computer simulations, and superimposed the error pixels from the actual spectra. For this process, the artificial spectra were cut to the same length as the actual spectra. We then calculated the power spectrum both with and without the effects of the gaps, as was shown in §3.4.7.

Chapter 4

Questioning neutrino mass constraints from the Lyα forest

4.1 Abstract

The standard way to analyze Lyα forest data is by comparison with large hydrodynamic simulations. We show that it is not possible to match the typical simulation to Lyα forest data. We show this incompatibility using just two Lyα forest statistics: the mean amount of absorption and the power spectrum of the flux overdensity on scales $-2.0 \leq logk \leq -1.0$. Not only can these statistics not be matched together, but the shape of the power spectrum at these scales in simulations does not match observations. We use a set of 44 fully hydrodynamic simulations run with different ionizing backgrounds and thermal histories, as well as differing cosmological parameters. We do not perform any post processing of the simulation outputs. We use a uniform ionizing background in the optically thin limit, with extra heating for each HeII ionization to approximate radiative transfer effects. We vary the spectrum of the uniform ultraviolet background radiation, σ_8 and n_s, and we test models with heating from a hard X-ray background from AGNs and heating by TeV gamma rays from blazars. We make our comparison

at four redshifts: 2.0, 2.4, 2.8, and 3.2. The compatibility is poor at redshift 2.0, and becomes worse with increasing redshift. Our results suggest that the ionization history of the intermediate density intergalactic medium that causes the absorption that makes up the Lyα forest does not match the model generally used. This calls into question previous constraints placed on the neutrino mass and other cosmological parameters, which are derived from hydrodynamic simulations.

4.2 Introduction

In this paper we show that the standard hydrodynamic simulations of cosmic structure formation, although the best tools we have for decoding Lyα forest data, are not yet up to the task of fully utilizing the precision of observational data in making quantitative measurements of cosmological parameters. The Lyα forest, which is made up of redshifted Lyα absorption lines along the line of sight to a QSO, is itself a sensitive probe of both cosmological and astrophysical parameters.

The problem lies in the methodology used in determining cosmological parameters from the data. Statistics of the Lyα forest have been used by many groups in the past to place constraints on cosmological and astrophysical parameters. These constraints, however, are no better than the physical models used, which in most cases were no better than the simulations we examine here. With ever decreasing statistical errors in observational data from the growing SDSS quasar spectra data set and from HIRES and UVES spectra which accurately probe even smaller scales, it is necessary to increase the accuracy of the simulations both to decrease systematic errors and to verify the correctness of the physical models used.

Of particular interest is the determination of the linear matter power spectrum from the Lyα forest data, from which a wealth of cosmological and astrophysical data can be extracted. The hydrogen density distribution causing the Lyα forest absorption follows the overall matter density, modified by baryonic

physics. A measurement of the power spectrum of the flux of the Lyα forest can be combined with a detailed model of the intergalactic medium (IGM) to produce a measurement of the linear matter power spectrum, as has been attempted several times, including by [11, 27, 10, 39, 30].

One reason for interest in the linear matter power spectrum at small scales is the possibility of using it to place constraints on the masses of active neutrinos or on warm dark matter (WDM). Free streaming by light, initially relativistic particles will suppress the matter power spectrum on scales that are inside of the Lyα forest [5, 9, 35, 40]. Small scale power is also suppressed by higher temperatures in the IGM, due to increased Jeans length as well as increased doppler broadening of Lyα absorption lines. The degeneracy of this suppression of small scale power with that caused by the free streaming of light particles can be lifted through measurements which uniquely constrain the temperature, such as statistics of the Lyα or metal line widths. It is critical that any simulation used to extract limits on the masses of light, free streaming particles have the appropriate thermal and ionization conditions in the IGM. This can only be achieved through the comparison of multiple observational statistics.

In this paper, we use fully hydrodynamic simulations run with the code ENZO, which implements a widely used model consisting of an optically thin IGM with a uniform ultraviolet background (UVB). Given that the neutral fraction of both hydrogen and helium is less than $\sim 10^{-3}$ in the bulk of the Lyα forest, and the mean free path of an ionizing photon is greater than 50 Mpc [17], the optically thin approximation is valid for photons that ionize HI and HeI. Sources of ionizing radiation, including galaxies and quasars, are separated by much smaller distances than the mean free path of ionizing photons, and so the HI and HeI ionizing radiation field should be approximately uniform [15, 25]. The precise timing and process through which hydrogen was ionized and helium was singly ionized is not important for the redshift range considered here. This is because over time, photoionization equilibrium will be reached in which photoheating is

balanced by adiabatic cooling. This process will erase any initial inhomogeneity of the ionization, and the temperature will asymptotically approach a form given by the UVB [18, 19].

A complication in the modeling of the thermal state of the IGM arises due to a variety of uncertain heating sources, including heating from HeII ionization, X-rays, and blazars. HeII ionization is known to occur, but the radiative transfer physics that controls the thermal impact on the IGM is computationally expensive, and so is not usually included when interpreting Lyα forest statistics. The galaxies that likely caused the ionization of HI and HeI did not produce enough energetic photons to significantly doubly ionize helium. It wasn't until much later, sometime around $z \sim 2.7$ [41], that helium became doubly ionized, likely by quasars. This process raised the temperature of the IGM through photoheating. The timing of HeII ionization and the ionizing spectrum are particularly important, as the completion of the ionization process likely occurred around the same epoch as the middle of the redshift range of the Lyα forest data. We add a constant extra heating term for each HeII ionization in our simulations to approximate radiative transfer effects during the HeII ionization process. Other sources of heating, including X-rays and blazars, are difficult to observe and so their effects are poorly constrained. In this paper, we run several simulations including a variety of X-ray and blazar heating models.

The layout of the paper is as follows. In §4.3, we describe the observational data sets we use. In §4.4, we present the 44 hydrodynamic ENZO simulations we ran. In §4.5, we compare the simulations we ran to the observational data sets. Finally, in §4.6 we discuss the implications of our results.

4.3 Observational Data

We use observational data for two statistics of the Lyα forest, the power spectrum of the flux overdensity, and the mean effective optical depth to Lyα

Table 4.1: Observational data. P_{-2} at z=2 is extrapolated using data values at z=2.2 and 2.4, since the data stops at z=2.2.

z	τ_{eff}	P_{-2}	$P_{-1.5}$	P_{-1}
3.2	0.387 ± 0.036	24.84 ± 0.90	6.3 ± 0.6	0.232 ± 0.032
2.8	0.279 ± 0.021	18.14 ± 0.55	4.44 ± 0.28	0.137 ± 0.020
2.4	0.198 ± 0.018	11.52 ± 0.41	3.26 ± 0.19	0.156 ± 0.021
2.0	0.136 ± 0.0069	6.7 ± 0.38	2.05 ± 0.12	0.091 ± 0.025

Table 4.2: Input parameter and output statistic definitions.

Parameter	Description
τ_{eff}	Mean effective optical depth ($-ln$(mean flux))
$P_{log(k)}$	Power spectrum of flux overdensity at $log(k)$ s/km
Box Size	Side length of simulation cube (comoving Mpc)
Cell Size	Cell size in simulation cube (comoving kpc)
γ_{912}	Factor multiplying UVB ionization and photoheating rates
X_{228}	Factor multiplying photoheating rate per HeII ionization
Γ_{228}	Factor multiplying ionization rate of HeII
σ_8	Present linear matter power spectrum amplitude at $8h^{-1}Mpc$
n_s	Spectral index of primordial matter power spectrum

absorption.

4.3.1 Lyα forest flux power spectrum

For the Lyα forest flux power spectrum, we use two separate data sets: the SDSS data set [28], consisting of approximately 3,000 QSO spectra, and a HIRES data set consisting of 91 high resolution, high S/N QSO spectra reported in Chapter 3. The SDSS data set is by far the largest currently available, by almost 2 orders of magnitude. It thus has the smallest statistical errors. However, the low resolution of the SDSS spectra limits the smallest scales to $k \leq 0.01778 s/km$. The inclusion of the HIRES spectra yields scales as small as $k = 0.1 s/km$. The smallest scales are particularly sensitive to the temperature, where the line widths, which are strongly influenced by doppler broadening, are effectively being measured. It was shown in Chapter 3 that these two data sets are consistent at overlapping scales.

The power spectrum is taken of the flux overdensity, which is defined to be

$$\delta_f \equiv \frac{f - \bar{f}}{\bar{f}}, \tag{4.1}$$

where f is the flux in units of the continuum level, and $\bar{f}$ is the mean flux of an individual spectrum. The power spectrum is then given by:

$$P_f(k) = \delta_f(k)^* \delta_f(k). \tag{4.2}$$

We use three wavenumbers, $log(k) = -2.0$, -1.5, and -1.0, denoted by: P_{-2}, $P_{-1.5}$, and P_{-1} respectively. We chose the largest scale to be at $log(k) = -2.0$ because it is sensitive to the cosmological model, and larger than the scale where the power spectrum is most sensitive to the temperature. If we were to choose a larger scale for the power, we would also require larger simulation boxes for comparison and more computer time. The smaller scales provide information about the shape of the power spectrum, and also the temperature of the IGM. The temperature is particularly important because it controls the recombination rate, which balances photoionizations to set the neutral fraction of hydrogen throughout the IGM.

4.3.2 Mean effective optical depth

We use the mean effective optical depth (τ_{eff}) data from [23]. This data set consists of 24 HIRES spectra. Absorption from metal lines and from Lyman-limit systems and damped Lyα systems is removed from these spectra, since it is also not included in standard simulations. The main uncertainty in determining the optical depth comes from the continuum fitting procedure. We verified that τ_{eff} from other data sets [21, 14, 36] is consistent enough that our results are not dependent on the particular data set used.

4.4 ENZO IGM Simulations

We use a suite of 44 fully hydrodynamic simulations run with the simulation code ENZO. We examine the values of τ_{eff} and P_{-2}, $P_{-1.5}$, and P_{-1} produced when we adjust the amplitude and shape of the ionizing background, as well as several cosmological parameters. Our simulations follow both cold dark matter (CDM) and baryonic gas with hydrodynamic physics implemented on a uniform grid. The simulations calculate cooling rates using collisional and radiative processes for 6 species: H, H+, He, He+, He++, and e- [31, 1, 3].

For the bulk of the simulations, we start at $z = 60$ using the transfer function of [13]. The simulated volumes are all cubes with strictly periodic boundary conditions. The simulations model HI, HeI, and HeII gas that is optically thin to ionizing radiation (with the exception of 1 simulation we ran to test self shielding effects). The simulations do not include metal cooling, as it has been shown to be negligible at the scales used in this paper, and only important at the smallest scales probed by HIRES spectra, with around a 9% maximum shift of small scale flux power [30]. The simulations do not include feedback from individual stars or QSOs, which has also been shown to have a small effect on the power at the scales we use here [30].

4.4.1 Ionizing background radiation

In the optically thin limit for a uniform ionizing background, there are just 6 parameters that completely specify the background radiation in the IGM: the photoionization rates and photoheating rates of HI, HeI, and HeII. Since the Lyα forest is made up of HI absorption, to first order there are 2 relevant parameters: the photoionization rate of HI and the heating from all sources. The heating effects the Lyα forest through the doppler broadening of line profiles, pressure smoothing, and most importantly, through the recombination rate. Hydrogen in the IGM is in photoionization equilibrium, with the photoionization rate balanced

by the temperature dependent recombination rate.

For the bulk of our simulations, we use the ionizing background radiation model from [16], adjusting both the amplitude of the radiation field and the heating rate per HeII ionization, as in [20] and [37]. The parameter γ_{912} is defined to be the same constant factor that multiplies the photoionization and photoheating rates for each HI, HeI, and HeII ionization. This sets the amplitude of the UVB without changing the spectral shape. The parameter X_{228} is the constant that multiplies the photoheating rate per HeII ionization. Changing X_{228} does not explicitly change the shape of the UVB. Rather, it corrects for the heat missing due to the lack of radiative transfer in the simulations. Both γ_{912} and X_{228} are in units of the values calculated from the UVB spectrum model used, either [16] or [17], with a value of 1 corresponding to no modification to the spectrum.

As a further test of the importance of the spectral shape of the ionizing background, we ran 8 of our simulations utilizing the more recently published ionization and heating rates from [17]. These new rates have a substantially different shape than the old ones, due to the addition of several important pieces of physics, including the sawtooth modulation of the background intensity from resonant line absorption in the Lyman series of hydrogen and helium [17].

We also ran a single simulation utilizing the ionization model described in [7], which is similar to what was used in the SDSS Lyα forest power spectrum analysis [30]. This model internally calculates the full spectrum of the radiation field from the star formation rate. Since the full spectral energy distribution of the ionizing radiation is available in this model only, this is the only simulation for which the cross section of HI was calculated and used to apply self shielding of the HI in a cell. The shielding is simply a reduction of the ionization rate by the factor $e^{-N(HI)\sigma_H}$. This factor will be important in dense, collapsed regions.

4.4.2 Models with extra heating

Optically thin photoheating from HI, HeI, and HeII ionizations by the UVB produces heating rates proportional to the density of the species being ionized. Other possibilities exist. We also ran simulations testing other heating sources, including heating from TeV gamma rays from blazars or from an X-ray background from AGN.

We ran 2 simulations with a hard X-ray background model from [24]. This X-ray background heats the IGM through Compton scattering off of free electrons, and so the heating rate is proportional to the density of electrons. Thus with hard X-rays, extra heat is added to the ionized regions of the IGM, rather than to the neutral regions as is the case for photoionizations.

We also ran 3 simulations including heating from TeV gamma rays produced by blazars. We use the model from [8], in which TeV gamma rays pair produce high energy electrons and positrons, which excite plasma instabilities leading to a local dissipation of the pairs' kinetic energy. This effectively means including a heating rate that is constant throughout the volume of the IGM, with no density dependence. This model is based on observations of blazars in the local universe at $z \sim 0.1$, and then extrapolating to high redshift by assuming that the blazar luminosity function evolves in the same way as the quasar luminosity function [6].

4.4.3 Cosmological parameters

We adjust 3 parameters that alter the matter power spectrum used as initial conditions to our simulations: the amplitude of the primoridal power spectrum σ_8, the spectral index n_S, and the presence of a single massive neutrino. For most of our simulations, we use values given in Table 4.3, which are near to those determined by the CMB data [12]. We also use values that are beyond the realistically allowed range so as to be certain that we have explored all of the parameter space. We use σ_8 between 0.5 and 1.1, and n_s between 0.86 and 1.06. As a crude test for the

Table 4.3: Standard cosmological parameters for our simulations.

Parameter	Value	Parameter	Value
Ω_{total}	1	h	0.71
Ω_Λ	0.73	n_s	0.96
Ω_m	0.27	σ_8	0.8
Ω_b	0.044		

effect of a single massive neutrino, we use an initial matter power spectrum from CAMB with $\Omega_\nu = 0.02$. We also ran a single simulation initialized with CAMB's matter power spectrum rather than the standard matter power spectrum from [13] as verification that the 2 methods give similar results. For both simulations initialized with CAMB outputs, we used our standard cosmological parameters specified in Table 4.3, and set all other parameters to their default values.

4.4.4 Simulated spectra

We make flux spectra using code described in [42], and used in [20, 37]. These spectra are created by choosing a random initial position in the simulation box and a random initial direction, and casting a ray that changes to a new random direction upon hitting the edges of the cube. The neutral hydrogen density, temperature, and velocity of each simulation cell is used to integrate a Voigt profile along the line of sight that includes both the thermal doppler broadening of the absorption lines as well as the natural line width and damping wings. Pixels are generated with the same velocity width as HIRES spectra, $2.1 km/s$. The simulated spectra are each 20000 pixels long, similar in length to real HIRES spectra.

We use the same algorithm to calculate the Lyα forest flux power spectrum as was used for actual HIRES spectra in Chapter 3. This algorithm was designed to handle gaps in the spectra caused by metal lines and other imperfections in observational data, as well as short spectrum segments due to S/N and redshift binning. While we don't have these issues in simulated spectra, using the same technique eliminates this as a source of error when making a comparison between

the simulated spectra and observational data.

4.4.5 Box size corrections

To measure the flux power spectrum at large scales, the simulation box size must be large enough to contain the longest modes that are to be compared to the observational data. Due to computational limits, there is a trade off between box size and resolution. We choose to use a box size of dimension 19.2 comoving Mpc per side for the bulk of our simulations, which is about twice as large as necessary to contain power at wavenumber $log(k) = -2s/km$. To account for effects due to finite box size, we run 1 simulation that is twice as large, at 38.4 Mpc per side. Holding all other properties of the simulation constant, we divide the 2 output parameters from the larger box by those obtained from the smaller box. This is the scaling factor that we multiply all outputs from the smaller boxes by to correct for finite box size. In all cases, this is never more than about a 5% change to τ_{eff}, P_{-2}, or $P_{-1.5}$. The correction to $P_{-1.0}$ is larger, at around 12% at all redshifts. This is due to the higher temperatures present in simulations run with larger volumes, as was examined in [37]. Higher temperatures lead to greater doppler broadening, which decreases the power at the smallest scales. Prior papers have shown that this correction is sufficient [37, 30].

4.4.6 Cell size corrections

Having chosen the box size, the resolution is effectively determined by the computational resources available. For the bulk of our analysis, we use boxes with 256 cells on a side, which yields a cell size of 75 kpc. We also run two simulations with box length of 9.6 Mpc, 1 with a cell size of 75 kpc, and the other with 18.75 kpc. The scaling factors to correct for finite resolution are defined as the output parameter at the small cell size divided by the output parameter at the standard cell size. For τ_{eff}, this effect is around 5% at redshift 3.2 and 9% at redshift 2.0. For

P_{-2} it varies from 14% at z=3.2 to 24% at z=2.0. While these effects are larger than ideal, increasing the resolution further would not necessarily give a more realistic model. At smaller scales, dense structures such as galaxies and quasars can form, and our simulations do not currently have all the necessary physics to model these. If the resolution used here is not sufficient, then a significantly more sophisticated model is required than we use here or others have used in the past.

4.4.7 Observational data corrections

Reference [28] showed that several residual systematic uncertainties need to be corrected for when comparing the simulated and observed SDSS data power. These include corrections for SiIII absorption (found in the Lyα forest but not on the red side of the Lyα emission peak), strong absorption systems, noise, and resolution. We make these corrections only in a rough sense. Rather than explicitly attempting to find best fit values for adjustable parameters that account for the uncertain noise and resolution effects, as was done in [30, 38], we simply assign similar values for these effects as did the prior analyses. These effects are small enough that any errors from using our simple approach will not effect our conclusions. Thus we subtract 2% from P_{-2} for noise and 1% for resolution corrections [38, Fig. 1]. For the correlated SiIII feature present in the data, we use [28, Eqn. 15], which results in a $\sim$ 5% increase to the SDSS P_{-2}. Given that strong absorption systems are not accurately reproduced in simulations, we subtract 5% from the data power to account for this, as suggested in [29, Fig. 3].

4.4.8 Simulation set

Our simulation set includes:

1. 4 simulations to correct for box size and resolution effects.

2. 25 simulations run with the UVB from [15], varying only γ_{912} and X_{228}. We

used values of γ_{912} ranging between 0.3 and 1.8, and values of X_{228} ranging between 0.3 and 2. Measurements of the temperature of the IGM [33, 34, 26], as well as comparisons to Lyα line widths [20, 22] place constraints which prevent us from raising X_{228} beyond the range we use here.

3. 4 simulations run with the UVB from [17], varying γ_{912}, X_{228}, and Γ_{228}.

4. 4 simulations run with the UVB from [17], varying the cosmological parameters σ_8 and n_s.

5. 2 simulations run with CAMB initial conditions, 1 of which includes a single massive neutrino.

6. 1 simulation run with the UVB from [7], testing self shielding effects.

7. 1 simulations run with a hard X-ray background emitted by AGN from [24].

8. 2 simulations run with a TeV gamma ray background emitted by blazars from [8].

9. 1 simulation run with both a hard X-ray background from [24] and a TeV gamma ray background from [8].

We give the input parameters to our simulations in Table 4.3 and in Table 4.4. In Table 4.5, Table 4.6, Table 4.7, and Table 4.8 we list the values of τ_{eff}, P_{-2}, $P_{-1.5}$, and P_{-1} that the simulations output at redshifts 2.0, 2.4, 2.8, and 3.2.

4.5 Comparing simulations to observational data

Our main result is that the small scale Lyα forest power spectrum and optical depth obtained from any of our wide range of state of the art ENZO simulations do not match observational data.

The combination of just two numbers, τ_{eff} and P_{-2}, is enough to show that hydrodynamic simulations do not match observational data. Although we

have simulations which match either τ_{eff} or P_{-2} at a particular redshift, there is no simulation which can match both parameters at any redshift. In fact, the compatibility of the two statistics is worse at higher redshift. Furthermore, for a simulation that closely matches the observed P_{-2} value at low redshift, the simulated value is far above data at high redshift. Also, the shape of the power spectrum at scales in the range $-2.0 \leq logk \leq -1.0$ cannot be obtained from our simulations.

4.5.1 Adjusting the amplitude and heating of the uniform ionizing background

For our set of 24 simulations in which we only altered X_{228} and γ_{912}, figure 4.1 shows contour plots for the absolute value of the difference between the simulation outputs and the observational data values in the $X_{228}-\gamma_{912}$ plane. Each contour line is a fixed number of standard deviations away from the data value. There are several things to notice in these plots. First, the 1-sigma levels of the contours for τ_{eff}, P_{-2}, $P_{-1.5}$, and P_{-1} do not overlap at any redshift. This implies that the simulations cannot simultaneously produce values of τ_{eff} and small scale power that match the actual observed values. This is also true of just the three power measurements together. P_{-2} and P_{-1} have quite different contours, indicating that the shape of the power spectrum in the simulations is not consistent with observations.

Even worse, the overlap of τ_{eff} and P_{-2} gets worse with increasing redshift. Given the lack of a match at high redshift, the somewhat better, although still poor match at redshift 2.0 is called into question. If the astrophysical conditions do not produce τ_{eff} and P_{-2} values that match observed data values at high redshift, it is not valid to use these same conditions to produce a better fit at low redshift.

Although the contours for any single statistic follow roughly the same shape for all redshifts, the sigma level of a given band in the $X_{228}-\gamma_{912}$ plane varies with

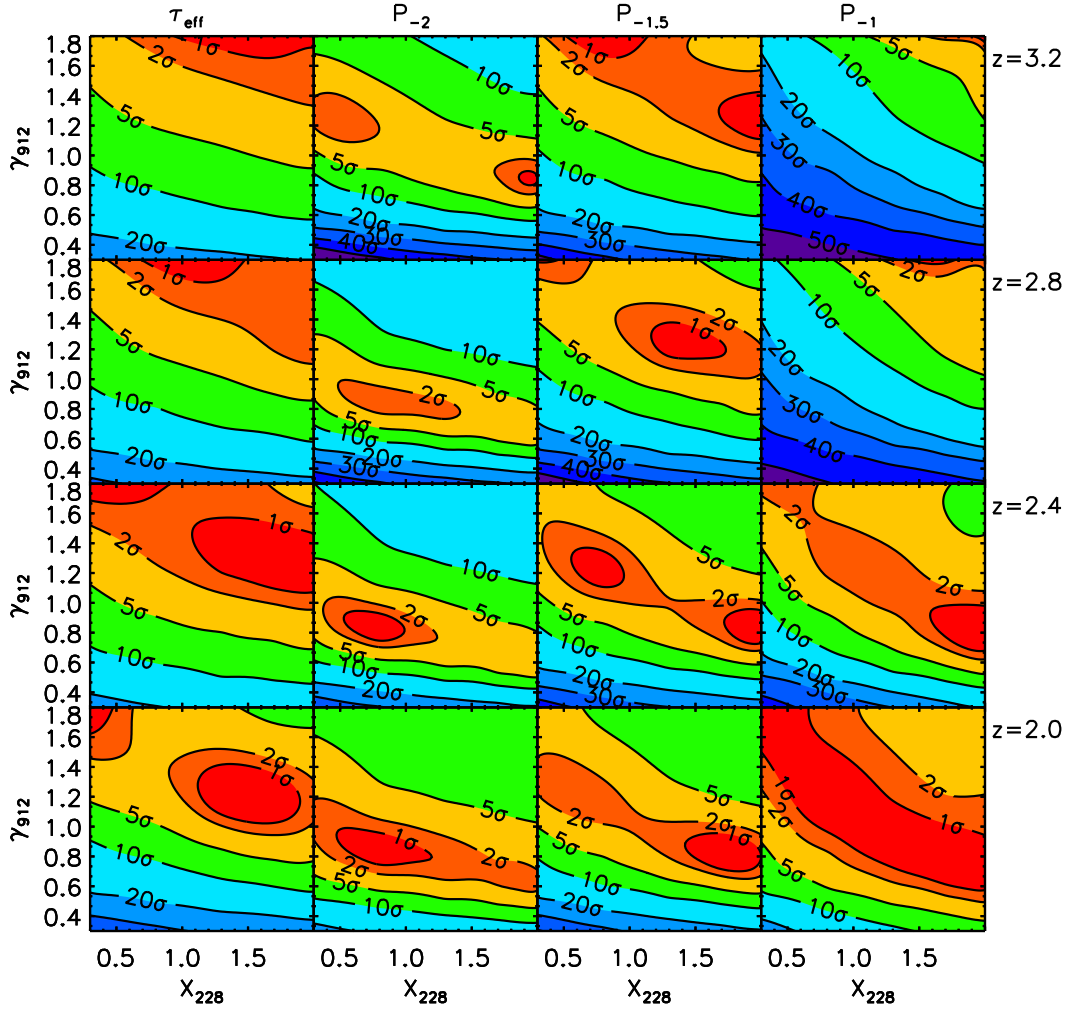

Figure 4.1: Contours showing the number of standard deviations between the simulated and observed Lyα forest statistics. We show the mean absorption τ_{eff} on the left and the intermediate-scale power P_{-2} on the right. We label the contours by the number of σ shown on the plot, where 1σ is the error reported for the data only, with no contribution from the simulation, a fair approximation. Each of the 8 panels show the full range of IGM models as a function of γ_{912} (UVB intensity) on the vertical axis, and X_{228} (HeII photoheating rate) on the horizontal axis. Each row is for the redshift given on the right edge of the plot. The simulation data is listed in Table 4.5, Table 4.6, Table 4.7, and Table 4.8. We made a correction for resolution. The data and simulations agree in the red regions, but those regions correspond to different simulations for the two columns. Hence, there is no simulation that matches both τ_{eff} and P_{-2} simultaneously at any redshift.

redshift. This can be seen especially for the τ_{eff} contours at redshifts 2.8 and 3.2, where a 1-sigma fit is only achieved at the upper right of the plot, compared to at redshifts 2.0 and 2.4 where a 1-sigma fit can be achieved at lower values of γ_{912} . This variation with redshift for a single statistic could be fixed by modifying the redshift evolution of the amplitude of the UVB.

Figure 4.1 can also be used to examine the dependence of the τ_{eff} and power fits on X_{228} and γ_{912}. The density of the contour lines show the slope of the change in the simulation output value. For example, all of the P_{-2} plots have a high density of lines at low γ_{912}, showing that the power varies rapidly with changing γ_{912} for low values of γ_{912}, while the lines are less dense at high γ_{912}, showing that P_{-2} becomes less sensitive to changes in γ_{912} as γ_{912} increases. This also implies that at higher redshift, when the amplitude of the ionizing background is lower because there are less sources, the power will be more sensitive to the precise amplitude of the ionizing background. This higher sensitivity at high redshift is seen as the higher number of sigma levels contained in the contour plots of both τ_{eff} and P_{-2} at higher redshift. It can also be seen that there are bands of space in the $X_{228}-\gamma_{912}$ plane that yield the same quality of fit to the observational data values, for each of the contour plots, separately. The closed bubbles that appear as the 1 and 2 sigma levels are actually artifacts of the limited resolution of the grid. With greater resolution, these bubbles would stretch out and become valleys, as are seen for the contours at higher sigma.

Figure 4.2 shows τ_{eff} and P_{-2} as a function of redshift for observational data compared to two of our simulations. The red triangle symbols (γ_{912}=1.8, X_{228}=0.8) are for the simulation that gives the closest match to the τ_{eff} data values, while the green circle symbols (γ_{912}=0.8, X_{228}=0.8) are closest to the P_{-2} data values. Although we can choose a simulation with τ_{eff} values that are not far from observed values over a wide range of redshift, the same simulation will give P_{-2} values that are far below the observed values. For P_{-2}, we have a simulation that is close to observed data for $z = 2.0, 2.4$, and 2.8, but at $z = 3.2$, the simulated

value is much higher than expected. This alone would indicate that the redshift dependence of the amplitude of the ionizing background needs modification. If we were to raise γ_{912} only at $z = 3.2$, this would lower both P_{-2} and τ_{eff}, pushing the simulated values closer to those from observational data. However, this would still not match P_{-2} and τ_{eff} simultaneously.

4.5.2 Exploring a wide parameter space.

In Figure 4.3, we show that none of our simulations can match observations, particularly at high redshifts. Each row in the plot shows P_{-2} vs DA, $P_{-1.5}$, and $P_{-1.0}$ for our various simulations, as well as the observationally measured values represented by the black error bars. The mismatch is most notable at redshifts 3.2 and 2.8 in the plot of P_{-2} vs $P_{-1.5}$.

Cosmological parameters

In addition to the mismatch between simulations and observational data, Figure 4.3 gives some information as to what is necessary to obtain constraints on cosmological parameters. The amplitude of any of P_{-2}, $P_{-1.5}$, or P_{-1} individually does not provide any information for the sought after cosmological parameters. Essentially any value for any 1 of these can be obtained by adjusting the UVB to alter the ionization state of hydrogen. The shape of the power spectrum over this factor of 10 change in wavenumber is also not very sensitive to cosmological parameters. This can be seen from the P_{-2} vs $P_{-1.5}$ or P_{-2} vs P_{-1} plots. The simulations run with varying values of σ_8, n_s, and neutrino mass do not deviate much from simulations run with various UVB conditions.

Adding the mean level of absorption as an additional statistic greatly increases the sensitivity to cosmological parameters. In the P_{-2} vs DA plot, the blue diamond, red x, and purple asterisk symbols representing changes to cosmological parameters fall off of the strict line that the black plus and green triangle symbols

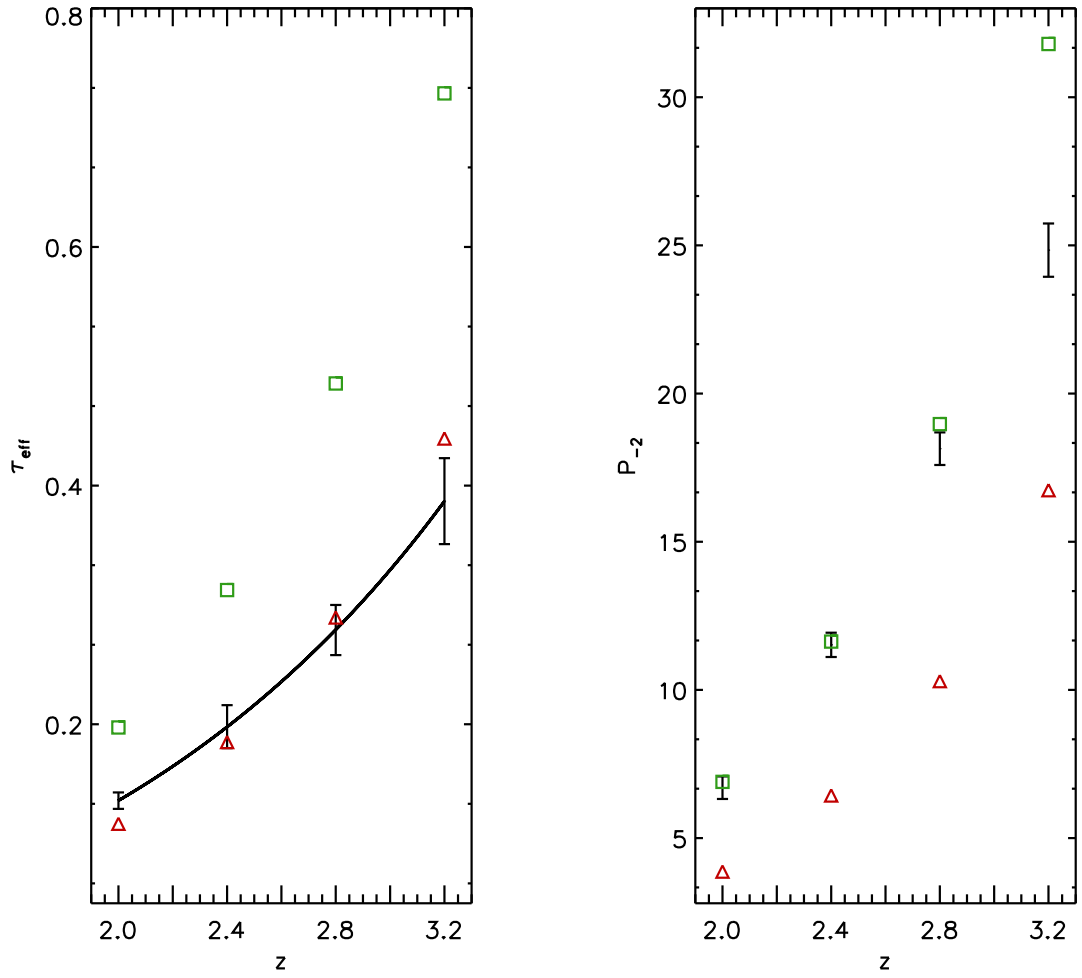

Figure 4.2: The mean amount of Lyα absorption, τ_{eff} on the left, and the power of the flux P_{-2} on the right as a function of redshift horizontally. Black error bars are observational data. The red triangles are from a simulation with γ_{912}=1.8, X_{228}=0.8 that is close to the observed amount of absorption at several redshifts, but with significantly less power than the data. The green circles are from a different simulation with γ_{912}=0.8 and X_{228}=0.8 that is close to the observed power out to z=2.8, but the circles on the left column show far more absorption than the data. The line in the τ_{eff} vs z plot is the function given in [23], which is a fit to τ_{eff} data points between $1.6 < z < 3.2$. The simulation data used is listed in In Table 4.5, Table 4.6, Table 4.7, and Table 4.8. We made corrections for resolution and box size. We can find simulations that match either the amount of absorption or the power over a range of redshifts, but no simulation simultaneously matches both the absorption and the power.

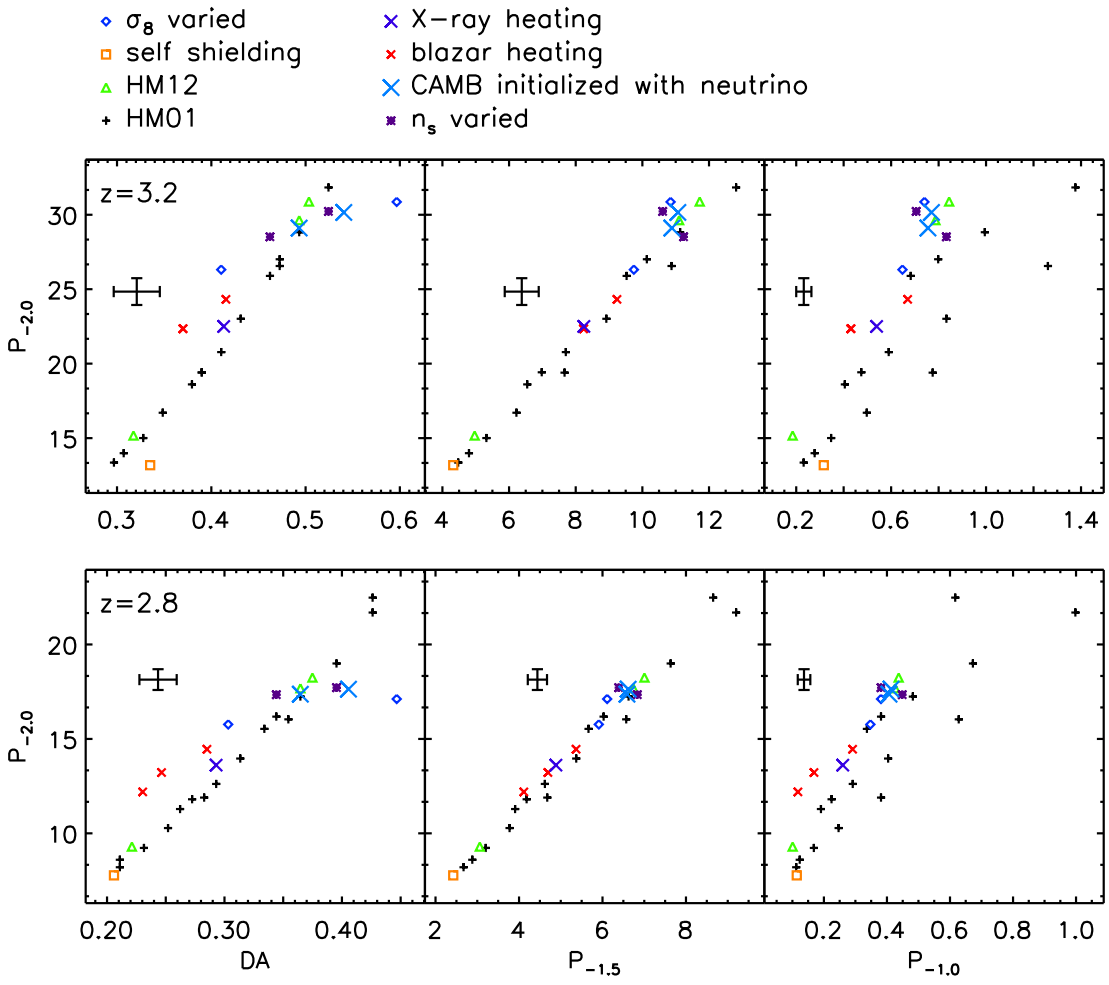

Figure 4.3: P_{-2} vs DA, $P_{-1.5}$, and P_{-1}. The large black crosses represent the actual observed values. Simulation input parameters are listed in 4.4. The unscaled outputs from the simulations are listed in Tables 4.5, 4.6, 4.7, and 4.8. Small black plus symbols represent simulations that use a uniform UVB from [16] (HM01), with γ_{912} and X_{228} varied, and with standard cosmological parameters. Green triangles use a substantially different UVB from [17], once again varying γ_{912} and X_{228}, and with standard cosmological parameters. Large light blue X symbols use initial conditions from CAMB, with the points farther to the right in the P_{-2} vs DA plot including 1 massive neutrino. Purple asterisk symbols use spectral index values of 0.86 and 1.06, with the asterisk farther to the right in the P_{-2} vs DA plot set to 0.86. Blue diamonds represent simulations with σ_8 equal to 0.5 and 1.1, with the diamond farther to the right in the P_{-2} vs DA plot set to 0.5. The orange square represents a simulation which utilizes the ionizing background described in [7], which includes self shielding of the HI to ionizing radiation. Medium dark blue X symbols represent simulations which include X-rays. Small red X symbols are for simulations with TeV gamma rays from blazars.

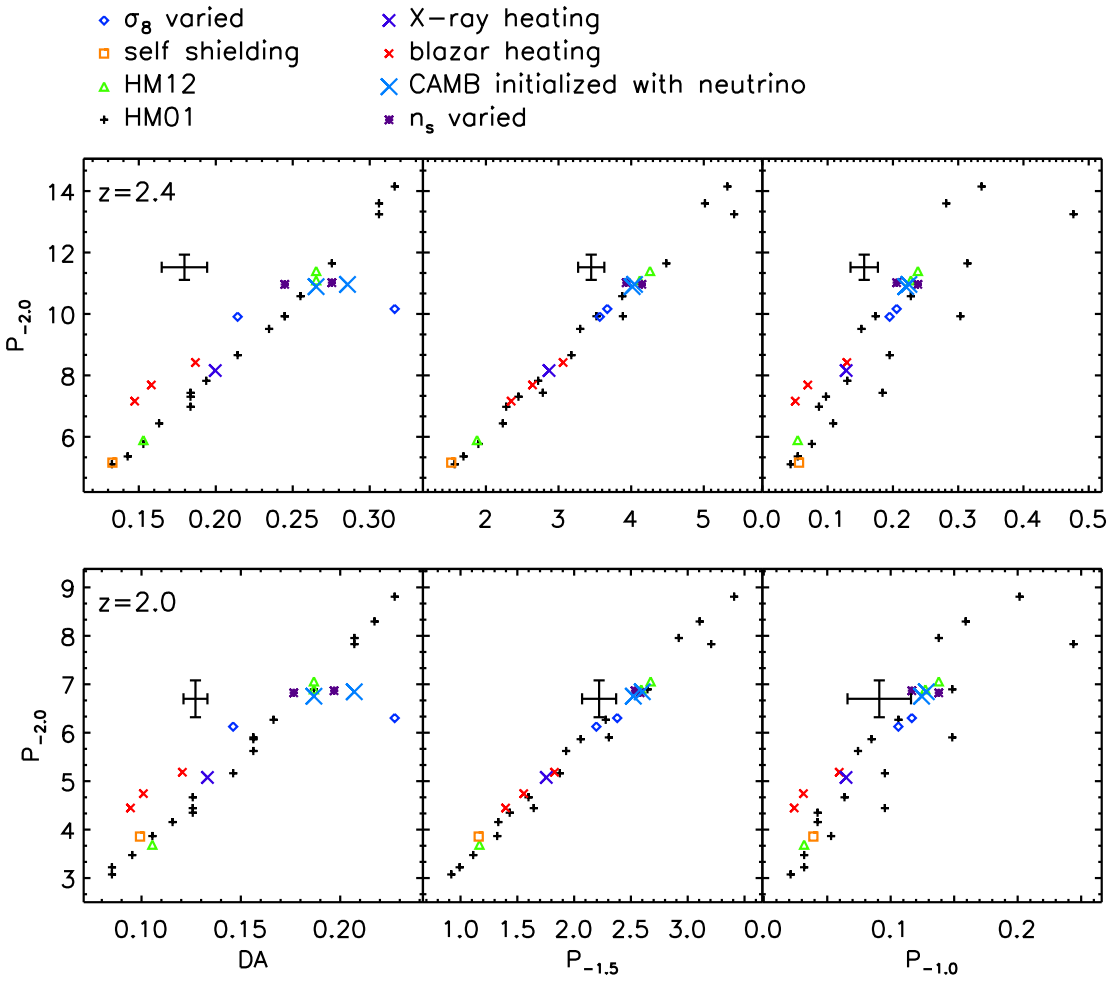

Figure 4.4: As Figure 4.3

that represent changes to the UVB follow.

Unfortunately, all of the simulations, regardless of cosmological or UVB parameters, fall at least a few sigma away from observational data. Even worse, adding a massive neutrino or decreasing σ_8 makes the values more discrepant.

Comparing different UVB models

In Figure 4.3, the green triangle, black plus, and orange square symbols represent simulations that use exactly the same cosmological parameters and initial conditions. They only differ in the UVB model used. The black plus symbols use the UVB model from [16], and are the same simulations as were used in Figure 4.1. These simulations were run with various values of γ_{912} and X_{228}. The green triangle symbols use the more recently published UVB model from [17], which is essentially an update of the model in [16]. The orange square symbol uses the UVB based on the star formation rate, as discussed in §4.4.1. This single simulation has the important addition of self shielding of HI.

It can clearly be seen that the green triangle symbols compared to the black plus symbols offer little freedom in adjusting the relationship between P_{-2} and DA, $P_{-1.5}$, and P_{-1}. The photoionization rates and photoheating rates of HI, HeI, and HeII are quite different between these 2 models, and these rates completely specify a uniform UVB. Since none of these simulations deviate from a linear relationship between P_{-2} and DA or P_{-2} and $P_{-1.5}$, it can be concluded that no value of these rates can produce a simulation that matches observations for this set of statistics. The uniform UVB used as the only source of ionization and heating of the IGM, as implemented in ENZO, is not a valid model for the IGM at the precision offered by current observational data.

At z=3.2, the use of self shielding in the simulation represented by the orange square symbol does fall slightly off of the standard curve on the P_{-2} vs DA plot set by the other 2 UVB models, but it still does not offer the mechanism necessary to agree with observations. The larger difference at z=3.2 than at the

lower redshifts can be understood by the higher overall neutral fraction at higher redshift. With a higher HI density, self shielding is more important. Unfortunately, even this small difference is in the wrong direction, making the mismatch between simulations and observations even more severe.

The shape of the power spectrum is somewhat sensitive to the ionization and heating rates of the IGM, as can be seen from the scatter in the P_{-2} vs P_{-1} plot. This scatter is mostly caused by the sensitivity of P_{-1} to the width of the absorption lines, with higher temperature leading to wider lines. It may be possible to obtain a match for both P_{-2} and P_{-1} simultaneously, but for redshifts 2.8 and 3.2, this would require higher temperatures than provided by any of our simulations. It could be that effects of radiative transfer physics, which are missing from our simulations, account for this temperature increase. Since HeII reionization completes around a redshift of 2.8, this could explain why at the lower redshifts of 2.4 and 2.0 there is better agreement.

TeV gamma rays from blazars and X-rays from AGN

The lack of a solution with any UVB model raises questions about the nature of the ionization and heating of the IGM. The UVB provides photoionization and photoheating rates that are proportional to the density of the neutral fraction of the species being ionized. Other sources of heating are known to exist, and it is possible that these sources have a non-negligible contribution.

In Figure 4.3, the medium sized dark blue X symbol represents a simulation with X-rays produced by AGN [24], and the small red X symbols represent simulations that include TeV gamma rays produced by blazars [8]. These two sources heat the IGM differently than a UVB model, as discussed in 4.4.2. The X-ray background has little effect on our results. It is possible that the intensity could be higher, particularly at high redshifts where the observations have large uncertainties. However, it is difficult to see how X-rays could account for the large mismatch between simulated and observed statistics we find here.

Blazars potentially have a greater influence on the simulation outputs, with the largest effect on the pair of P_{-2} and DA. Simulations with TeV gamma rays included have a larger value of P_{-2} for a fixed value of DA, as is required by ovservational data. Although the discrepancy is reduced at all redshifts, a match is not found at any redshift. Unfortunately, even these heating sources do not provide a mechanism to match the shape of the power spectrum.

The plots of P_{-2} vs $P_{-1.5}$ show that we do not have a way to cause the simulation outputs to deviate from a strictly linear relationship. Any variation of an input parameter which causes P_{-2} to change by some factor, also causes $P_{-1.5}$ to change by the same factor. We do not find a mechanism to alter the shape of the power spectrum on these close scales.

4.6 Discussion

4.6.1 The mismatch between simulations and observational data

We have shown that for $2.0 \leq z \leq 3.2$, current hydrodynamic simulations of the IGM do not produce values of τ_{eff} and the Lyα forest flux power spectrum at small scales ($-2.0 \leq logk \leq -1.0$) that simultaneously match those in observational data. There are three related problems. First, there is no single simulation that matches data values for the flux power and τ_{eff} at any single redshift. Second, the compatibility of τ_{eff}, P_{-2}, $P_{-1.5}$, and P_{-1} become worse at higher redshifts for all simulations. Third, when a single simulation matches a single statistic at low redshift, the match becomes worse at high redshift.

The problem with matching both the flux power and τ_{eff} in simulations to data at any individual redshift is that a simulation with the correct τ_{eff} will have power that is too low. Since flux power is defined to be the power of the overdensity of the mean flux, dividing by the mean flux is in its definition. Thus

any process that only raises the mean flux will decrease P_{-2}. Since τ_{eff} is simply another way of stating the mean flux, we need a physical mechanism that will do more than just change the ionization fraction of the hydrogen that is causing the absorption that determines τ_{eff}. Our results show that the variation of γ_{912} and X_{228} does not offer the necessary physical mechanism. Rather than raising or lowering the ionization rate at the same level for all densities, it may be necessary for the ionization rate or heating rate to be a function of density.

The deterioration with increasing redshift of the compatibility between the optical depth and the flux power is particularly troubling. Physical effects of the ionization and thermal history of the IGM at high redshift will influence structure formation. This may leave an imprint on the flux power spectrum measured at lower redshifts. This implies that if we are not able to match simulations to data at high redshift, a closer match at low redshift is suspect.

We do not yet have the answer as to why the difference between simulations and observational data is greater at higher redshifts. A possible explanation for this may be the lack of radiative transfer in our simulations, which are optically thin with a completely homogenous and isotropic UVB. Although the approximation of a homogeneous, optically thin IGM is valid for HI and HeI ionizing photons for redshifts well above those examined here [18, 19], radiative transfer effects are important for HeII ionization until He has been completely ionized throughout the IGM. A non-uniform HeII ionization background implies that the temperature increase due to HeII photoheating is likely a function of the density. This will effect the HI ionization fraction through the recombination rate, which is sensitive to temperature.

For the purposes of determining cosmological parameters from the Lyα forest flux power spectrum, it should be sufficient to obtain the correct thermal state of the IGM through a means that mimics the heat input due to radiative transfer, without explicitly running a radiation transfer simulation. Radiative transfer processes argue that the heating rate per atom is linked to the density of

the gas. One possible change to the method we use here would be to impose a power law relationship between the HeII density and the heat input per HeII ionization, as was done by [4] when examining the Lyα forest flux PDF. This would correspond well to the physical process of the hardening of the radiation field as lower energy photons are preferentially absorbed in dense regions surrounding the sources [2].

4.6.2 Reasons the mismatch between observational data and simulations has gone unnoticed

Because of the high computational cost of running fully hydrodynamic simulations, many approximations have been made in the past. One approximation often made is the use of hydro-particle-mesh (HPM) simulations. HPM simulations model only the evolution of the IGM under gravity, with a pseudo-pressure term added for the baryons by artificially imposing a power law temperature-density relation. HPM simulations may offer unphysical freedom in setting the thermal state of the IGM. Also, most studies focus on only a single statistic of the Lyα forest, ignoring statistics that could shed light on a physical property of the IGM that may be in error in the simulations. Most notably, when analyzing the flux power spectrum alone, the temperature in simulations is sometimes overlooked. In addition, some past studies may not have analyzed the redshift evolution of outputs of a set of simulations with fixed input parameters.

Another common approximation is rescaling the effective optical depth after a simulation has completed in order to match the flux power. The justification of this is that renormalizing the optical depth is effectively equivalent to modifying the intensity of the ionizing background [27]. However, this ignores physical effects that will alter structure formation, such as changes in temperature due to a different photoheating rate, or changes to the importance of collisional ionization. Our results show that while increasing the intensity of the UVB does have the expected general result of decreasing τ_{eff}, it does not do so in such a way that τ_{eff} and the

flux power can both take on their observed values.

Past analyses of the SDSS flux power spectrum have attempted only to match the power between simulations and data, with the effective optical depth given as an output [30, 38]. Surprisingly, the optical depth values obtained are only about 1 standard deviation away from the values measured in [23]. Given all the approximations made by these analyses, this does not imply that any single modern hydrodynamic simulation could obtain the observed values of both the flux power and optical depth without the use of postprocessing or some other method of modifying the final results of the simulation. In fact, given that we obtain much different values for the optical depth for simulations that match the power spectrum when we use unmodified fully hydrodynamic simulations, it would appear that it may be possible to obtain a wide range of optical depth values using the approximations that were made in the past. Given that there is some degeneracy between the amplitude of the linear matter power spectrum and the optical depth, this calls into question past constraints on the linear matter power spectrum.

In this paper, we use the smallest scales available in the Lyα forest, with the largest wavenumber we use near the smallest wavenumber available in the SDSS power spectrum at $logk = -1.75$. It could be that the mismatch between simulations and observations was not noticed previously because of the different scale that the analyses used. The small scales that we use are much more sensitive to the thermal conditions of the IGM. However, if previous analyses used an overly simplistic model of the UVB, as seems likely given our results presented here, then the recombination rate for HII would be invalid. The recombination rate and thus the neutral hydrogen fraction is dependent on the temperature density relationship. This implies that the HI that makes up the Lyα forest could be associated with different total hydrogen densities than generally found in optically thin simulations.

The exact reason that the extent of this problem has not been realized in the past is not known. Aspects of this problem have been addressed by other groups. Reference [4] found that they get a better match to the Lyα forest flux

PDF when they use a simulation that has a nonstandard inverted temperature density relationship, where lower density regions are hotter. Reference [32] finds that including a uniform volumetric heating term to model the effect of heat input from TeV gamma rays from blazars improves the match to Lyα forest statistics. This produces higher temperatures at lower densities, agreeing with [4]. We find that simulations including the volumetric heating term from blazars in cosmological simulations does indeed improve the match to the observed flux power spectrum, but even this does not go far enough to provide an acceptable match.

4.6.3 Conclusion

Before we can obtain constraints on cosmological parameters from the Lyα forest, we must have numerical simulations which produce accurate spatial distributions, velocities, temperatures, and ionization fractions of hydrogen in the low density IGM. The simulations used here, although at least as accurate as those used in several analyses in the past, do not provide physical conditions in the IGM that lead to an optical depth and flux power spectrum that match those in observational data. The small scale flux power we examine here is more sensitive to astrophysics that determine the temperature and ionization fraction of HI in the IGM than on cosmological parameters. Larger scales are available from the SDSS data set, but to interpret this data, it is necessary to obtain the correct ionization fraction of hydrogen in the IGM. This information is best determined by examining the smallest scales available in the flux power spectrum, as we do here. Only by using these small scales can the thermal state and ionization fraction be determined to sufficient accuracy to allow cosmological parameters to be extracted from the larger scale Lyα forest flux power spectrum.

Acknowledgments

This chapter is currently being prepared for submission for publication of the material. Day, Aaron; Tytler, David; Kirkman, David.

Bibliography

[1] T. Abel, P. Anninos, Y. Zhang, and M. L. Norman. Modeling primordial gas in numerical cosmology. *New Astronomy*, 2:181, Aug. 1997.

[2] T. Abel and M. G. Haehnelt. Radiative Transfer Effects during Photoheating of the Intergalactic Medium. *ApJ*, 520:L13, July 1999.

[3] P. Anninos, Y. Zhang, T. Abel, and M. L. Norman. Cosmological hydrodynamics with multi-species chemistry and nonequilibrium ionization and cooling. *New Astronomy*, 2:209–224, 1997.

[4] J. S. Bolton, M. Viel, T. . Kim, M. G. Haehnelt, and R. F. Carswell. Possible evidence for an inverted temperature-density relation in the intergalactic medium from the flux distribution of the Lyman-alpha forest. *ArXiv e-prints 0711.2064*, 711, Nov. 2007.

[5] A. Boyarsky, J. Lesgourgues, O. Ruchayskiy, and M. Viel. Lyman-α constraints on warm and on warm-plus-cold dark matter models. *Journal of Cosmology and Astro-Particle Physics*, 5:12–+, May 2009.

[6] A. E. Broderick, P. Chang, and C. Pfrommer. The Cosmological Impact of Luminous TeV Blazars. I. Implications of Plasma Instabilit ies for the Intergalactic Magnetic Field and Extragalactic Gamma-Ray Background. *ApJ*, 752:22, June 2012.

[7] R. Cen and J. Ostriker. A hydrodynamic treatment of the cold dark matter cosmological scenario. *ApJ*, 393:22–41, July 1992.

[8] P. Chang, A. E. Broderick, and C. Pfrommer. The Cosmological Impact of Luminous TeV Blazars. II. Rewriting the Thermal History of the Intergalactic Medium. *ApJ*, 752:23, June 2012.

[9] R. A. C. Croft, W. Hu, and R. Davé. Cosmological Limits on the Neutrino Mass from the LyAlpha Forest. *Physical Review Letters*, 83:1092, Aug. 1999.

[10] R. A. C. Croft, D. H. Weinberg, M. Bolte, S. Burles, L. Hernquist, N. Katz, D. Kirkman, and D. Tytler. Toward a Precise Measurement of Matter Clustering: Lyα Forest Data at Redshifts 2-4. *ApJ*, 581:20, Dec. 2002.

[11] R. A. C. Croft, D. H. Weinberg, M. Pettini, L. Hernquist, and N. Katz. The Power Spectrum of Mass Fluctuations Measured from the LYalpha Forest at Redshift Z=2.5. *ApJ*, 520:1–23, July 1999.

[12] J. Dunkley, E. Komatsu, M. R. Nolta, D. N. Spergel, D. Larson, G. Hinshaw, L. Page, C. L. Bennett, B. Gold, N. Jarosik, J. L. Weiland, M. Halpern, R. S. Hill, A. Kogut, M. Limon, S. S. Meyer, G. S. Tucker, E. Wollack, and E. L. Wright. Five-Year Wilkinson Microwave Anisotropy Probe Observations: Likelihoods and Parameters from the WMAP Data. *ApJS*, 180:306–329, Feb. 2009.

[13] D. J. Eisenstein and W. Hu. Power Spectra for Cold Dark Matter and Its Variants. *ApJ*, 511:5–15, Jan. 1999.

[14] C. Faucher-Giguere, J. X. Prochaska, A. Lidz, L. Hernquist, and M. Zaldarriaga. A Direct Precision Measurement of the Intergalactic Lyα Opacity at $2 \leq z \leq 4.2$. *ApJ*, 681:831–855, July 2008.

[15] F. Haardt and P. Madau. Radiative Transfer in a Clumpy Universe. II. The Ultraviolet Extragalactic Background. *ApJ*, 461:20, Apr. 1996.

[16] F. Haardt and P. Madau. Modelling the UV/X-ray cosmic background with CUBA. In *Clusters of galaxies and the high redshift universe observed in X-rays, Recent results of XMM-Newton and Chandra, XXXVIth Rencontres de Moriond, XXIst Moriond Astrophysics Meeting, March 10-17, 2001, Savoie France. Edited by D.M. Neumann & J.T.T. Van*, 2001.

[17] F. Haardt and P. Madau. Radiative Transfer in a Clumpy Universe. IV. New Synthesis Models of the Cosmic UV/X-Ray Background. *ApJ*, 746:125, Feb. 2012.

[18] L. Hui and N. Y. Gnedin. Equation of state of the photoionized intergalactic medium. *MNRAS*, 292:27, Nov. 1997.

[19] L. Hui and Z. Haiman. The Thermal Memory of Reionization History. *ApJ*, 596:9–18, Oct. 2003.

[20] T. Jena, M. L. Norman, D. Tytler, D. Kirkman, N. Suzuki, A. Chapman, C. Melis, P. Paschos, B. O'Shea, G. So, D. Lubin, W. Lin, D. Reimers, E. Janknecht, and C. Fechner. A concordance model of the Lyman α forest at z= 1.95. *MNRAS*, 361:70–96, July 2005.

[21] T.-S. Kim, J. Bolton, M. Viel, M. G. Haehnelt, and R. F. Carswell. An improved measurement of the flux distribution of the Ly-alpha forest in QSO absorption spectra: the effect of continuum fitting, metal contamination and noise properties. *ArXiv e-prints 0711.1862*, 711, Nov. 2007.

[22] T.-S. Kim, S. Cristiani, and S. D'Odorico. The Lyalpha forest at 1.5 < z < 4. *A&A*, 373:757, July 2001.

[23] D. Kirkman, D. Tytler, N. Suzuki, C. Melis, S. Hollywood, K. James, G. So, D. Lubin, T. Jena, M. L. Norman, and P. Paschos. The H I opacity of the intergalactic medium at redshifts $1.6 < z < 3.2$. *MNRAS*, 360:1373–1380, July 2005.

[24] P. Madau and G. Efstathiou. Compton Heating of the Intergalactic Medium by the Hard X-Ray Background. *ApJL*, 517:L9–L12, May 1999.

[25] P. Madau, F. Haardt, and M. J. Rees. Radiative transfer in a clumpy universe. III. the nature of cosmological ionizing sources. *ApJ*, 514:648–659, 1999.

[26] P. McDonald, J. Miralda-Escudé, M. Rauch, W. L. W. Sargent, T. A. Barlow, and R. Cen. A Measurement of the Temperature-Density Relation in the Intergalactic Medium Using a New Lyα Absorption-Line Fitting Method. *ApJ*, 562:52–75, 2001.

[27] P. McDonald, J. Miralda-Escudé, M. Rauch, W. L. W. Sargent, T. A. Barlow, R. Cen, and J. P. Ostriker. The Observed Probability Distribution Function, Power Spectrum, and Correlation Function of the Transmitted Flux in the Lyα Forest. *ApJ*, 543:1–23, Nov. 2000.

[28] P. McDonald, U. Seljak, S. Burles, , et al. The Lyα Forest Power Spectrum from the Sloan Digital Sky Survey. *ApJS*, 163:80–109, Mar. 2006.

[29] P. McDonald, U. Seljak, R. Cen, P. Bode, and J. P. Ostriker. Physical effects on the Lyα forest flux power spectrum: damping wings, ionizing radiation fluctuations and galactic winds. *MNRAS*, 360:1471–1482, July 2005.

[30] P. McDonald, U. Seljak, R. Cen, D. Shih, D. H. Weinberg, S. Burles, D. P. Schneider, D. J. Schlegel, N. A. Bahcall, J. W. Briggs, J. Brinkmann, M. Fukugita, Ž. Ivezić, S. Kent, and D. E. Vanden Berk. The Linear Theory Power Spectrum from the Lyα Forest in the Sloan Digital Sky Survey. *ApJ*, 635:761–783, Dec. 2005.

[31] B. W. O'Shea, G. Bryan, J. Bordner, M. L. Norman, T. Abel, R. Harkness, and A. Kritsuk. Intoducing ENZO, an AMR cosmology application. In *Adaptive Mesh Refinement – Theory and Applications. Eds. T. Plewa, T. Linde & V.G. Weirs, Springer Lecture Notes in Computational Science and Engineering.* , 2004.

[32] E. Puchwein, C. Pfrommer, V. Springel, A. E. Broderick, and P. Chang. The Lyman-α forest in a blazar-heated Universe. *MNRAS*, 423:149–164, June 2012.

[33] M. Ricotti, N. Y. Gnedin, and J. M. Shull. The Evolution of the Effective Equation of State of the Intergalactic Medium. *ApJ*, 534:41, May 2000.

[34] J. Schaye, T. Theuns, M. Rauch, G. Efstathiou, and W. L. W. Sargent. The thermal history of the intergalactic medium*. *MNRAS*, 318:817, Nov. 2000.

[35] U. Seljak, A. Makarov, P. McDonald, and and others. Cosmological parameter analysis including SDSS Lyα forest and galaxy bias: Constraints on the primordial spectrum of fluctuations, neutrino mass, and dark energy. *PhysRevD*, 71(10):3515, May 2005.

[36] A. Songaila. The Evolution of the Intergalactic Medium Transmission to Redshift 6. *AJ*, 127:2598–2603, May 2004.

[37] D. Tytler, M. Gleed, C. Melis, A. Chapman, D. Kirkman, D. Lubin, P. Paschos, T. Jena, and A. P. S. Crotts. Metal absorption systems in spectra of pairs of QSOs: how absorbers cluster around QSOs and other absorbers. *MNRAS*, 392:1539–1572, Feb. 2009.

[38] M. Viel and M. G. Haehnelt. Cosmological and astrophysical parameters from the Sloan Digital Sky Survey flux power spectrum and hydrodynamical simulations of the Lyman α forest. *MNRAS*, 365:231–244, Jan. 2006.

[39] M. Viel, M. G. Haehnelt, and V. Springel. Inferring the dark matter power spectrum from the Lyman α forest in high-resolution QSO absorption spectra. *MNRAS*, 354:684–694, Nov. 2004.

[40] M. Viel, J. Lesgourgues, M. G. Haehnelt, S. Matarrese, and A. Riotto. Constraining warm dark matter candidates including sterile neutrinos and light gravitinos with WMAP and the Lyman-α forest. *Phys. Rev. D*, 71(6):063534–+, Mar. 2005.

[41] G. Worseck, J. X. Prochaska, M. McQuinn, A. Dall'Aglio, C. Fechner, J. F. Hennawi, D. Reimers, P. Richter, and L. Wisotzki. The End of Helium Reionization at z ˜= 2.7 Inferred from Cosmic Variance in HST/COS He II Lyα Absorption Spectra. *ApJ*, 733:L24+, June 2011.

[42] Y. Zhang, P. Anninos, M. L. Norman, and A. Meiksin. Spectral Analysis of the Ly alpha Forest in a Cold Dark Matter Cosmology. *ApJ*, 485:496, Aug. 1997.

Table 4.4: Input parameters for all simulations. For the UVB spectrum type, HM01 indicates the use of the UVB model from [16], HM12 indicates [17], and CO indicates [7]. Unless specified otherwise, simulations are run with the cosmological parameters specified in Table 4.3, and with a box size of 19.2 Mpc comoving and a cell size of 75 kpc comoving.

sim #	γ_{912}	X_{228}	UVB	Note
1	0.3	0.3	HM01	
2	0.3	0.8	HM01	
3	0.3	1.3	HM01	
4	0.3	1.7	HM01	
5	0.3	2.0	HM01	
6	0.5	0.3	HM01	
7	0.5	0.8	HM01	
8	0.5	1.3	HM01	
9	0.5	1.7	HM01	
10	0.5	2.0	HM01	
11	0.8	0.3	HM01	
12	0.8	0.8	HM01	
13	0.8	1.3	HM01	
14	0.8	1.7	HM01	
15	0.8	2.0	HM01	
16	1.2	0.3	HM01	
17	1.2	0.8	HM01	
18	1.2	1.3	HM01	
19	1.2	1.7	HM01	
20	1.2	2.0	HM01	
21	1.8	0.3	HM01	
22	1.8	0.8	HM01	
23	1.8	1.3	HM01	
24	1.8	1.7	HM01	
25	1.8	2.0	HM01	
26	1.0	1.0	HM12	$\sigma_8 = 0.5$
27	1.0	0.25	HM12	$\Gamma_{228} = 0.25$
28	1.0	1.0	HM12	$n_s = 0.86$
29	1.0	1.0	HM12	$\sigma_8 = 1.1$
30	1.0	1.0	HM12	
31	0.3	0.3	HM12	
32	1.0	1.0	HM12	$n_s = 1.06$
33	1.8	2.0	HM12	
34	1.0	1.0	HM01	CAMB inits, $\Omega_\nu = 0.02$, $\sigma_8 = 0.62$
35	1.0	1.0	HM01	CAMB inits
36	-	-	CO	Self shielding

Table 4.4 – continued from previous page

sim #	γ_{912}	X_{228}	UVB	Note
37	1.3	1.1	HM01	Box size = 38.4 Mpc, Cell size = 75 kpc
38	1.3	1.1	HM01	Box size = 9.6 Mpc, Cell size = 18.75 kpc
39	1.3	1.1	HM01	Box size = 9.6 Mpc, Cell size = 75 kpc
40	1.3	1.1	HM01	
41	1.0	1.0	HM01	xrays
42	1.0	1.0	HM01	blazar heating
43	1.0	1.0	HM01	blazar heating, 3 times heat input
44	1.0	1.0	HM01	xrays and blazar heating

Table 4.5: Lyα forest flux power spectrum at scale $log(k)$ ($P_{log(k)}$) and effective optical depth (τ_{eff}) values for each simulation. Units of k are s/km. Units of $P_{log(k)}$ are km/s.

z=2.0				
sim #	τ_{eff}	P_{-2}	$P_{-1.5}$	P_{-1}
1	0.448	20.9	7.55	0.675
2	0.404	18.7	6.43	0.472
3	0.375	17.2	5.68	0.352
4	0.357	16.3	5.22	0.286
5	0.345	15.7	4.93	0.248
6	0.330	14.6	5.07	0.384
7	0.296	13.0	4.25	0.257
8	0.273	11.9	3.71	0.186
9	0.259	11.2	3.38	0.147
10	0.250	10.7	3.18	0.126
11	0.247	10.6	3.49	0.226
12	0.220	9.31	2.88	0.145
13	0.202	8.46	2.48	0.101
14	0.191	7.92	2.24	0.078
15	0.184	7.59	2.10	0.066
16	0.191	7.97	2.51	0.141
17	0.169	6.97	2.04	0.0869
18	0.155	6.30	1.74	0.0586
19	0.146	5.87	1.56	0.0446
20	0.140	5.61	1.45	0.0370
21	0.147	6.00	1.79	0.0867
22	0.130	5.22	1.44	0.0514
23	0.118	4.69	1.21	0.0336
24	0.111	4.35	1.08	0.0251
25	0.106	4.15	1.00	0.0205

Table 4.5 – continued from previous page

z=2.0				
sim #	τ_{eff}	P_{-2}	$P_{-1.5}$	P_{-1}
26	0.270	8.51	2.59	0.111
27	0.223	9.53	2.91	0.129
28	0.236	9.27	2.76	0.112
29	0.176	8.27	2.39	0.101
30	0.221	9.31	2.82	0.122
31	0.552	26.5	9.61	0.841
32	0.206	9.21	2.81	0.129
33	0.127	4.98	1.27	0.0288
34	0.248	9.24	2.83	0.121
35	0.223	9.12	2.75	0.117
36	0.121	5.21	1.26	0.0369
37	0.149	6.03	1.68	0.0538
38	0.144	4.82	1.85	0.0894
39	0.158	6.36	1.96	0.0740
40	0.152	6.18	1.72	0.0613
41	0.159	6.85	1.91	0.0612
42	0.145	7.00	1.99	0.0561
43	0.123	6.40	1.70	0.0295
44	0.116	6.00	1.52	0.0227

Table 4.6: Lyα forest flux power spectrum at scale $log(k)$ ($P_{log(k)}$) and effective optical depth (τ_{eff}) values for each simulation. Units of k are s/km. Units of $P_{log(k)}$ are km/s.

z=2.4				
sim #	τ_{eff}	P_{-2}	$P_{-1.5}$	P_{-1}
1	0.687	33.9	12.8	1.35
2	0.620	30.1	10.9	0.955
3	0.575	27.6	9.62	0.720
4	0.547	26.1	8.85	0.591
5	0.529	25.2	8.38	0.516
6	0.509	23.3	8.49	0.760
7	0.457	20.6	7.12	0.520
8	0.421	18.9	6.23	0.381
9	0.400	17.8	5.70	0.307
10	0.386	17.1	5.37	0.265
11	0.383	16.6	5.80	0.444
12	0.341	14.6	4.80	0.293
13	0.313	13.3	4.15	0.208

Table 4.6 – continued from previous page

z=2.4				
sim #	τ_{eff}	P_{-2}	$P_{-1.5}$	P_{-1}
14	0.296	12.5	3.77	0.165
15	0.286	11.9	3.53	0.140
16	0.297	12.5	4.16	0.277
17	0.263	10.9	3.40	0.177
18	0.240	9.82	2.91	0.122
19	0.227	9.17	2.62	0.0945
20	0.218	8.76	2.44	0.0793
21	0.229	9.33	2.98	0.172
22	0.202	8.08	2.39	0.105
23	0.183	7.24	2.03	0.0703
24	0.172	6.73	1.81	0.0533
25	0.166	6.41	1.68	0.0441
26	0.403	12.8	3.93	0.189
27	0.329	14.3	4.56	0.221
28	0.349	13.8	4.21	0.191
29	0.260	12.4	3.82	0.177
30	0.326	13.9	4.41	0.212
31	0.816	42.0	15.6	1.52
32	0.303	13.8	4.44	0.224
33	0.186	7.40	2.01	0.0515
34	0.357	13.8	4.33	0.207
35	0.329	13.7	4.30	0.203
36	0.163	6.48	1.63	0.0518
37	0.233	9.60	2.82	0.111
38	0.224	7.65	3.09	0.181
39	0.241	9.59	3.24	0.147
40	0.236	9.61	2.88	0.126
41	0.243	10.2	3.07	0.119
42	0.227	10.6	3.28	0.120
43	0.192	9.65	2.83	0.0643
44	0.180	8.99	2.51	0.0466

Table 4.7: Lyα forest flux power spectrum at scale $log(k)$ ($P_{log(k)}$) and effective optical depth (τ_{eff}) values for each simulation. Units of k are s/km. Units of $P_{log(k)}$ are km/s.

z=2.8				
sim #	τ_{eff}	P_{-2}	$P_{-1.5}$	P_{-1}
1	1.03	57.3	22.3	2.77

Table 4.7 – continued from previous page

z=2.8				
sim #	τ_{eff}	P_{-2}	$P_{-1.5}$	P_{-1}
2	0.933	50.4	18.8	1.96
3	0.865	45.9	16.6	1.48
4	0.823	43.3	15.2	1.21
5	0.796	41.7	14.4	1.06
6	0.772	38.3	14.4	1.53
7	0.693	33.7	12.0	1.06
8	0.639	30.7	10.5	0.784
9	0.607	28.9	9.65	0.636
10	0.587	27.7	9.10	0.551
11	0.583	26.8	9.68	0.890
12	0.520	23.4	8.03	0.596
13	0.478	21.3	6.97	0.432
14	0.453	20.0	6.34	0.345
15	0.437	19.2	5.96	0.296
16	0.455	19.8	6.91	0.556
17	0.403	17.2	5.65	0.361
18	0.369	15.6	4.86	0.255
19	0.348	14.6	4.40	0.201
20	0.335	13.9	4.11	0.170
21	0.353	14.7	4.92	0.344
22	0.310	12.7	3.97	0.216
23	0.282	11.4	3.37	0.149
24	0.266	10.6	3.03	0.115
25	0.255	10.1	2.81	0.0960
26	0.616	21.1	6.43	0.338
27	0.491	22.5	7.37	0.393
28	0.524	21.9	6.72	0.340
29	0.387	19.5	6.22	0.315
30	0.486	21.8	7.09	0.378
31	1.21	71.9	27.3	3.00
32	0.448	21.4	7.19	0.400
33	0.278	11.5	3.22	0.091
34	0.544	21.8	6.96	0.369
35	0.478	21.4	6.93	0.363
36	0.255	9.59	2.55	0.102
37	0.358	15.0	4.67	0.230
38	0.346	12.2	5.20	0.380
39	0.367	14.8	5.33	0.297
40	0.362	15.2	4.79	0.262
41	0.371	16.8	5.14	0.232

Table 4.7 – continued from previous page

z=2.8				
sim #	τ_{eff}	P_{-2}	$P_{-1.5}$	P_{-1}
42	0.360	17.8	5.65	0.260
43	0.307	16.3	4.94	0.150
44	0.286	15.0	4.33	0.105

Table 4.8: Lyα forest flux power spectrum at scale $log(k)$ ($P_{log(k)}$) and effective optical depth (τ_{eff}) values for each simulation. Units of k are s/km. Units of $P_{log(k)}$ are km/s.

z=3.2				
sim #	τ_{eff}	P_{-2}	$P_{-1.5}$	P_{-1}
1	1.51	98.6	40.7	5.87
2	1.36	85.6	33.7	4.07
3	1.26	77.5	29.3	3.03
4	1.20	72.8	26.8	2.46
5	1.17	69.9	25.3	2.14
6	1.14	63.8	25.0	3.11
7	1.02	55.5	20.7	2.13
8	0.945	50.3	18.0	1.57
9	0.898	47.3	16.5	1.28
10	0.868	45.4	15.6	1.10
11	0.868	43.5	16.3	1.76
12	0.776	37.8	13.5	1.19
13	0.714	34.3	11.7	0.864
14	0.676	32.1	10.7	0.692
15	0.652	30.8	10.0	0.594
16	0.682	31.6	11.5	1.09
17	0.605	27.4	9.39	0.717
18	0.555	24.7	8.11	0.513
19	0.524	23.1	7.35	0.406
20	0.505	22.1	6.89	0.346
21	0.531	23.1	8.07	0.672
22	0.468	19.9	6.55	0.430
23	0.427	17.8	5.60	0.301
24	0.402	16.6	5.05	0.235
25	0.387	15.9	4.71	0.199
26	0.943	36.7	11.4	0.640
27	0.734	36.7	12.3	0.734
28	0.786	35.9	11.2	0.613
29	0.571	31.3	10.3	0.564

Table 4.8 – continued from previous page

z=3.2				
sim #	τ_{eff}	P_{-2}	$P_{-1.5}$	P_{-1}
30	0.722	35.2	11.7	0.682
31	1.78	130	52.8	6.71
32	0.658	33.9	11.8	0.717
33	0.414	18.0	5.23	0.156
34	0.811	35.9	11.7	0.666
35	0.713	34.6	11.5	0.653
36	0.442	15.7	4.55	0.273
37	0.537	23.5	7.76	0.458
38	0.521	19.6	8.46	0.770
39	0.547	22.8	8.68	0.581
40	0.544	24.1	7.97	0.525
41	0.567	26.8	8.68	0.466
42	0.571	28.9	9.73	0.579
43	0.496	26.6	8.68	0.373
44	0.495	26.6	8.67	0.372